Document Title: Effects of Crimp and Slip on Laminar and Woven Fabrics Subjected To Ballistic Impact

Author(s): Rachel Zhou, Stuart Leigh Phoenix

Document No.: 248133

Date Received: September 2014

Award Number: 2007-DE-BX-K003

November 15, 2013

EFFECTS OF CRIMP AND SLIP ON LAMINAR AND WOVEN FABRICS SUBJECTED TO BALLISTIC IMPACT

Final Report Document submitted to

U.S. Department of Justice
National Institute of Justice
Grant: 2007-DE-BX-K003
Grant Monitor: Debra Stoe

November 15, 2013

By

Rachel Zhou (GRA) and Stuart Leigh Phoenix (PI)
(slp6@cornell.edu)

Sibley School of Mechanical and Aerospace Engineering
Cornell University
Ithaca, NY 14853

Note: This report is based on the PhD Thesis of Rachel Zhou, Cornell University, approved on November 15, 2013.

EFFECTS OF CRIMP AND SLIP ON LAMINAR AND WOVEN FABRICS SUBJECTED TO BALLISTIC IMPACT

Rachel Zhou and S. Leigh Phoenix
Cornell University 2013

In the past decade, there has been growing interest and research on improving the performance of soft body armor materials subjected to high-speed ballistic impact. One "by-product" of the production process for these high strength polymer fibers, which are bundled into yarns, is the existence of undulation or waviness in the yarns, known as crimp. While this has always been treated as undesirable, few comprehensive studies have been done on the true effects of crimp in conjunction with yarn slip in ballistic fabrics.

We first develop an in-house Finite-Difference (FD) numerical model to study the post-impact but pre-failure behavior of crimped fabrics made with Dyneema® yarns. While there has been past literature that attempted to numerically model crimp in ballistic fabrics, we note that the results provided little insight regarding the strain profile of individual yarns, the growth and evolution of tension and cone waves, and the yarn de-crimping process. Our first fabric model has laminar geometry with out-of-plane zigzag crimp, and we validate our results through comparison with previous analytical models developed by the Cornell Phoenix Group. We present the following findings: (i) the peak strain attained by yarns in the fabric is lowered with increase in crimp, but with small sacrifices in terms of velocity deceleration and out-of-plane projectile displacement, (ii) yarn strain build-up towards its maximum value can vary

significantly depending on projectile mass and size dimensions, (iii) tension and cone waves' velocities and shapes are influenced by various parameters including η, the rocking viscosity coefficient, and (iv) allowing for frictional slip between the projectile and the yarns beneath it causes a shock wave effect, which changes the very early response behavior of the fabric post-impact. With our first fabric model, we also ensure that local strain concentrations and other dynamic artifacts resulting from the discretization of the structure are suppressed or smoothed.

Since most fabrics in reality are woven with interlaced, over-under yarn structure, we develop a second crimp model with woven geometry. In addition to the forces from our first model, we introduce six new forces to describe the contact motion between weft and warp yarns in-plane (viscoelastic), and out-of-plane (allowing for compression but imposing a "Hertzian" condition). Correspondingly, we introduce six new parameters to control for yarn slip, crossover forces, and restoring forces. Comparing our two models, we observe that the second model provides greater flexibility and is more realistic in its ability to accurately portray the phenomenon of crimp interchange. Within the woven crimp model, we find many of the same trends in results provided in (i)-(iv) from the laminar model. We also discover that most of these parametric effects are not independent of each other, and provide case studies to show that varying combinations of multiple parameter values can in some cases produce nearly identical simulation behavior, but in other cases significantly different simulation behavior from one another.

BIOGRAPHICAL SKETCH

Rachel Zhou was born in August 1986, in Xuzhou, China. She came to United States with her family when she was six and has lived in 5 different states. Rachel received her Bachelor degree from University of California at Berkeley in December 2007, with a major in Mechanical Engineering. She then joined the Sibley School of Mechanical and Aerospace Engineering of Cornell University in January 2008. Rachel married Jason Yan Wang in January 2010, who earned his Ph.D. degree in Mechanical Engineering at Cornell University in 2012.

To my husband, Jason

ACKNOWLEDGMENTS

I would like to sincerely thank my Ph.D. advisor, Professor Stuart Leigh Phoenix, for his patience, outstanding guidance and constant support during the last 5 years. I am also grateful to Professor Chung-Yuen Hui and Professor Wolfgang Sachse for serving on my special committee and for emphasizing the importance of fundamental solid and wave mechanics theory as part of obtaining a Ph.D. in Mechanical Engineering. In addition to serving on my special committee, I would like to thank Prof. Sachse for his dedicated mentoring during the many semesters I served as a TA for one of his undergraduate mechanics courses.

Much appreciation goes to Dr. Abdulkadir Yavuz, a member of Prof. Phoenix's research group, for his help in developing the numerical model that eventually became the heart of my thesis. This appreciation also extends to Dr. Wei Li, for his analytical and numerical contributions to many aspects of the model. Our research group's ongoing collaboration with DSM Dyneema®, represented by Dr. Harm van der Werff and Dr. Ulrich Heisserer, has been an enlightening experience into the world of fiber development and testing, and I am thankful to them for giving us this opportunity.

I would like to express my gratitude for the financial sponsorship from the U.S. Department of Justice through the National Institute of Justice under Grant 2007-DE-BX-K003, monitored by Debra Stoe. I thank Debra for showing enormous patience regarding our struggle with the code and our effort to eliminate numerical instabilities and artifacts. In retrospect, it is probably no accident that the subjects of crimp and slip, especially when treated together, have not been studied methodically in the literature. I am very happy to have been given the chance to keep working away until ultimately achieving success.

Finally, I thank my husband, Jason Yan Wang, for his love, encouragement and un-wavering support, and also my parents, for their continued belief that with hard work, nothing is impossible.

TABLE OF CONTENTS

LIST OF FIGURES

LIST OF TABLES

CHAPTER 1

INTRODUCTION

Since the beginning of recorded human history, mankind has sought protection from sharp objects and projectiles of combat by wearing protective clothing in the form of body armor, made of materials ranging from animal skins to silk to copper and steel. With the development of more technologically advanced weaponry, the research and quest for more effective forms of personal protection continues to be important today, especially against high-velocity bullets, which are available to not only military but also to civilian populations around the world, including in the United States. By the 1970s, new polymeric lightweight fibrous materials were invented in industrial laboratories and exhibited improved ballistic performance over their nylon predecessors. Since then, Aramids (e.g., Kevlar®, Twaron®, Technora®) and UHMWPE (ultra-high-weight-molecular-polyethylene) (e.g., Dyneema®, Spectra®), along with their various successors from the same composition families, have been widely used in the body armor worn by law enforcement and military personnel across the globe. In tension they differ greatly from nylon, having very high stiffness, extremely high strength to weight ratios, and very low strains to failure (<4%). They are essentially elastic in tension, both at low and high rates of tensile loading, where stiffness differences are relatively minor. Meanwhile, they retain the advantages of nylon in transverse compression, undergoing large plastic deformation without a significant reduction in tensile load-carrying ability (unlike carbon or glass fibers, which shatter). Figure 1.1 illustrates a sequence of possible events that a hypothetical lightweight material system might undergo to halt an armor-piercing bullet (e.g., APM2).

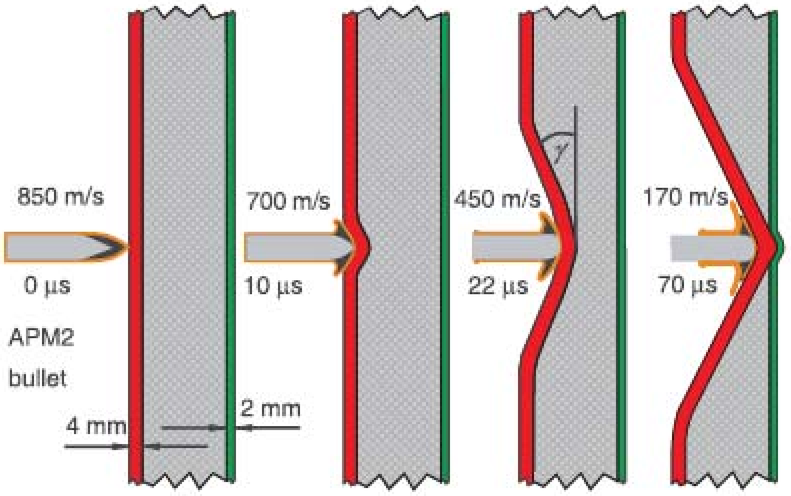

Figure 1.1. Schematic of a hypothetical layered fibrous structure envisioned to stop armor piercing APM2 bullets.

The last decade has seen significant increase in research interest associated with understanding the impact response mechanisms of existing fibrous systems, and not just to develop better materials through trial-and-error methods. Analytically, the fundamental problem of an un-tensioned 2-D membrane impacted transversely by a blunt-nosed projectile was not adequately solved until 2003 by Phoenix and Porwal (2003). Since then, this analytical model has been updated and revised to include multiple bi-axial layers (Phoenix and Porwal, 2003; Phoenix et al., 2010; Phoenix et al., 2010; Li, 2011). The insights provided by these models are presented in Chapter 2. Previously, the earliest work on transverse impact of a projectile into an elastic membrane was done by Grigoryan (1949) for point impact, which neglected circumferential stresses. Galin (1949) and Rakhmatulin and Dem'vanov (1961) believed that neglecting circumferential stresses would lead to unreasonable results. Rakhmatulin and Dem'yanov (1961) reformulated the governing partial differential equation include circumferential stresses and Poisson's ratio effects. The work of Phoenix and Porwal (2003) used Rakhmatulin's and dem'yanov's mathematical formulation, but because of the low strain-to-failure property of the most recent fibers, was able to introduce rescalings and certain approximations that allowed not only partitioning but also particle velocity and strain matching at the edge of the transverse (cone) wave. This resulted in new insights into the problem as well as interpretation of experiments by Cunniff (1999). Vinson and Zukas (1975) adopted a static conical shell theory to fabric impact by a blunt cylindrical projectile and compared results to Roylance et al. (1973, 1980). Chocron-Benluluo et al. (1997) extended the 1-D yarn impact model by including a strain energy based damage variable. Scott (1999) used plate analysis to model the penetration of compliant composites. Walker (1999, 2001) developed an impact model for fabrics and flexible composites using a static deflection analysis for bi-axial membranes under point loading and restrained edges. Cheeseman and Bogetti (2003) presented a summary of relatively recent developments in fabric system impact up to 2003. Tabiei and Nilakantan (2008) continued with a summarization of key concepts relevant to the field up to 2008.

While analytical results can potentially provide a fast and computationally efficient way to solve problems, the assumptions made in their derivation often require the exclusion of details such as yarn slip and fiber waviness, also known as crimp. To track the behavior of single fibers in order to comprehend how they work together to provide ballistic resistance to their fabrics, various numerical models were developed, especially in the last decade, where monumental increases in easily available computing power could be taken advantage of. With this capability, commercial software using the finite-element method (FEM), including but not limited to ABAQUS explicit, LS-DYNA, and AUTODYN, has become the most popular choice for numerically solving a wide variety of ballistic impact problems (Ivanov and Tabiei, 2004; Duan, et al., 2005; King, et al., 2005; Rao, et al., 2009; Cavallaro, 2011; Nilakantan et al., 2013). Gruijic et al. (2008) developed a meso-scale unit-cell based continuum material model for plain-woven single-ply ballistic fabric materials, which could predict fabric deformation and fracture behavior for various fabric edge boundary conditions. Shahkarami and Vaziri (2007) used FEM to simulate projectile impact on woven fabrics and developed a preprocessor to create a 3-D mesh of the unit cell using the measured fabric cross-sectional micro-images. Parsons et al. (2010) utilized a continuum-level modeling technique to describe fabric meso-structure evolution without explicitly modeling every yarn. Barauskas and Abraitiene (2007) modeled the central patch in the impacted fabric with yarn-level detail while the rest of the fabric consisted of orthotropic shell elements. Jin et al. (2010) modeled a bi-axial warp-knitted composite and assumed perfect bonding between yarn and matrix where the elements of each shared the same nodes and surface in meshing. Luan et al. (2013) developed both a continuum model (meshed with hexahedron elements) and a micro-structure model (meshed with 4-node tetrahedron elements) in LS-DYNA for 3-D angle-interlock woven composites. Gopinath et al. (2012) studied the effect of matrix on the performance of woven fabric composites using several commercial packages and treated the Kevlar yarn bundle as a 3-D continuum, meshed with 8-node brick elements.

In addition to FEM modeling, the finite-difference method (FDM) has been another often-used approach to solving the ballistic impact problem (Roylance, 1980; Shim, et al., 1995; Cunniff, et al., 1998; Tan, et al., 2005; Zeng, et al., 2006). Compared to commercial software packages, most FDM codes were written separately by the researcher, and modeled fabrics as a nodal network of pin-jointed mass-spring-damper systems. These simulations usually required much less computational space and time than software packages such as LS-DYNA. We adopt this method for this thesis, and present our detailed algorithm in Chapters 3 and 4.

Beyond the single ply or membrane problem, a more complex geometrical problem is that of modeling crimp in a fabric system. Crimp is defined as the undulation or waviness in yarns, as shown in Fig. 1.2, and is a product of the fiber-yarn-fabric manufacturing process.

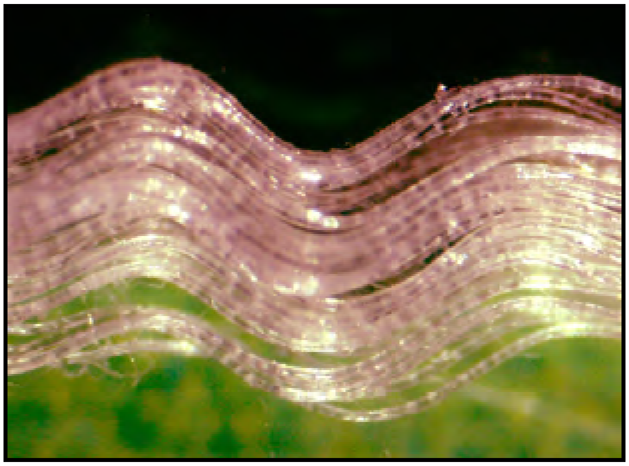

Figure 1.2. Enlarged view of crimped yarn extracted from plain-woven fabric (10^{-3}m) (Cavallaro, 2011).

Current ballistic fabric manufacturing trends view crimp as undesirable (Van et al., 2008; Chou et al., 2011) and seek to keep the amount to a minimum. However, the role crimp plays in the fabric penetration process, post- impact, has only begun to be appreciated and studied in recent years (Shim et al., 1995; Billon, 1998; Cunniff et al., 1998; Kirkwood et al., 2004; Ching and Tan, 2006; Tan and Ching, 2006; Barauskas and Abraitiene, 2007; Atas and Liu, 2008; Hur et al., 2008; Dong and Sun, 2009; Bilisik and Korkmaz, 2010), including with analytical methods (Hur et al., 2008; Ha-Minh et al., 2011; Stig and Hallstrom, 2013). In terms of direction, for the most commonly adopted woven architecture, the plain-weave, yarns from two principal families ("warp" and "weft") are interlaced at right angles to each other, as shown in Fig. 1.3. Since the yarns from each family pass periodically over and under the crossing family, and are bent in the process, woven fabrics are also called "crimped fabrics." In standard textile terminology, warp yarns run lengthwise and parallel to the selvage (fabric edges) while weft (or fill) yarns run widthwise across the fabric width, from selvage to selvage. The points where the weft and warp yarns are in contact with each other are called "crossovers." Lastly, the process with which crimp is pulled out, or the yarn is flattened, is known as "de-crimping."

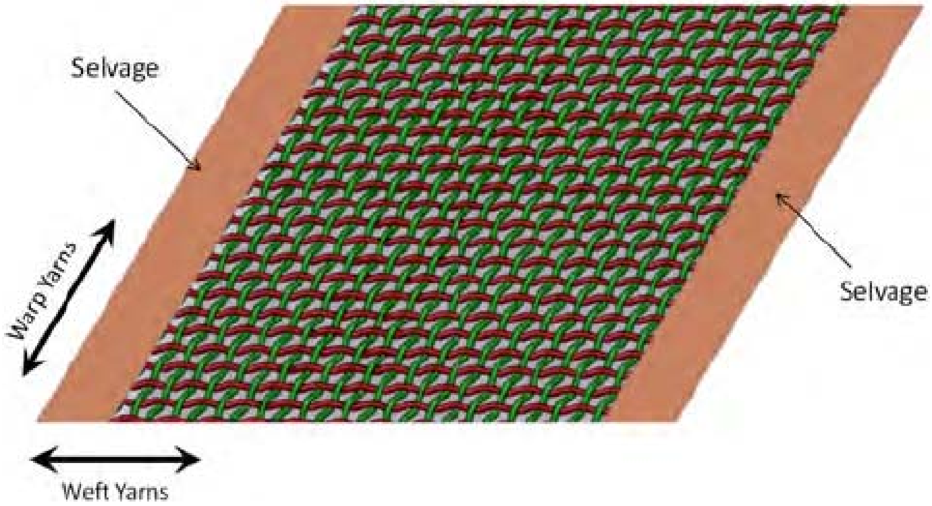

Figure 1.3. Warp and weft yarn directions for plain-woven fabric (Cavallaro, 2011).

Because warp and weft yarns are manufactured independently and then woven together, they often exhibit different degrees of crimp, referred to as crimp imbalance. Cavallaro et al. (2011) conducted extensive studies into crimp imbalance, varying the crimp ratio between the warp and weft yarns, and letting the projectile impact the fabric at oblique as well as normal angles (Cavallaro and Sadegh, 2010; Cavallaro, 2011). Zeng et. al (2006) conducted experiments with various combinations of boundary conditions and used crimp imbalance to explain the different shapes of the pyramidal cone that appeared in the fabric post impact. Tan et al. (2005) introduced crimp into their fabric models via two different ways: first by including the toe region of the load-deflection curve in the constitutive equation describing the viscoelastic elements, and second by arranging the chain of linear elements that define each yarn in a zigzag manner. Duan et al. (2006) used LS-DYNA to show that friction at yarn crossovers slowed the de-crimping process, causing earlier fabric failure. More recently, most numerical crimp models have realized the importance of accurately modeling the motion at yarn crossovers. Numerous studies have included parameters such as rotational spring stiffness, in-plane bending stiffness, viscous-shear stiffness, twist stiffness, and out-of-plane bending stiffness to describe this motion (Ivanov and Tabiei, 2004; King, et al., 2005; Grujicic et al., 2008; Parsons et al., 2013). Even within woven fabrics, experimental studies have been done on different styles of plain-weave (Dong and Sun, 2009) and different weaves such as twill, basket, and satin (Cheng and Chen, 2010; Shimek and Fahrenthold, 2012).

For motion of yarns in woven fabrics subjected to ballistic impact, another key factor to consider is the presence of yarn slip, as shown in Fig. 1.4.

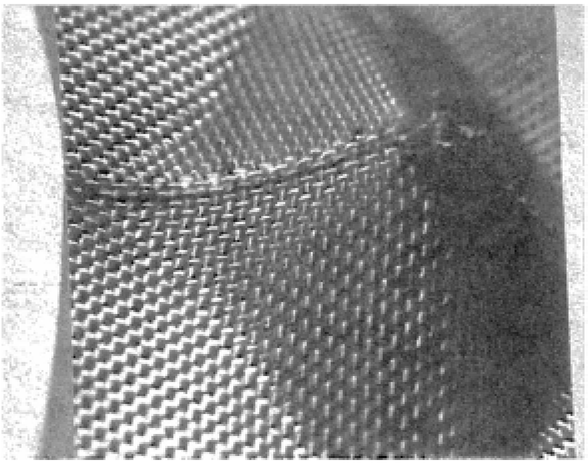

Figure 1.4. Yarn slip seen in a deformed single layer Kevlar29 fabric that had successfully stopped an incoming projectile traveling at 254 m/s (Cunniff, 1992).

This can be of the yarn-yarn form, where warp and weft yarns slide against each other, or it can be of the yarn-projectile form, where yarns in contact with the projectile slide against it. Many experimental and numerical studies have been done to understand the role of slip and/or friction in woven fabrics, some independent of crimp and ballistic impact (Roylance, 1980; Briscoe and Motamedi, 1992; Cunniff, 1992; Bazhenov, 1997; Roylance et al., 1995; Duan et al., 2005; Boubaker et al., 2007; Dong and Sun, 2009; Barauskas and Abraitiene, 2007; Wang et al., 2010). Lim et al. (2002) and Shim et al. (1995) observed a third type of slip where the projectile pushed aside the yarns rather than breaking them, and slipped through to cause fabric failure (Fig. 1.5). This phenomenon can be attributed to a combination of too few crossover points, a very sharp and pointed impacting projectile nose, and low friction between the yarns.

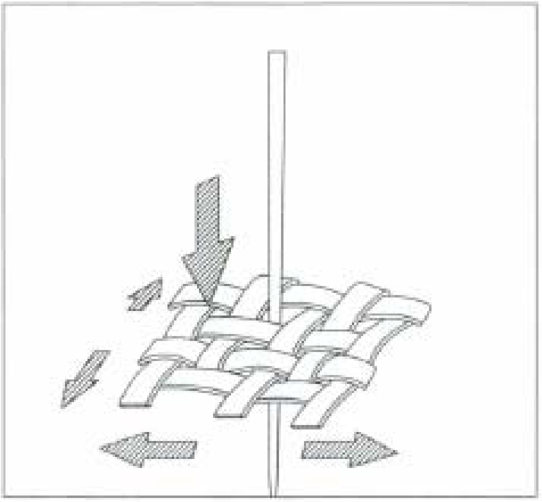

Figure 1.5. A schematic showing the process of a projectile slipping through a piece of not-so-densely woven fabric without failing/breaking the yarns.

Nilakantan and Gillespie (2012) studied the effect of five different inter-yarn friction levels on fabric ballistic performance, and concluded that performance was proportional to inter-yarn friction levels for the two-sided clamped cases and inversely proportional to inter-yarn friction for four-sided clamped cases. Rao et al. (2009) sought to couple friction with material properties and boundary conditions for a given fabric geometry and projectile to obtain a more comprehensive understanding of ballistic performance. They concluded that friction helped improve performance of the fabric with higher stiffness and higher strength yarns. They also found that for low striking velocities below 100m/s, yarn-yarn friction was more important than projectile-yarn friction. Earlier studies by Tabiei and Ivanov (2002) showed that for impact velocities well above the ballistic limit of the fabric (usually meant to describe V_{50}, the velocity at which 50% of the impacting projectiles will be stopped by the target), projectile-fabric friction is more beneficial than yarn-yarn friction. Finally, Shim et al. (2012) considers energy dissipation due to both types of friction in experimental studies of oblique impact into woven fabrics and laminates.

For most, if not all the literature cited on ballistic impact studies, we observe at least one of the following drawbacks in each study: (1) one or more of the boundaries of the fabric region are clamped close to the impact location, (2) single fabric layer used for testing, (3) small target fabric size on the order of 50-200mm per side, (4) spherical ball-shaped projectile impacting at very low velocities, (5) energy absorption analysis. (1) - (4) reduces the realistic outcomes of the model, since it does not resemble actual real-life impact scenarios. For humans wearing body armor, there is no initial tension in the fabric, and therefore clamping down on any side (1) creates unrealistic wave reflections and boundary effects. The same boundary effects come into play for (3), as tension waves propagate on the order of 8000 m/s, and using such small pieces of target fabric does not resemble the real size of body armor. Also, a piece of body armor can consist of hundreds of individual layers compressed together, which also work together in stopping the projectile. Using a single layer for simulation (i.e., a single layer with an areal density of that of just one fabric layer rather than that of the entire system) practically ensures that perforation will occur right away, and thus, little insight can be obtained on how the fabric would behave to stop the projectile. On the other hand, impacting at very low velocities (4) compared to the ballistic limit is also not useful to understanding the mechanics of fabric behavior such as cone wave growth, especially with a spherical ball-shaped projectile whose shape and contact surface are not at all like that of a projectile's. Finally, while there have been detailed comprehensive numerical models that accurately portray the geometry of crimp (Fig. 1.6) and the forces for various types of yarn slip, nearly all the post-processing analysis of results are done from the perspective of energy absorption (5). While projectiles do have enormous kinetic energy and this energy does need to be absorbed for the projectile to be stopped, the shortcomings of this approach often involve thinking in terms of material toughness, such as ductility, fracture toughness, and/or energy absorbed in phase transitions. For this we take the example of nylon, a material no longer used in ballistic fabrics. Although nylon exhibits high strain energy in terms of its area under the stress-strain curve, it is not nearly as effective as stopping projectiles as fabrics such as polyethylene-based Dyneema or aramid-based Kevlar (Tabiei and Nilakantan, 2008). To understand the reasoning behind this, we often have to look beyond energy absorption and track the motion of individual yarns, whose failure criteria is based on maximum tensile strain. Phoenix and Porwal (2003) discusses the role of yarn elastic energy (a measure of toughness) coincidentally with other properties such as Young's Modulus and maximum tensile yarn strains, but notably points out that increasing this energy value may not improve ballistic performance if tensile wave speed is reduced in the process.

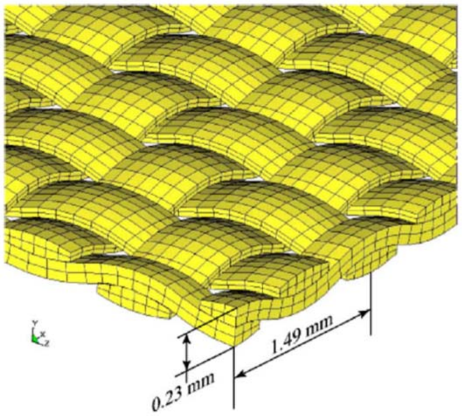

Figure 1.6. Detailed geometry of crimp shown in numerical model (Rao et al., 2009).

In this thesis we present two numerical models to describe zigzag out-of-plane crimp in laminar and woven fabrics. The first model, presented in Chapter 3, was developed to obtain general agreement with previous Cornell Phoenix Group's analytical models, which are summarized in Chapter 2. It also allowed us to experiment with implementing crimp as well as set parameters for controlling the stability of the numerical simulation. We also include the option of turning on projectile-yarn slip in this model for comparison with the no slip cases.

The second model, presented in Chapter 4, incorporates the over-under woven fabric geometry, with crossover points being a special focus. We define a set of new parameters (in addition to the ones from our first model) to account for yarn-yarn slip/sliding, compression at crossover points, and restoring forces.

In presenting our simulation results, we aim to study the changes in strain, velocity, and displacement fields over time, as well as the yarn de-crimping process. We write our code in MATLAB and do not use any commercial software packages, which has cut-down significantly on running time. Our simulation uses material properties of

Dyneema®, a UHMWPE fiber developed by DSM, a Netherlands-based company, with which we have collaborated on various ballistic impact-related research topics since 2009.

CHAPTER 2

REVIEW OF CORNELL GROUP ANALYTICAL MODELS

2.1 Introduction

The Cornell Group under the direction of Prof. S. L. Phoenix has been conducting research on the ballistic impact problem since 2003 (Phoenix and Porwal, 2003; Phoenix et al., 2010; Phoenix et al., 2010). Before we present our newest numerical models which include features such as crimp, woven biaxial fabrics, and yarn slip, we first review the setup of the ballistic impact problem. Important findings are presented, taken from our group's various analytical models including the 1-D tape model, the 2-D membrane model, and the 2-D bi-axial model. In subsequent chapters, we will validate our analytical findings through numerical simulations, which will also provide further insight on details not observable due to simplifying assumptions made by the analytical derivations. For convenience, Table 2.1 summarizes the notations used for key quantities in the analytical derivations presented in this chapter.

Table 2.1: Summary of key quantities involved in analytical models

Notation	Definition
M_{p}	Mass of the projectile
h_{p}	Length of the projectile
V_{p}	Velocity of the projectile prior to impact
D_{p}	Projectile nose width and tape width
h	Effective thickness of a 1-D tape
E	Young's modulus of impact tape/membrane/fabric
ν	Poisson's ratio of impact tape/membrane/fabric
ρ	Density of impact tape/membrane/fabric
ε_{t}	Strain of fabric/target element
σ_{t}	Stress of fabric/target element
γ	Cone angle
a_0	In-plane tension wave velocity
r_{p}	Projectile nose radius
r_{c}	Cone wave radius
ε_{p}	Strain in fabric/target in contact with projectile edge
$\varepsilon_{\max}$	Highest strain (over time) occurring in fabric/target
$\varepsilon_{\mathrm{ult}}$	Ultimate tensile strength in single yarn (obtained experimentally)
Γ_0	Membrane to projectile areal density ratio, also the mass ratio
ψ	Normalized cone wave front radius
h_{f}	Membrane thickness
m_{p}	Mass of fabric/target in contact with the projectile
A_{p}	Area of projectile in contact with the target
$a_{0\mathrm{f}}$	In-plane tension wave velocity in the fabric/membrane
$a_{0\mathrm{y}}$	In-plane tension wave velocity in the yarn/fiber
K_{SC}	Ratio to define strain concentration due to tension wave collision
$\varepsilon_{\mathrm{SC}}$	Strain value due to tension wave collision underneath projectile
ε_{∞}	Steady state strain value at long times

2.2 Governing equations for 1-D tape impact analytical model

We consider the deformation of a 1-D tape illustrated in Fig. 2.1 with the following assumptions. The tape is linearly elastic, subject to transverse impact by a projectile of mass M_{p} and length h_{p}, traveling at velocity V_{p} prior to impact. The projectile is idealized as a flat rectangular nose with width, D_{p}, transverse to the tape axis and span, d_{p}, along it. It has tensile modulus *E*, Poisson's ratio ν, material density *ρ*, and rectangular cross-section with width D_{p} and effective thickness *h*. We also assume no rounding at the projectile edge, no deformation of the projectile over time, and that the tape is long enough so that no boundary effects need to be considered. We note that unlike classical 1-D wave theory of string motion, the tape from our model is initially un-tensioned and infinite in length.

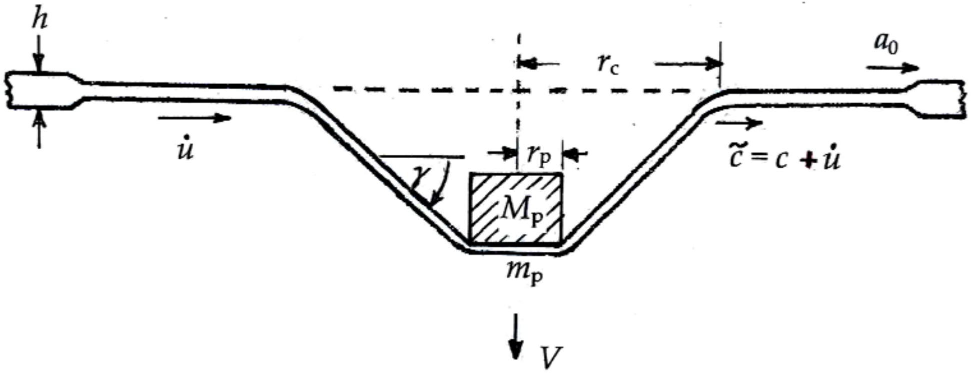

Figure 2.1. Schematic showing variables and geometry of tape impact problem. Material flows towards the projectile at velocity $\dot{u}$ and lowers triangle wave speed $\tilde{c}$ (ground coordinates) compared to *c* (material coordinates).

Using Cartesian coordinates (x, y) and assuming symmetric impact deformation of the tape with respect to the *y*-axis, we consider just the right half the plane ($x \geq 0$) in our analysis. At time $t = 0$, the tape lies on the line $y = 0$, and *x* represents the initial location of a tape material points. After impact, we define *u* and *v* to be the axial and transverse components of the displacement of this point, with new coordinates $(x+u, v)$. We mostly follow the approach provided by Rakhmatulin and Dem'yanov (1961) in the development and solution of two governing partial differential equations for tape displacement.

We start our analysis with a conservation of mass during deformation:

$$\rho A dx = \bar{\rho}\bar{A}\left(1+\varepsilon_{\mathrm{t}}\right)dx\,, \tag{2.1}$$

where Adx is the initial volume of a tape element, $A = D_{\mathrm{p}}h$ is its initial cross-sectional area and ρ its initial density. After deformation, $\bar{\rho}$, $\bar{A}$ and $\left(1+\varepsilon_{\mathrm{t}}\right)dx$ are, respectively, the element material density, cross-sectional area and length, and ε_{t} is the element strain, given by:

$$\varepsilon_{\mathrm{t}} = \sqrt{\left(1+\frac{\partial u}{\partial x}\right)^{2} + \left(\frac{\partial v}{\partial x}\right)^{2}} - 1\,. \tag{2.2}$$

For a tangentially aligned element shown in Fig. 2.2, at any given instant the forces acting on it are $-\bar{\sigma}_{\mathrm{t}}\bar{A}$ and $\bar{\sigma}_{\mathrm{t}}\bar{A} + \left\{\partial\left(\bar{\sigma}_{\mathrm{t}}\bar{A}\right)/\partial x\right\}dx$ where $\bar{\sigma}_{\mathrm{t}}$ is true stress.

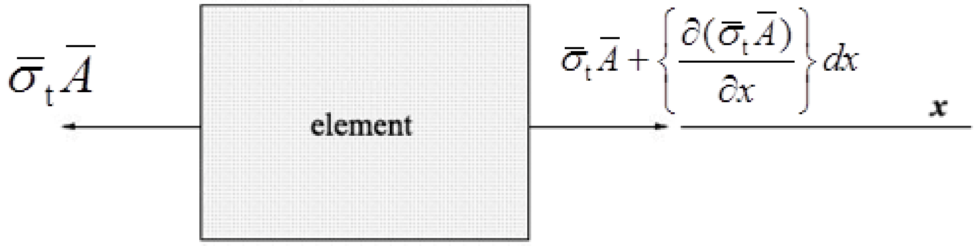

Figure 2.2. Element forces acting on a tangentially aligned material element.

We resolve these forces parallel to and perpendicular to the tape line and use conservation of momentum to obtain:

$$\rho A dx \frac{\partial^2 u}{\partial t^2} = \frac{\partial}{\partial x}\left(\bar{\sigma}_{\mathrm{t}} \bar{A} \cos\gamma\right) dx \tag{2.3}$$

and

$$\rho A dx \frac{\partial^2 v}{\partial t^2} = -\frac{\partial}{\partial x}\left(\bar{\sigma}_{\mathrm{t}} \bar{A} \sin\gamma\right) dx\,, \tag{2.4}$$

where γ is the inner angle (positive) between the tangent to the element surface and the tape axis, as shown in Fig. 2.1. We let σ_{t} be the engineering stress corresponding to $\bar{\sigma}_{\mathrm{t}}$ and from force balance get

$$\sigma_{\mathrm{t}} = \left(\bar{A}/A\right)\bar{\sigma}_{\mathrm{t}}\ . \tag{2.5}$$

We now substitute Eq. (2.5) into Eqs. (2.3) and (2.4) to obtain the governing partial differential equations (PDEs)

$$\rho \frac{\partial^2 u}{\partial t^2} = \frac{\partial}{\partial x}\left(\sigma_{\mathrm{t}} \cos\gamma\right) \tag{2.6}$$

and

$$\rho \frac{\partial^2 v}{\partial t^2} = -\frac{\partial}{\partial x}\left(\sigma_{\mathrm{t}} \sin\gamma\right), \tag{2.7}$$

where

$$\cos\gamma = \frac{1 + \partial u/\partial x}{\sqrt{\left(1 + \partial u/\partial x\right)^2 + \left(\partial v/\partial x\right)^2}} \tag{2.8}$$

and

$$\sin\gamma = -\frac{\partial v/\partial x}{\sqrt{\left(1+\partial u/\partial x\right)^2+\left(\partial v/\partial x\right)^2}} \ . \tag{2.9}$$

We aim to write Eqs. (2.5) and (2.6) in terms of the 1-D tensile wave speed, which is

$$a_0 = \sqrt{E/\rho} \ . \tag{2.10}$$

Since stress σ_{t} and strain ε_{t} are related by 1-D Hooke's Law $\sigma_{\mathrm{t}} = E\varepsilon_{\mathrm{t}}$ in this case, we can now use this and Eq. (2.10) to write Eqs. (2.5) and (2.6) as

$$\frac{1}{a_0^2}\frac{\partial^2 u}{\partial t^2} = \frac{\partial}{\partial x}\left(\varepsilon_{\mathrm{t}}\cos\gamma\right) \tag{2.11}$$

and

$$\frac{1}{a_0^2}\frac{\partial^2 v}{\partial t^2} = -\frac{\partial}{\partial x}\left(\varepsilon_{\mathrm{t}}\sin\gamma\right). \tag{2.12}$$

We do not include detailed derivations of the solutions to these PDEs here, but note that there are two distinct solutions, one representing the longitudinal tension wave and one representing the transverse, triangle-shaped cone wave. To obtain the final results presented in Section 2.4, it is crucial to implement the boundary condition which states that tension and cone wave fronts both coincide with the projectile radius at the instant of impact, or $t = 0$.

2.3 Governing equations for 2-D membrane impact analytical model

We now extend the ballistic impact problem to a thin 2-D isotropic membrane and present the process for determining its governing partial differential equations. We assume impact by a flat-nosed projectile with cylinder radius r_{p}, diameter $D_{\mathrm{p}} = 2r_{\mathrm{p}}$, and mass M_p. It travels at velocity V_p perpendicular to the membrane, and contact occurs over an area $A_\mathrm{p} = \pi r_\mathrm{p}^2 = \pi D_\mathrm{p}^2 / 4$. Similar to the 1-D tape, the membrane is initially un-tensioned and extends outwards infinitely with tensile modulus *E*, Poisson's ratio ν, thickness *h*, and density ρ per unit volume. We neglect compressive hoop stresses because tensile stresses are very large and the membrane is assumed to be thin and fibrous, and fibers and yarns will locally buckle to relieve them. Corresponding Poisson effects are also neglected.

The membrane deformation is assumed to be axisymmetric, therefore the analysis is done in cylindrical coordinates (r, ϕ, y), as illustrated in Fig. 2.3. At time $t = 0$, *r* and ϕ represent the initial radial and circumferential location of a fabric point in the membrane lying at rest at $y = 0$. After impact at time *t*, we define *u* and v to be the in-plane and normal (out-of-plane) components, respectively, of the displacement of this point, with the cylindrical angle ϕ remaining the same. We note that the new coordinates of this point now become ($r + u, \phi, 0 + v$), as shown in Fig. 2.3. We now follow the same procedure as presented in the previous section for obtaining the two governing partial differential equations.

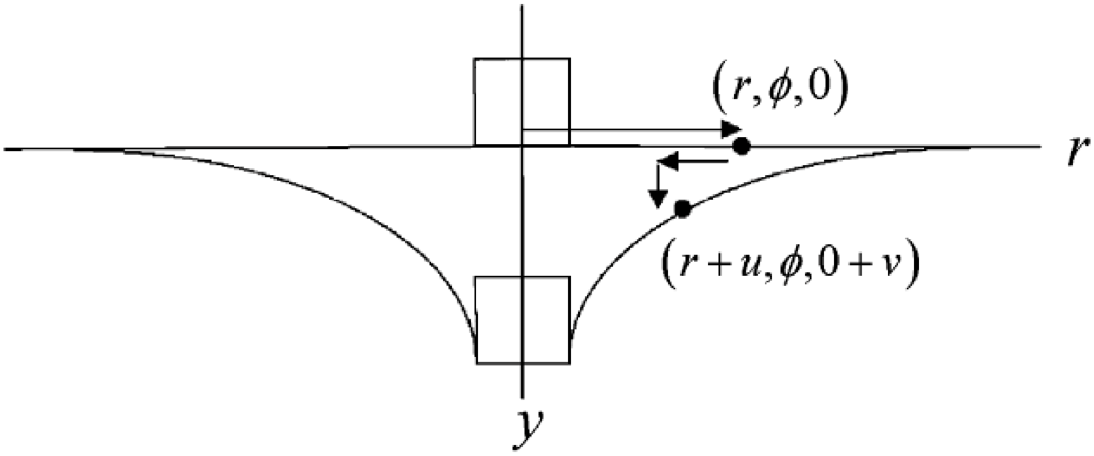

Figure 2.3. Cylindrical coordinate system (r, ϕ, y) and displacements (u, v) in a 2D membrane impact system where the cone has large angles and curvature.

We now apply conservation of mass during deformation for a membrane element initially of volume $hrdrd\phi$, thickness h, and density ρ:

$$\rho hrdrd\phi = \bar{\rho}\bar{h}(r+u)(1+\varepsilon_{\mathrm{t}})drd\phi, \tag{2.13}$$

where $\bar{\rho}$, $\bar{h}$, and $(1+\varepsilon_{\mathrm{t}})dr$ are the current density, thickness and length. Also, ε_{t} is the local in-plane strain oriented radially, given by

$$\varepsilon_{\mathrm{t}} = \sqrt{\left(1+\frac{\partial u}{\partial r}\right)^2 + \left(\frac{\partial v}{\partial r}\right)^2} - 1 . \tag{2.14}$$

The circumferential hoop strain ε_{ϕ} is

$$\varepsilon_{\phi} = u/r \ . \tag{2.15}$$

For any given time instant, the forces acting on the element locally in plane but radially oriented are $-\bar{\sigma}_{\mathrm{t}}\bar{h}(r+u)d\phi$ and $\bar{\sigma}_{\mathrm{t}}\bar{h}(r+u)d\phi + [\partial(\bar{\sigma}_{\mathrm{t}}\bar{h}(r+u))/\partial r]drd\phi$ where $\bar{\sigma}_{\mathrm{t}}$ is the true stress. It is also necessary to consider the resultant force from circumferential stresses resolved in the radial direction given by $-\overline{\sigma}_\phi \overline{h}(1+\varepsilon_{\mathrm{t}})drd\phi$ where $\overline{\sigma}_\phi$ is the true hoop stress. We resolve these forces parallel and perpendicular to the ground plane and use momentum conservation to obtain:

$$\rho hrdrd\phi \frac{\partial^2 u}{\partial t^2} = \frac{\partial}{\partial r}\left[\overline{\sigma}_{\mathrm{t}} \overline{h}(r+u)\cos\gamma\right]drd\phi - \overline{\sigma}_{\mathrm{t}} \overline{h}(1+\varepsilon_{\mathrm{t}})drd\phi \tag{2.16}$$

and

$$\rho hrdrd\phi \frac{\partial^2 v}{\partial t^2} = \frac{\partial}{\partial r}\left[\overline{\sigma}_{\mathrm{t}} \overline{h}(r+u)\sin\gamma\right]drd\phi\,, \tag{2.17}$$

where γ is the angle between the local tangential surface to the membrane element and the ground plane. We now express the ‘engineering’ stresses σ_{t} and ε_{t} in terms of the true stresses $\overline{\sigma}_{\mathrm{t}}$ and $\overline{\varepsilon}_{\mathrm{t}}$, and compare areas before and after deformation to obtain

$$\sigma_{\mathrm{t}} = \frac{\overline{\sigma}_{\mathrm{t}} \overline{h}(r+u)d\phi}{hrd\phi} \tag{2.18}$$

and

$$\sigma_\phi = \frac{\overline{\sigma}_\phi \overline{h}(1+\varepsilon_{\mathrm{t}})dr}{hdr}\,. \tag{2.19}$$

We now substitute Eqs. (2.18) and (2.19) into Eqs. (2.16) and (2.17) to obtain

$$\rho\frac{\partial^2 u}{\partial t^2} = \frac{1}{r}\frac{\partial(\sigma_{\mathrm{t}} r\cos\gamma)}{\partial r} - \frac{\sigma_\phi}{r} \tag{2.20}$$

and

$$\rho\frac{\partial^2 v}{\partial t^2} = -\frac{1}{r}\frac{\partial(\sigma_{\mathrm{t}} r\sin\gamma)}{\partial r}\,, \tag{2.21}$$

where

$$\cos\gamma = \frac{1+\partial u/\partial r}{\sqrt{\left(1+\partial u/\partial r\right)^2 + \left(\partial v/\partial r\right)^2}} \tag{2.22}$$

and

$$\sin\gamma = -\frac{\partial v/\partial r}{\sqrt{\left(1+\partial u/\partial r\right)^2 + \left(\partial v/\partial r\right)^2}}\,. \tag{2.23}$$

The stresses and strains are related by 2-D Hooke's Law, where

$$\sigma_{\mathrm{t}} = \left(\frac{E}{1-\nu^2}\right)(\varepsilon_{\mathrm{t}} + \nu\varepsilon_{\phi}) \tag{2.24}$$

and

$$\sigma_{\phi} = \left(\frac{E}{1-\nu^2}\right)(\varepsilon_{\phi} + \nu\varepsilon_{\mathrm{t}})\,. \tag{2.25}$$

The speed of tensile waves in the membrane propagating outward but in-plane is given by a_0, where $a_0^2 = E/[\rho(1-\nu^2)]$. We note that since this is the only place where ν appears in the governing equations, and since neglecting ν in a_0 results in less than 5% error (for ballistic materials), we do not include Poisson effects in our analysis, and the tensile wave speed thus reduces to its 1-D form, given by Eq. (2.10).

We initially keep the hoop stress term from Eq. (2.20) to see what role it might play in results, but since all hoop stresses prove to be compressive, we will ultimately neglect them. We observe that membranes and fabrics cannot support significant in-plane compressive stresses due to buckling of yarns. Eqs. (2.20) and (2.21) now become:

$$\frac{1}{a_0^2}\frac{\partial^2 u}{\partial t^2} = \frac{1}{r}\frac{\partial(\varepsilon_{\mathrm{t}} r\cos\gamma)}{\partial r} - \left[\frac{u}{r^2}\right]^{\oplus} \tag{2.26}$$

and

$$\frac{1}{a_0^2}\frac{\partial^2 v}{\partial t^2}=\frac{1}{r}\frac{\partial(\varepsilon_{\mathrm{t}} r\sin\gamma)}{\partial r}, \tag{2.27}$$

where $[\cdot]^{\oplus}$ indicates that the quantity only exists if it is positive. These equations, together with Eqs. (2.22) and (2.23), are the governing PDEs for the 2-D isotropic membrane impact problem.

2.4 Comparison of 1-D and 2-D model results

We present several important findings from the 1-D and 2-D analytical models, which are relatable to numerical simulation results from later sections. These analytical findings have been published and compared with experimental curves (Phoenix and Porwal, 2003), so we quote them on the premises that they have been verified already.

After impact, an initial tensile strain is generated at the projectile edge r_{p}, which is the fabric region where the highest strains occur over time, especially in the 2-D problem. Based on the 1-D tape model, we approximate this to be

$$\varepsilon\approx\left(\frac{V_{\mathrm{p}}}{\sqrt{2}a_0}\right)^{4/3}. \tag{2.28}$$

We also observe that since a_0 depends on fabric material properties and is constant throughout the impact, and V_{p} is always decreasing after impact. Thus in the 1-D problem ε would therefore be highest initially and decrease over time. This means that in the 1-D impact case, the highest strain $\varepsilon_{\max}$ is also the initial strain.

Since $\varepsilon_{\max}$ is often compared with ε_{ult}, the ultimate tensile strength in a single yarn (obtained experimentally), we can conclude that for a 1-D tape yarn failure, if it occurs, would occur at the beginning, or the instant right after impact, for a 1-D tape impact.

We now look at the same strain, but for the 2-D membrane impact case, given by

$$\varepsilon_{\text{p}} = \left(\frac{V_{\text{p}}}{\sqrt{2}a_0} \right)^{4/3} \psi^{1/3} \left(\frac{\sqrt{\psi/\varepsilon_{\text{p}}}(\psi - 1)}{\ln(1 + \sqrt{\psi/\varepsilon_{\text{p}}}(\psi - 1))} \right)^{2/3}, \tag{2.29}$$

where ψ, a function of time, is the normalized cone wave front radius $r_{\text{c}}/r_{\text{p}} > 1$ in terms of material coordinates. Example plots of Eq. (2.29) are shown in Fig. 2.4 (Porwal and Phoenix, 2005), where θ is a parameter (≥ 1) to account for the possibility of an effective impact radius larger than the nominal projectile radius r_{p}.

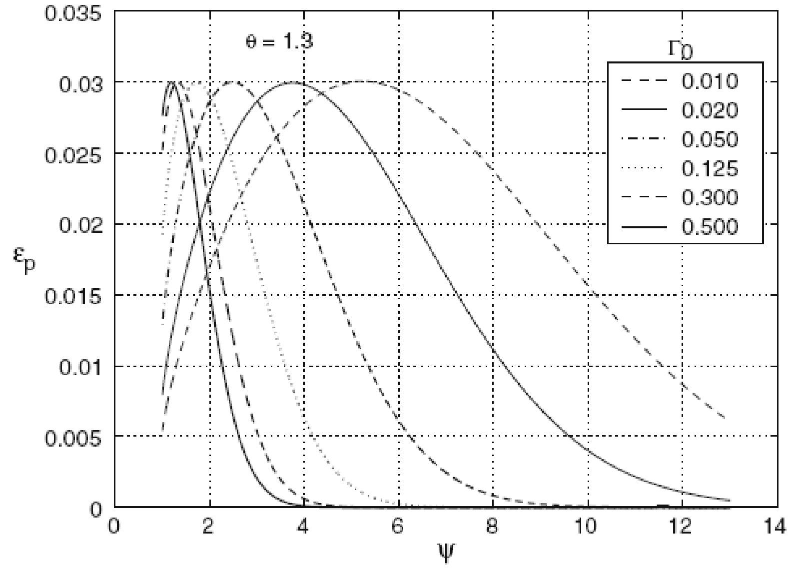

Figure 2.4. Plot of strain at the projectile edge ε_{p} versus normalized cone wave front ψ, which is a function of time.

The quantity, Γ_0, is the membrane to projectile areal density ratio, which is also the mass ratio, given by

$$\Gamma_0 = \frac{\rho h_\mathrm{f}}{(M_\mathrm{p}/A_\mathrm{p})} = \frac{m_\mathrm{p}}{M_\mathrm{p}}, \qquad (2.30)$$

where h_f is the membrane thickness, m_p is the mass of the fabric/target (in this case membrane) in contact with the projectile, and A_p is the area of the projectile in contact with the target, given by πr_p^2.

From Fig. 2.4, we first observe that the ε_p values for various Γ_0 all increase beyond their initial values (at $t = 0$ or $\psi = 1$) to a certain peak before decreasing for the remainder of time. (This decrease is the result of the projectile decelerating due to the out-of-plane membrane forces acting on it, the rate depending on Γ_0. Otherwise it would continue to rise indefinitely or until the material failed.) This differs significantly from what Eq. (2.28) describes for the 1-D case, where the initial strain ε is also the peak strain for all time. We explain this from a physical perspective by comparing the way material flows into the cone region between the two cases. In the 1-D case, no matter how far out the tension wave front has propagated, the amount of material suddenly pulled towards the center at velocity $\dot{u}$ is the same. In the 2-D case, the initial increase in strain is attributed to a rapid in-flow of material towards the impact center to create the cone wave and decelerate the projectile. However, after some time, as the tension amplitude decreases with increased circumference and there is also more material to be pulled in towards the center. Thus it becomes increasingly more difficult for material to be pulled in at the same velocity $\dot{u}$, as before. From this we can see that, in the 1-D case, yarn failure will either occur right away or not at all, whereas in the 2-D case, if yarn failure does not occur right away, it still may occur sometime later.

Another important insight, which we draw from Fig. 2.4 is the significant difference in the times when maximum strains occur between curves of different Γ_0 and combined with altering the impact velocity V_p to maintain the same peak strain. This shows that for projectiles of different mass (recall Eq. 2.30), such as the FSP and 9mm used in Chapters 3 and 4, the subsequent time of yarn failure can be drastically different. Fig. 2.4 shows that the greater the projectile mass, the longer it takes for ε_p to reach its peak. This makes sense physically, as it will take more time for the fabric to decelerate a heavier projectile versus a lighter one. (We should note here that ψ is not quite the same as time but the difference is modest because the transverse wave-speed is fairly insensitive to the parameters being varied in the plots.)

From the 2-D model, we also seek to distinguish yarn (or fiber) properties (subscript "y") from fabric (or membrane) properties (subscript "f"). The effective modulus of the fabric is $E_\mathrm{f} = E_\mathrm{y}/2$ due to crossing yarns adding extra mass and cross-sectional area but not contributing stiffness in the direction of wave propagation. Nevertheless, the fabric and yarn densities are identical, i.e., $\rho_\mathrm{f} = \rho_\mathrm{y}$. With this we calculate the actual longitudinal wave speed for the fabric along principal yarn directions as

$$a_{0\mathrm{f}} = \sqrt{\frac{E_\mathrm{f}}{\rho_\mathrm{f}}} = \sqrt{\frac{E_\mathrm{y}/2}{\rho_\mathrm{y}}} = \frac{a_{0\mathrm{y}}}{\sqrt{2}}\,. \tag{2.31}$$

This reduced tensile wave velocity in fabrics is well-documented in literature (Roylance et al., 1973; Figucia et al., 1982; Parga-Landa et Al., 1995). While we don't typically consider individual yarns in the analytical membrane model, the value of a_{0f} as some factor of a_{0y} will be interesting to track in our numerical model with yarn slip in Chapter 4.

2.5 Ongoing analytical studies on allowing slip to occur underneath projectile

For the 2-D membrane model presented in Section 2.4, we assumed a RCC (right-circular-cylinder) projectile with a flat nose but did not allow any slip to occur in yarns underneath the projectile. However, unlike the 2-D case, the 1-D case shows no sensitivity to projectile radius. Nonetheless, recent access to experimental data from DSM, the manufacturer of Dyneema®, has shown that the critical velocity for yarn failure (made from UHMWPE fibers) differed significantly between two projectile types: a flat-nosed reversed FSP projectile and a saddle projectile, both shown in Fig. 2.5.

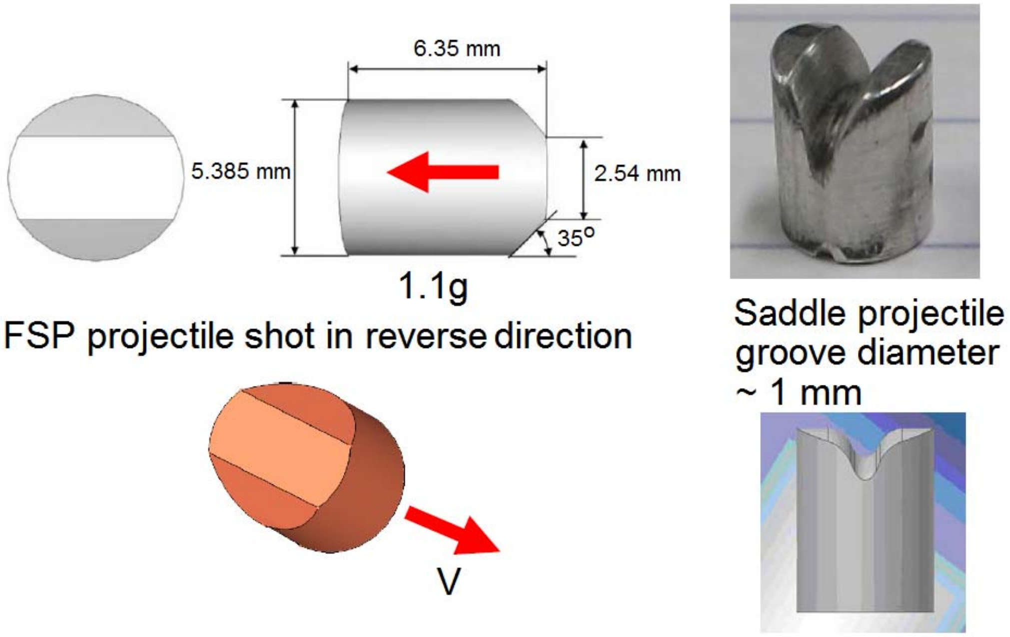

Figure 2.5. Comparison of FSP and saddle projectiles used in DSM's yarn shooting experiments.

In this section we quote several insights and findings from a pending journal paper (Phoenix, submitted). To explain why the critical velocity of the flat-nosed reversed FSP projectile was about 18% lower than the saddle projectile's critical velocity (which translates to a 25% difference in yarn strength), a wave-propagation model was developed that incorporates tension wave collision under blunt impact by a flat-faced projectile, in contrast to the simpler outward wave propagation in the classical model. However, we do not include equation derivations nor discuss all the findings from this paper, other than to select certain important results that relate to the results from our numerical models presented in subsequent chapters.

The reduction in yarn strength observed after shooting yarns with the two types of projectiles (Fig. 2.5) suggested that immediately following impact, the opposing tension waves emanating from the two edges of the flat-nosed projectile collide under the middle of the projectile, as shown in Fig. 2.6. As a result, symmetrically expanding tension wave is generated, which causes an increase in strain amplitude, which constitutes a strain concentration compared to the initial strain of the fabric in contact with the projectile edge right at the moment of impact.

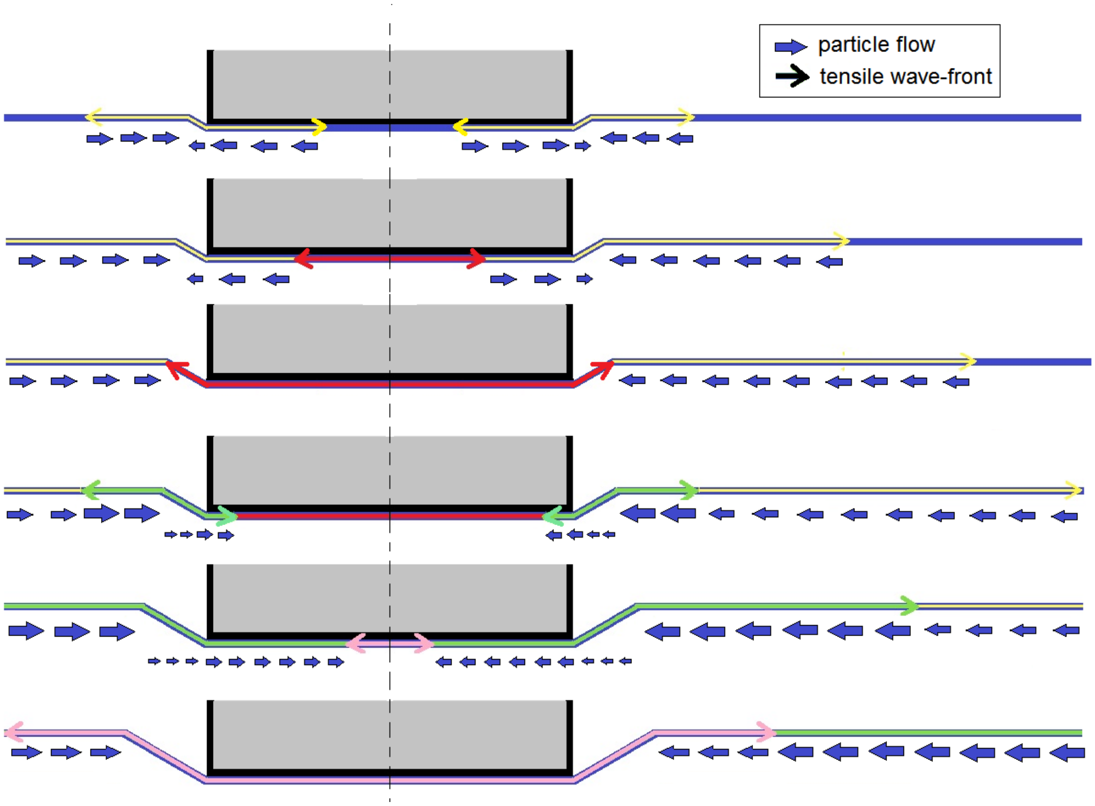

Figure 2.6. Evolution over time of the colliding tension waves and subsequent reflections under a flat-faced projectile impacting a frictionless yarn. Also shown is the direction of particle flow.

To quantify the effect of the shock wave on strain in yarns around the projectile edge, we define the variable K_{SC} to represent the strain concentration caused by tension wave collision under the projectile, $\varepsilon_{\mathrm{SC}}$, as compared to steady state behavior ε_{∞}, for the 1-D impact case:

$$K_{\mathrm{sc}} = \frac{\varepsilon_{\mathrm{SC}}}{\varepsilon_{\infty}}, \tag{2.32}$$

which becomes

$$K_{\mathrm{sc}} \approx \sqrt[3]{2}\left(1+\left(\frac{2^{2/3}-1}{3}\right)\left(\frac{V_{\mathrm{p}}}{2a_0}\right)^{4/3}-\frac{2^{1/3}}{3}\left(\frac{V_{\mathrm{p}}}{2a_0}\right)^{2/3}\right). \tag{2.33}$$

We note that typically $V_{\mathrm{p}} < a_0/20$, so $V_{\mathrm{p}}/(2a_0) < 1/40$. Therefore

$$\left(\frac{2^{2/3}-1}{3}\right)\left(\frac{1}{40}\right)^{4/3}-\frac{2^{1/3}}{3}\left(\frac{1}{40}\right)^{2/3} = 0.00367-0.0359 = 0.0322$$

Hence $K_{\mathrm{SC}} \approx \sqrt[3]{2}$ has an error of about 3%. This is a major result from the paper and will be revisited in Chapter 3. While there has been work done to derive an expression for K_{SC} like Eq. (2.33) for the 2-D case, we note that the 1-D expression is sufficient for comparison purposes with numerical results.

2.6 Summary

Chapter 2 is a review of selected aspects of the Cornell Group's analytical modeling work in the last decade. While the focus of this thesis is on developing numerical models to understand crimp and yarn slip in bi-axial fabrics, it is important to obtain agreement with previous analytical work in order to validate numerical results. Because many of the details incorporated into our numerical models have no corresponding place in the analytical models, we aim for qualitative agreement on general behavior and trends more than quantitative comparison.

The important analytical findings presented in this chapter are:

(1) Behavior of strain at projectile edge over time is different between 1-D and 2-D impact cases.

(2) The location of the peak strain attained by yarns at the projectile edge over time depends on Γ_0.

(3) Single yarn (1-D) properties such as tensile wave speed decreases when the yarns are part of a fabric.

(4) Allowing slip to occur underneath a flat-nosed projectile causes inward propagating waves to collide at the impact center, which leads to a strain concentration at the projectile edge, which causes a decrease in critical velocity.

CHAPTER 3

LAMINAR CRIMP MODEL FOR BI-AXIAL FABRICS

3.1 Introduction

Prior to the development of our numerical model, we first present a brief history of the coding process that arose from collaboration between Prof. S. L. Phoenix's Cornell Group and DSM, a Netherlands based company. This is followed by a review of several important qualitative observations from previous analytical modeling results as well as experimental findings that provide insight on post-ballistic fabric behavior.

DSM Dyneema®, a branch of DSM, is the manufacturer of Dyneema® fiber, a type of UHMWPE (Ultra High Molecular Weight Polyethylene) commonly used in personal body armor as well as military vehicles, bow strings, fishing lines, and ropes. Starting in 2008, the company sought to develop a relatively simple in-house code that could accurately model post-impact ballistic behavior without resorting to commercial Finite-Element Methods (FEM) such as LS-DYNA and AUTODYN, which were computationally demanding. Since the Finite-Difference Methods (FDM) for solving problems involving fabrics has been around for 30+ years and was relatively simple to incorporate, it was chosen for the initial version of the code, written in FORTRAN.

This model assumed (i) an RCC projectile where the mass of the projectile was evenly distributed (added) to all contact nodes, (ii) the system had no compressive strains, and (iii) the material behavior was linearly elastic. Fig. 3.1 shows assumptions (i) and (iii). All three assumptions were retained in our laminar crimp model, discussed extensively in this chapter.

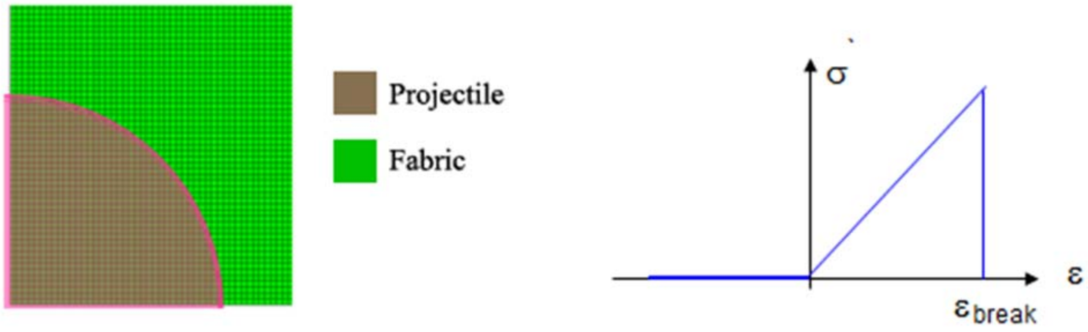

(a) (b)

Figure 3.1. (a) Schematic showing nodes as part of projectile contact, where the projectile mass was evenly distributed. (b) Assumption of linearly elastic material behavior in mass-spring system.

Several key features from the DSM simulation results appeared promising and provided more useful insights into the ballistic problem (versus the analytical model): (i) the ability to explicitly model progression of the tension and cone waves over time (including shape of waves at edges), (ii) the ability to track strains, forces, and positions in individual yarns via nodes, (iii) its general agreement with analytical models in terms of qualitative ballistic behavior post-impact, and (iv) the simplicity with which additional features could be added, both in terms of new calculations within the code and new graphs to display different features.

The DSM code also had several key unresolved problems: (i) the jagged nature of the projectile edge due to the square mesh often caused "high strain concentrations" at certain edge locations that would not be representative of actual physical impact, (ii) similarly, the calculation for strain around the projectile edge would be affected by such concentrations and would therefore not be accurate, (iii) oscillations were prevalent in the plots, especially during the initial impact moments, which would often not subside over time and (iv) slip underneath the projectile was not considered, neglecting the impact of an initial shock wave on subsequent fabric behavior. Figures 3.2, 3.3, and 3.4 show the problems inherent in the original DSM simulation results.

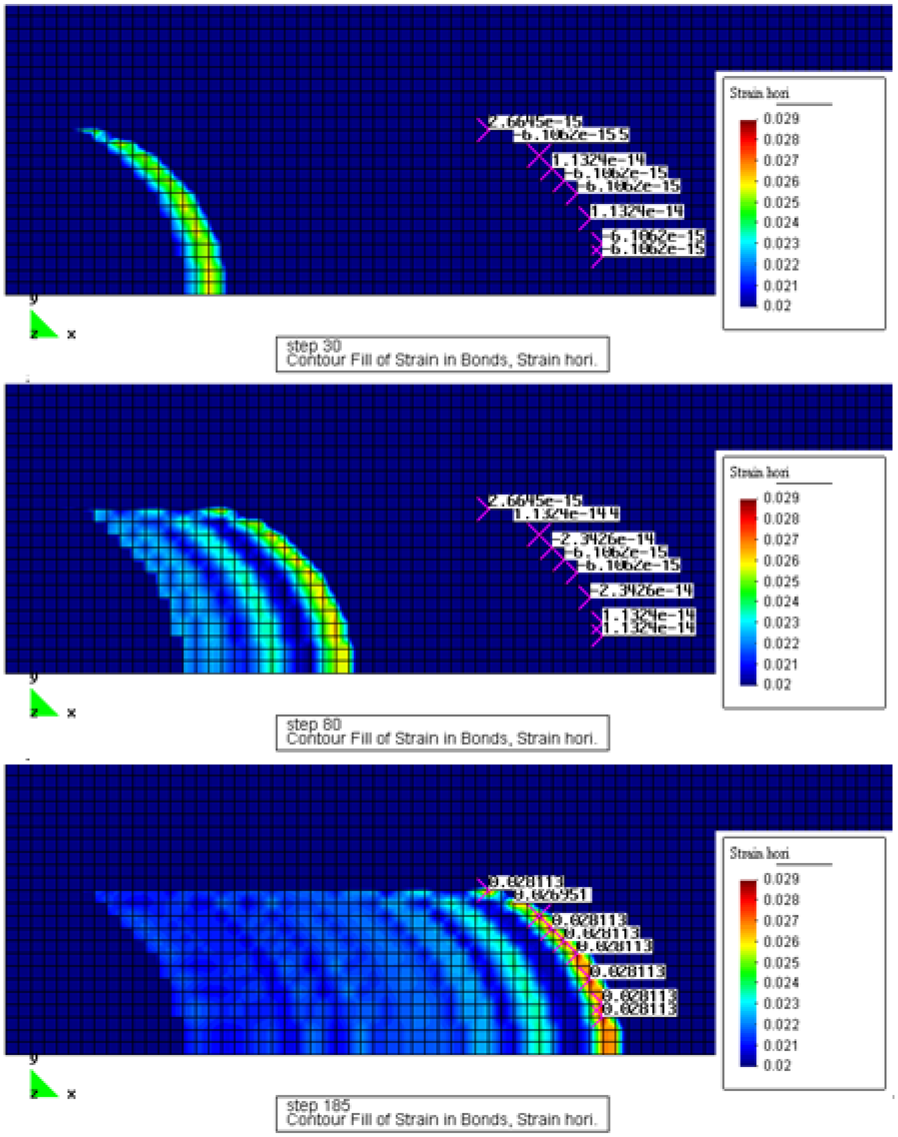

Figure 3.2. DSM simulation of tension wave in the fabric after impact at different times. We note that the wave progressions are discrete rather than continuous, and are thus inconsistent over the fabric material covered.

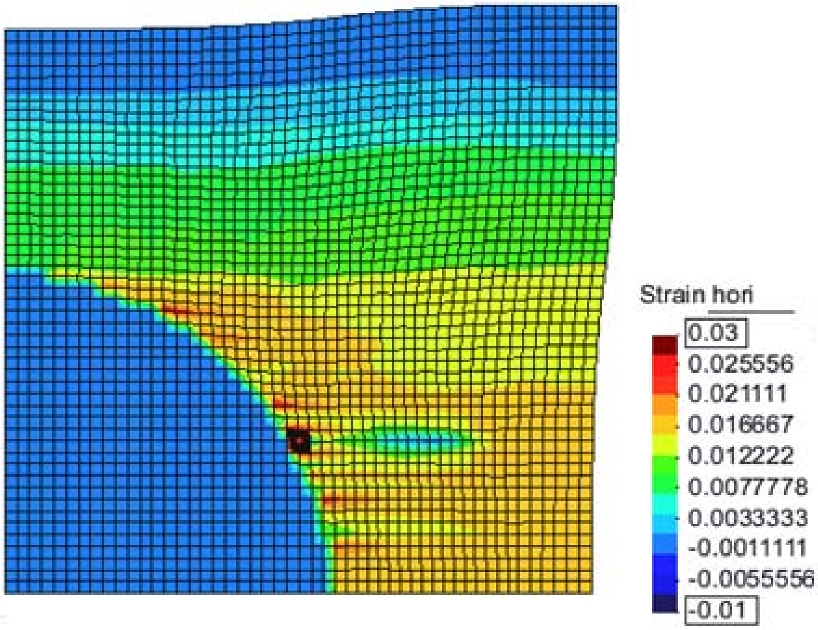

Figure 3.3. DSM simulation of horizontal strains in the fabric around the projectile after impact. The dark red point indicates where failure would occur. However, this may be a result of the jagged projectile edge rather than an actual physical phenomenon.

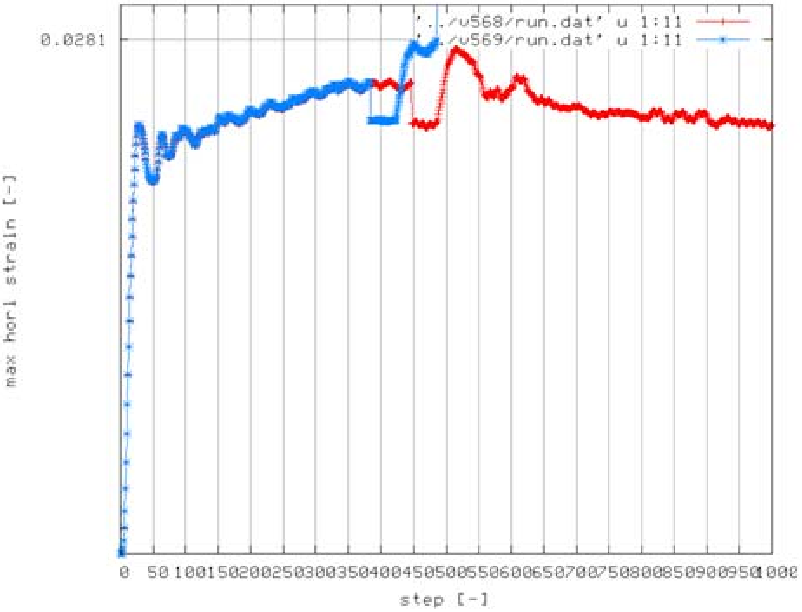

Figure 3.4. DSM simulation result of maximum horizontal strains in the fabric after impact over time. Oscillations are prevalent throughout the graph, reducing its accuracy.

We seek to address and resolve these problems in our numerical model described in this chapter, as well as implement crimp into the system. More complex features are implemented in the next model presented in Chapter 4.

Now we review several important qualitative observations from previous analytical modeling results as well as experimental findings that provide insight on post-ballistic fabric behavior. We note that qualitative and general observations are used for comparison rather than specific quantitative results because previous analytical models required many assumptions that simplify or omit certain impact conditions and parameters, and there has yet to be any quantitative experimental testing done for the cases we wish to examine in this dissertation.

The main observations are as follows:

1. Immediately after impact, tension waves rapidly propagate outwards along the principal yarn directions, pulling fabric material into the impact zone. This allows for the development and growth of a pyramid-shaped cone with rounded edges. The cone wave travels at a much slower velocity than the tension wave, and its existence has been well-documented by experimental and numerical results, as shown in Fig. 3.5. From an overall perspective, Fig. 3.6 shows, schematically the position, shape, and progression of the tension and cone waves following impact. Two distinct analytical solutions to the ballistic impact problem proving the existence of tension and cone waves are provided in previous publications from the Cornell Group (Phoenix and Porwal, 2003).

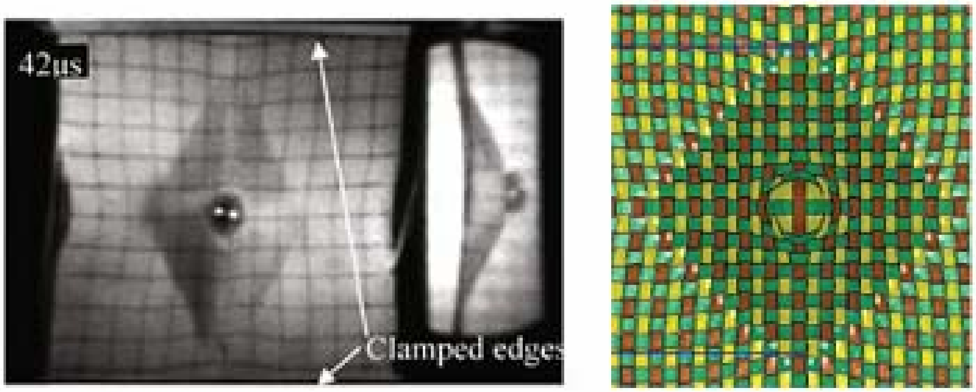

(a) (b)

Figure 3.5. (a) Image taken of ballistic fabric post-impact, showing the pyramid-shaped cone (Tan et al., 2008). (b) Simulation of cone wave through finite-element analysis (Chocron, et al., 2010).

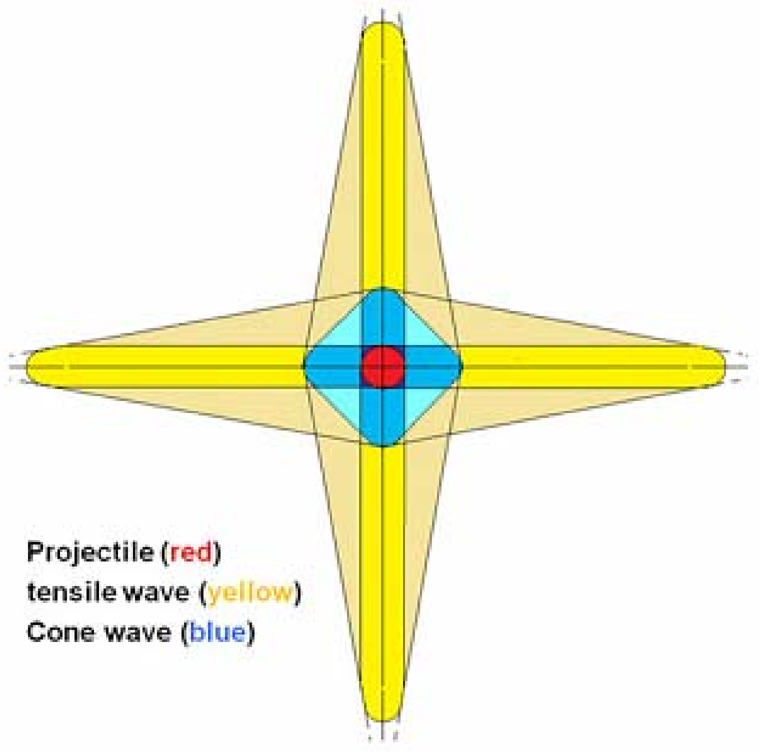

Figure 3.6. Top-down schematic of post-impact projectile behavior with tension and cone wave positions, shapes, and progressions shown relative to each other and projectile.

2. Maximum yarn strain is the failure criteria used by industry for testing ballistic fabrics and yarns. From previous publications (see Chapter 2), we note that out of all the yarns in the fabric, the ones that have the highest strain post-impact, and are therefore most likely to fail, are the ones in the region around the projectile edge. We plot the highest of the strains in this region over time, and observe that except for the 1-D impact case, these strains will always build up to a certain point before decreasing again. Figure 3.7 shows past analytical modeling results (2-D membrane, membrane with more than 1 layer, and bi-axial fabric), which all agree with this observation.
3. Fig. 3.7 also shows that depending on the dimensions of the projectile, the times at which yarn strains around the projectile edge reach their peak will be very different. In the figure, the smaller FSP's strain reaches its maximum much earlier than the larger 9mm's strain. This is important because from a timing and back face signature (BFS) (National Institute of Justice Standards, 2008; NATO Standardization Agreement, 2003; Department of Defense Military Standard, 1997) perspective, we can conclude that if the FSP causes fabric failure, this will occur almost immediately. On the other hand, if the 9mm causes fabric failure, this would occur much later, after the projectile has advanced farther in terms of displacement and the cone wave has grown considerably. We note that the trend described holds true regardless of impact velocity and yarn stiffness. Later analytical work with bi-axial fabrics shows the trend to still hold.

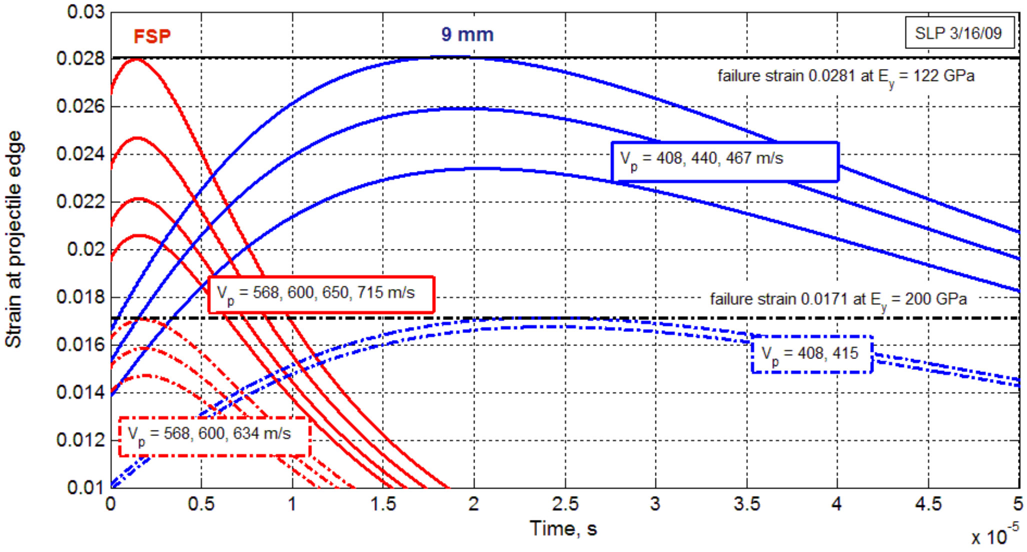
FSP
9 mm
SLP 3/16/09
failure strain 0.0281 at E_y = 122 GPa
V_p = 408, 440, 467 m/s
V_p = 568, 600, 650, 715 m/s
failure strain 0.0171 at E_y = 200 GPa
V_p = 408, 415
V_p = 568, 600, 634 m/s
Strain at projectile edge
0.03
0.028
0.026
0.024
0.022
0.02
0.018
0.016
0.014
0.012
0.01
0
0.5
1
1.5
2
2.5
3
3.5
4
4.5
5
Time, s
x 10^{-5}

(a)

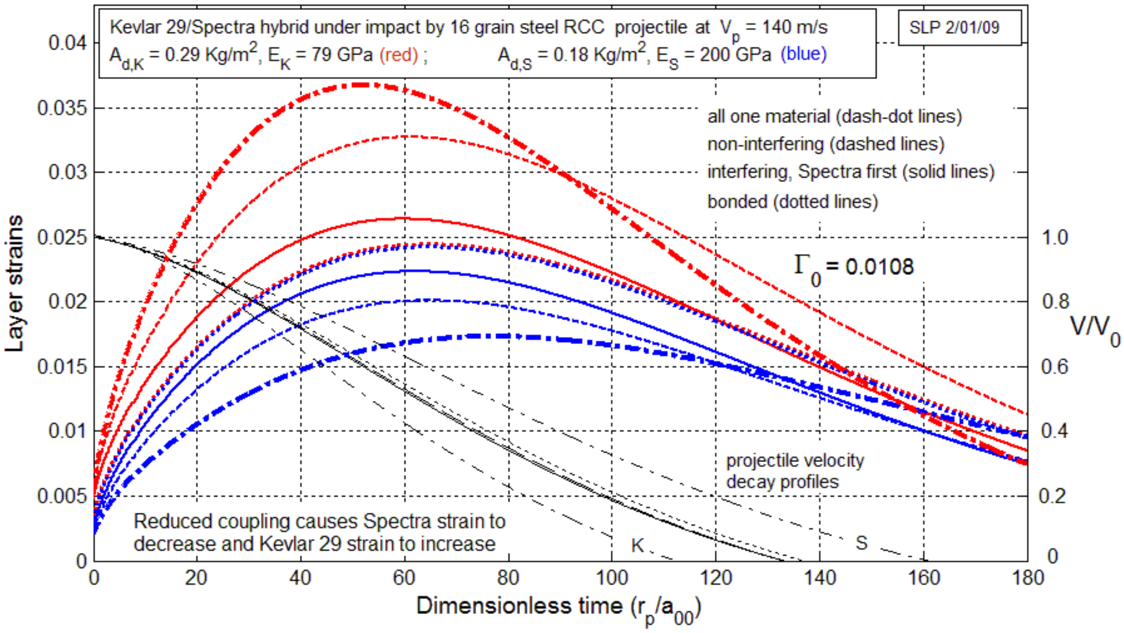
Kevlar 29/Spectra hybrid under impact by 16 grain steel RCC projectile at V_p = 140 m/s
$A_{d,K}$ = 0.29 Kg/m^2, E_K = 79 GPa (red) ; $A_{d,S}$ = 0.18 Kg/m^2, E_S = 200 GPa (blue)
SLP 2/01/09
all one material (dash-dot lines)
non-interfering (dashed lines)
interfering, Spectra first (solid lines)
bonded (dotted lines)
Γ_0 = 0.0108
projectile velocity decay profiles
Reduced coupling causes Spectra strain to decrease and Kevlar 29 strain to increase
K
S
Layer strains
0.04
0.035
0.03
0.025
0.02
0.015
0.01
0.005
0
V/V$_0$
1.0
0.8
0.6
0.4
0.2
0
0
20
40
60
80
100
120
140
160
180
Dimensionless time (r_p/a_{00})

(b)

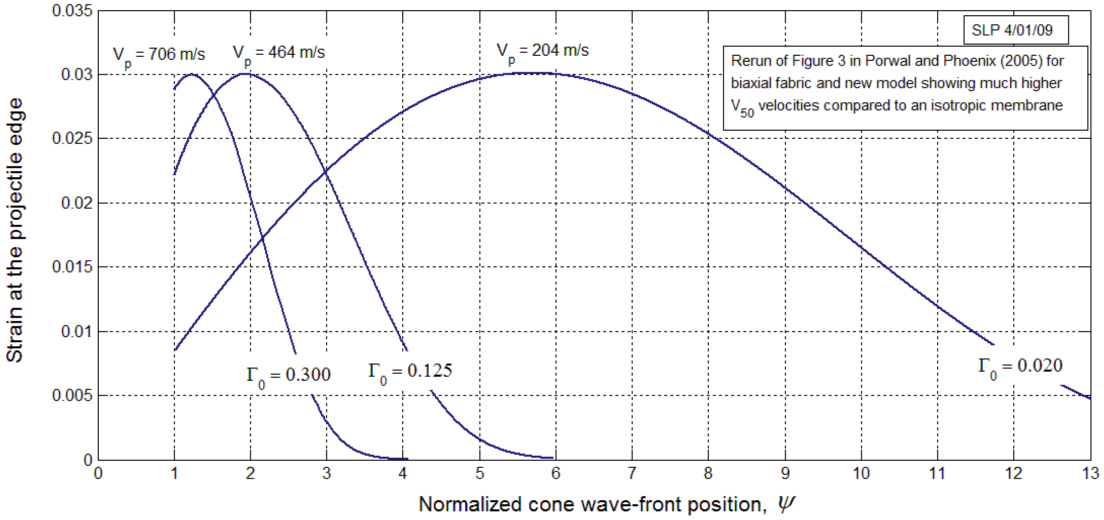

(c)

Figure 3.7. Cornell Group's analytical model results showing strain at projectile edge over time for (a) 2-D membrane (Phoenix et al., 2010), (b) more than 1 membrane layer (Phoenix et al., 2010), and (c) bi-axial fabrics where Γ_0 is the ratio of the mass per unit area of the fabric to the projected mass per unit area of the projectile.

3.2 Finite-difference numerical model

We choose a forward finite-difference (FD) method to numerically solve the ballistic impact into a laminar composite panel with imposed crimp problem. This method was chosen over the finite-element method due to its well-defined geometric representation of a bi-axial fabric, which allowed for straightforward spatial discretization into a rectangular grid. Prior to presenting our model, we lay out the following assumptions:

1. A flat-nosed, steel right circular cylinder (RCC) projectile with cylinder radius R_{proj}, mass m_{proj}, and initial velocity v_{proj}, is assumed to impact a bi-axial composite panel (with out-of-plane zigzag crimp) from a 90° perpendicular angle.

2. The projectile is rigid, therefore its shape does not change during the impact and deceleration process, i.e. R_{proj} is constant.
3. At the moment of impact, the instantaneous velocity drop is calculated using conservation of momentum between the projectile and the square patch of fabric material it contacts, resulting in a new velocity, $v_{\text{proj},0}$.
4. The fabric surface is defined such that it is large enough so that interference from wave reflections at the boundaries plays no role.
5. Deformation and shape change of the fabric were considered only up until the possible moment of perforation. This model does not allow for actual perforation to occur but assumes failure when the ultimate strain (experimentally determined) is reached in yarns.
6. Fabric perforation due to the projectile slipping between loosely arranged yarns without failing the yarns was not considered.

Further elaborations regarding these assumptions are presented in the subsequent sections of this chapter along with more specific modeling approximations.

For the laminar case presented in this chapter, we model the fabric panel in its un-perturbed state as a flat 2-D network of discrete, pin-jointed yarns where each node represents a cross-over point and has an assigned mass so that the areal density of the fabric is maintained fixed on a macroscopic scale. This is shown in Fig. 3.8(a). Also, all the masses are inter-connected by elastic spring elements representing the elastic properties, or stiffness, of the fabric. Fig. 3.8(b) shows this structural arrangement in more detail, along with how forces from neighboring springs affect each node.

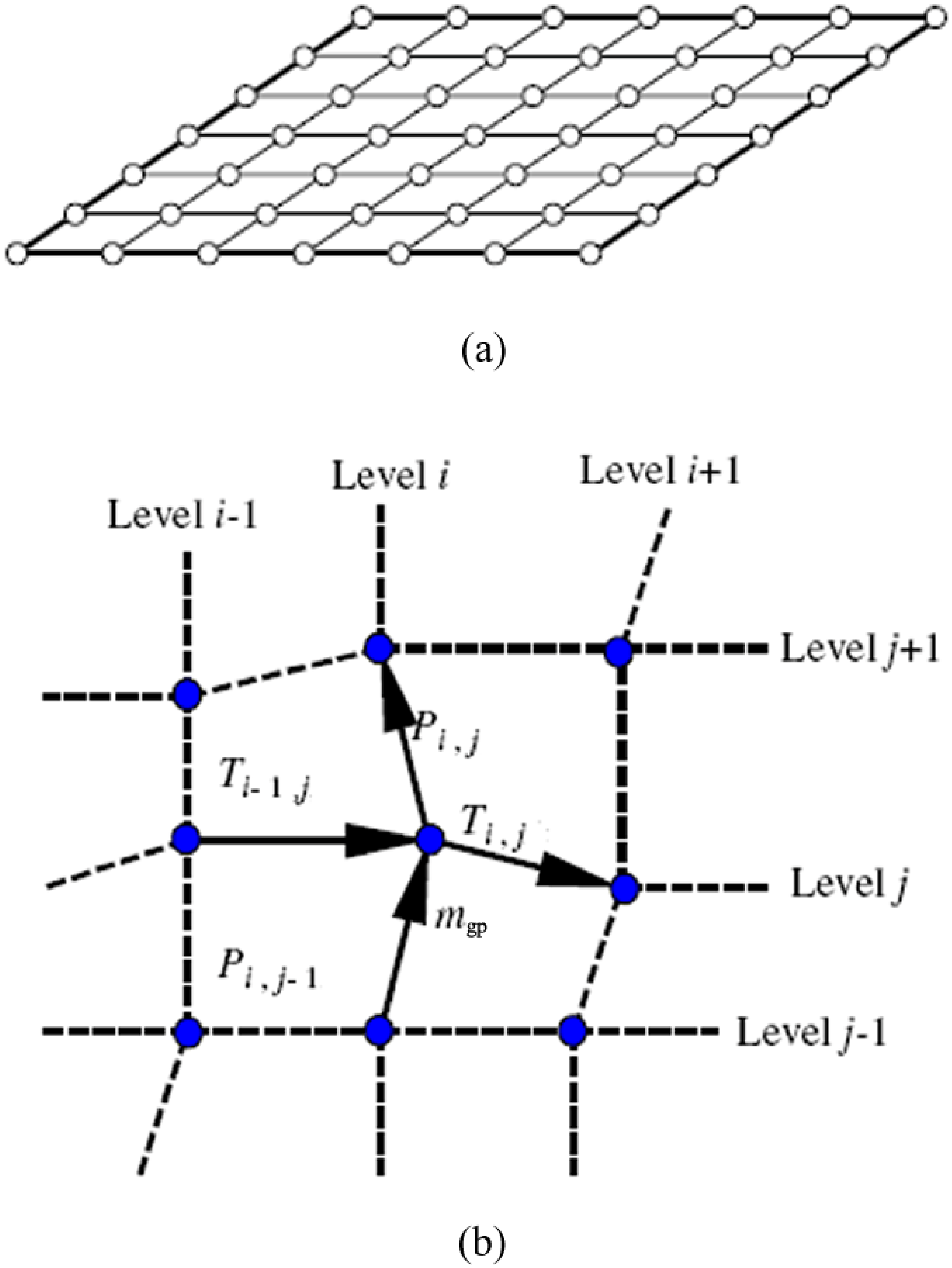

Figure 3.8. Pin-jointed network of discrete nodal masses representing the fabric panel (a) in an initial un-perturbed state (Tan et al., 2003), and (b) showing the effect of neighboring forces on a nodal mass where i and j number the nodes in the two orthogonal directions (Novotny et al., 2007).

To start the impact process, we assign the projectile velocity $v_{\text{proj},0}$ to all the nodal masses covered within its quarter-circle area, as shown in Fig. 3.9. This process of assigning masses and then velocities to nodes in contact with the projectile is explained more thoroughly in Section 3.2.4.

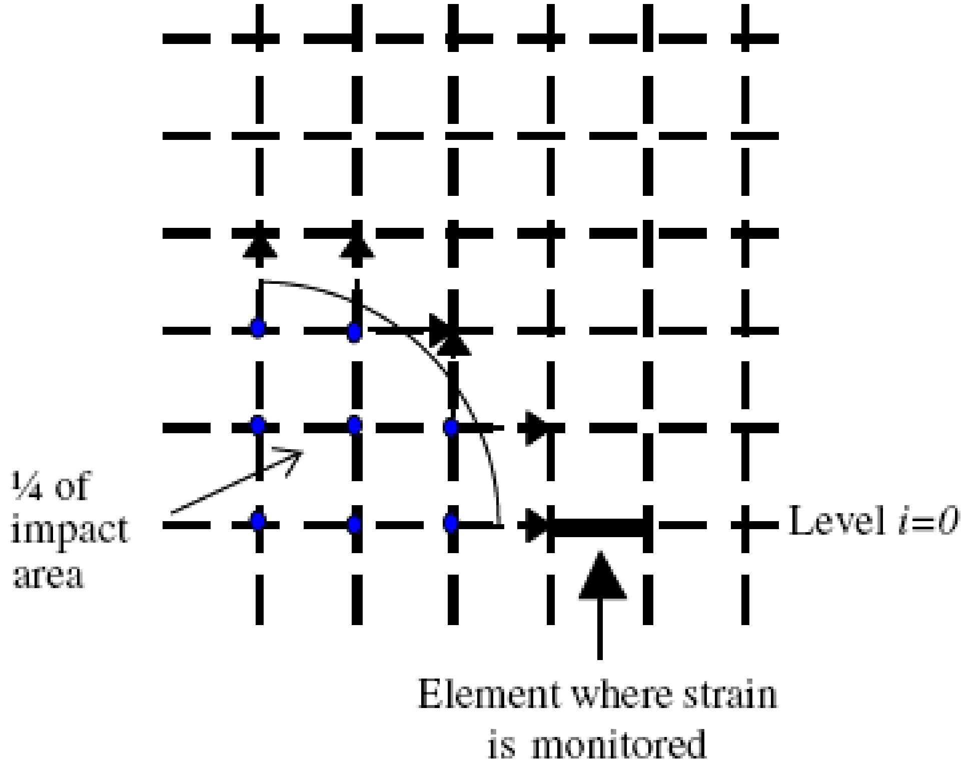

Figure 3.9. Due to *x*-and *y*-axis symmetry, we simulate one quarter of the impact area to conserve computational space. Here, the blue nodes represent nodes in contact with the RCC projectile, which has smooth round edges in reality (hence the circle outline), but can only be represented by "step-like" jagged edges on a square grid (Novotny et al., 2007).

We proceed to solve the Newtonian equation of motion in all three Cartesian coordinates for the current nodal velocities, written here in impulse-momentum format for a given time *t* and in the *x*-direction:

$$\frac{m}{\Delta t}(v_{(x)}^{t} - v_{(x)}^{t-\Delta t}) = \sum f_{(x)}^{t-\Delta t}\,, \qquad (3.1)$$

where $v_{(x)}^{t}$ is the current velocity component of the node in the *x*-direction and $f_{(x)}^{t-\Delta t}$ represents the projections in the *x*-direction of the tension forces applied to the node in the previous time step. According to Fig. 3.8(b), we can also write this as:

$$\sum f_{(x)}^{t-\Delta t} = \sum (T_{(x)}^{t-\Delta t} + P_{(x)}^{t-\Delta t}) . \tag{3.2}$$

We note that for the *y*- and *z*-directions, similar equations can be written. Once the velocity field has been determined, we use those values to solve for the nodal positions, written here for the *x*-direction at time *t*:

$$x^{t} = x^{t-\Delta t} + v_{(x)}^{t} \Delta t . \tag{3.3}$$

We then proceed to use the nodal positions to determine spring element lengths L^{t}, which are then used to solve for updated strains within the springs:

$$\varepsilon^{t} = \varepsilon^{t-\Delta t} + \frac{(L^{t} - L^{t-\Delta t})}{L^{t-\Delta t}} . \tag{3.4}$$

The strains are used in calculating tension forces T^{t} through a linear visco-elastic constitutive relationship such that

$$T^{t} = K\varepsilon^{t} + \Psi \Delta v^{t} , \tag{3.5}$$

where K represents the tensile stiffness (dependent on Young's modulus and cross-sectional area), Δv^{t} represents the relative motion of the nodes at the ends of a spring orthogonal to the spring's axis, and Ψ is a rocking viscosity coefficient applied to this motion for dampen oscillations. As subsequent results will show, these oscillations appear as a result of the explicit integration scheme used for temporal discretization and are thus products of the numerical simulation rather than the physical process.

3.2.1 Flow chart of algorithm

To provide a “big picture” perspective on how our laminar crimp model was programmed, we include a flow chart of the general algorithm, or design process, of the numerical code here, shown in Fig. 3.8(b). The process can be summarized in terms of four main steps: (i) setting input parameters and using those to allocate computational space and time, (ii) looping through each time step, (iii) looping through each grid-point or node in the fabric, and (iv) graphing final results. Details such as theory and reasoning behind specific coding decisions are presented in subsequent sections.

The accompanying legend to the flow chart on the next page is presented here in Fig 3.10(a). Box shapes, border colors, border line styles, connector colors, and text colors are utilized in various combinations to represent portions of the code with different functions and purposes.

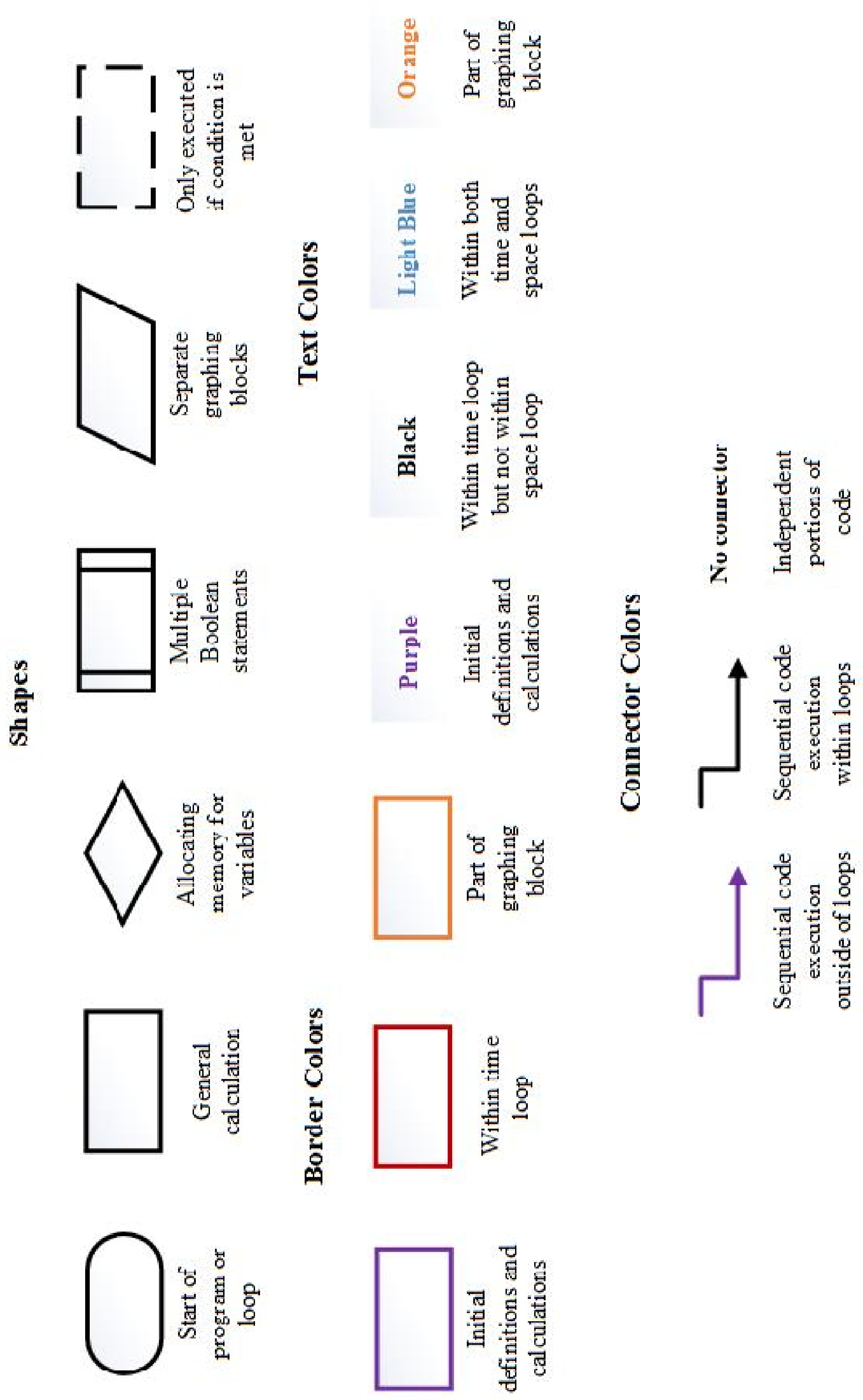
Shapes
Start of program or loop
General calculation
Allocating memory for variables
Multiple Boolean statements
Separate graphing blocks
Only executed if condition is met
Border Colors
Initial definitions and calculations
Within time loop
Part of graphing block
Text Colors
Purple
Initial definitions and calculations
Black
Within time loop but not within space loop
Light Blue
Within both time and space loops
Orange
Part of graphing block
Connector Colors
Sequential code execution outside of loops
Sequential code execution within loops
No connector
Independent portions of code

(a)

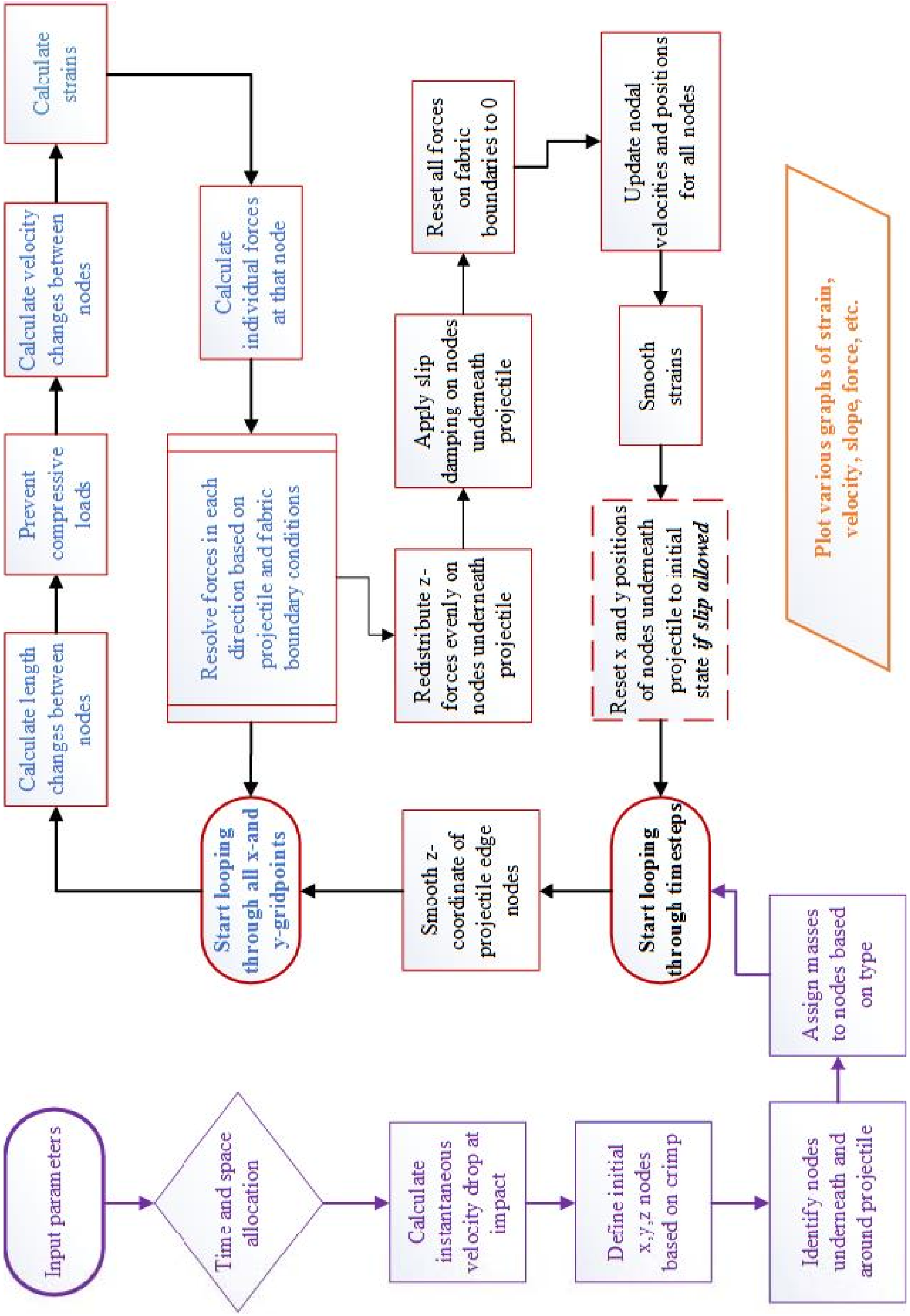

(b)

Figure 3.10. (a) Legend to reading part (b), the flow chart describing our programming algorithm

3.2.2 Initial input and calculated parameters

We present the list of parameters necessary to execute our numerical code in Tables 3.1 and 3.2, with each table representing either physical or simulation parameters, and each table separated into the user-defined inputs and the calculated dependent variables. The theory, reasoning, and possible equations behind the decision to use these parameters are discussed after each table.

Table 3.1: A list of physical parameters used as initial programming values

User-Input Parameters		
Name	Notation	Description
Ex	E_x	Young's Modulus in the x-axis
Ey	E_y	Young's Modulus in the y-axis
rho	ρ	density of fabric material
AD	AD	areal density of fabric material
v_proj	v_{proj}	projectile velocity right before impact
m_proj	m_{proj}	projectile mass
R_proj	R_{proj}	projectile radius
alpha	α	crimp factor
eta	η	rocking viscosity
zeta	ζ	slip (underneath projectile) viscosity
Calculated Parameters		
Name	Notation	Description
a0	a_0	tension wave velocity
d_panel	d_{panel}	thickness of fabric panel
ExA0	$E_x A_0$	panel tensile stiffness in x-direction
EyA0	$E_y A_0$	panel tensile stiffness in y-direction
v_proj0	$v_{\mathrm{proj},0}$	projectile velocity right after impact (momentum transfer)
m_gp	m_{gp}	mass of fabric per node
m_proj_gp	$m_{\mathrm{proj,gp}}$	mass of projectile per node

Alpha	A	ratio of extended yarn length from crimp to original length

E_x and E_y represent the Young's Modulus in the *x*-and *y*-directions, a condition of the bi-axial nature of the fabric. In our simulations, we use material properties of Dyneema® yarn and $E_x = E_y$.

ρ is the material density (kg/m^3) of the fabric, defined conventionally as mass per unit volume (without void space excluded).

AD is the areal density (kg/m^2) of the fabric, defined as mass per unit area.

v_{proj} is the projectile velocity (m/s) right before impact, which is set by the user to be any value of choice.

m_{proj} and R_{proj} are, respectively, the projectile mass (kg) and radius (m) determined by the type of projectile used. Parameter values used for the two types of projectiles simulated and presented in this thesis are presented in Section 3.2.4.

Crimp factor α is discussed in Section 3.2.5.

η is the rocking viscosity term (s/m) used for damping possible oscillations that occur in the nodes as a result of the nature of the FD incremental stepping scheme. It serves the same purpose as Ψ from Eq. (3.5), but has different units due to the format we chose to write our equations in while coding. ζ is the slip viscosity term (s/m) used for damping in-plane slip for nodes in contact with the projectile. Both are discussed in Section 3.2.7.

a_0 represents the tensile wave-speed propagating along a free-standing yarn, and is calculated using the definition of wave velocity in a thin rod where linear elasticity is assumed:

$$a_0 = \sqrt{E_x / \rho} \tag{3.6}$$

d_{panel} is the out-of-plane thickness (*Th*) of the panel of fabric used in our simulations, calculated by:

$$d_{\text{panel}} = \frac{AD}{\rho} = \frac{mass/area}{mass/volume} = \frac{mass/(dl \times dl)}{mass/(dl \times dl \times Th)} = Th \tag{3.7}$$

$E_x A_0$ and $E_y A_0$ represent the panel stiffness values in the *x*-and *y*-directions, and is the same as K from Eq. (3.5). It is calculated by using Young's Modulus and cross-sectional area:

$$E_x A_0 = dl \cdot d_{\text{panel}} \cdot E_x \, . \tag{3.8}$$

$v_{\text{proj,0}}$ is the projectile velocity (m/s) in the instant after impact, related to v_{proj} through a momentum transfer calculation:

$$v_{\text{proj,0}} = v_{\text{proj}} \cdot \frac{m_{\text{proj}}}{(\pi R_{\text{proj}}^2 \cdot AD + m_{\text{proj}})} \tag{3.9}$$

m_{gp} is the mass of the fabric per node, calculated by:

$$m_{\text{gp}} = AD \cdot dl^2 \tag{3.10}$$

$m_{\text{proj,gp}}$ is the mass of the projectile per node, calculated by dividing the projectile mass by the number of nodes covered by the projectile (which depends on projectile size) $n_{\text{proj,gp}}$. Exact calculations are presented in Section 3.2.4.

Alpha is a crimp-related length ratio, calculated by using α, and is discussed in Section 3.2.5.

Next, we list the key parameters that are not properties of the physical system or part of the ballistic impact problem described in the previous chapter, but rather simulation variables necessary to execute our numerical F-D program.

Table 3.2: A list of simulation parameters used as initial programming values

User-Input Parameters		
Name	Notation	Description
c1	c_1	coarseness of mesh
c2	c_2	boundary factor
c3	c_3	patch size factor
Taccel	T_{accel}	time accelerator
Tau	τ	approximate time length of run
Calculated Parameters		
Name	Notation	Description
n_steps	n_{steps}	actual number of time steps
n_elem	n_{elem}	number of element spacings in the entire fabric square
ne0	n_{e0}	number of nodes stored in patch around projectile
n_c	n_{c}	point at cone wave front
dl	dl	grid size
dt	dt	time step size
k	k	number of projectile grid points along axis
k1-k4	$k_1 - k_4$	various fractions of k used for smoothing
TAU	T	exact time length of run as a dimensionless quantity

We note that $c_1 - c_3$ are all user-entered, dimensionless factors used for the allocation/calculation of time and space for each simulation run. c_1 determines how detailed the grid-meshing or spatial discretization will be, where lower values indicate more detail and higher values less detail. c_2 indicates how close to the boundary of the fabric the tension wave will be allowed to travel, where lower values indicate greater proximity and higher values less proximity. Hence, it is also used to determine the overall size of the fabric square to be used in the simulation. c_3 is the patch size factor, which determines the size of the fabric square to be used in the simulation. We observe that c_2 values should typically be no less than 1.5 in our model to prevent wave reflections or other boundary effects. Since the tension wave travels very rapidly along the yarns, in order for its entirety to be seen in a plot, we usually set the c_3 value to be no less than $\tau - 1$. However, for larger τ values, this setup was often not feasible due to limitations in our available computation memory. For those cases, we set the c_3 values to be much smaller than τ, and as a result only a fraction of those tension waves showed up in plots (although the critical region around the projectile is always captured). Fortunately, this only affects plotting, and not the actual calculated values.

T_{accel} is the time accelerator factor that determines the coarseness of time discretization, where lower values indicate more detail and higher values less detail. For stability purposes, we usually set this value to 1.

τ is the user-entered dimensionless time length of run, which is an approximation or estimate of the actual dimensionless time quantity T.

From the calculated listed of parameters in Table 3.2, we note that n_{steps}, n_{elem}, and n_{e0} are all calculated from a combination of $c_1 - c_3$, T_{accel}, and τ. After impact, as the program progresses through time, it actually loops through each time step until n_{steps} is reached. Similarly, as the program progresses through space, i.e. the *x*-and *y*-directions covering the fabric area, it loops through each node where the upper limit is set by

n_{elem}. Since we are interested in the strain around the projectile, n_{e0} is used to set aside space in matrices intended for storing values only pertaining to that region.

From theory, we approximate the location of the cone wave front at the end of the time length of run by calculating n_{c} as a function of c_1 and τ. This value is calculated at the beginning and only used for reference purposes. No other values are dependent on it throughout the program.

We spatially discretize the fabric into equal-sized squares with side length *dl*, also known as the mesh or grid size (in meters). This value is determined from multiplying c_1 by a fraction of the projectile radius for stability purposes. Similarly, the time step increment *dt* also depends on the R_{proj}, c_1, and T_{accel}. For numerical stability, we require that Δ*t* be smaller than the time it takes for the tension wave to propagate through one element spacing *dl*.

In order to determine which nodes are impacted by the projectile, we first calculate *k*, the number of grid points (rounded down to nearest integer) along the axis covered by the projectile by:

$$k = \left\lfloor \frac{R_{\text{proj}}}{dl} \right\rfloor \tag{3.11}$$

Furthermore, because our mesh consists of square grids, but the actual projectile is round, we seek to smooth force and strain values around the projectile edge, particularly for plotting purposes. For purposes of strain smoothing, in order to determine how many grid points near the projectile edge (both inside and outside the projectile surface as well as in local, circumferential groupings) over which to average strains or apply tapers to displacements, we set values for parameters k_1 through k_4 as fractions of *k*. More figures and explanations of this process will be presented in later sections.

Finally, because our earlier, user-defined τ was an approximation, we now calculate the exact value of dimensionless time T, also shown as τ in graphs, by:

$$\mathrm{T} = \frac{n_{\mathrm{steps}} dt \cdot a_0}{R_{\mathrm{proj}}}, \tag{3.12}$$

where a_0 is the tension wave speed. This value of T represents the number of projectile radii traveled by a tension wave in a free standing yarn under impact. We note that the distance, in projectile radii, traveled by the actual tension wave observed in the model, will be somewhat less than T. A general summary relating dimensionless time T to its corresponding true time in μs is shown in Table 3.3. The true physical time that has passed in seconds can be obtained from $n_{\mathrm{steps}} dt$. We note that 9mm simulation cases were run for longer periods of time due to its characteristic of reaching peak strains much later than the FSP simulation cases.

Table 3.3: Dimensionless time corresponding real-time for two projectile types.

FSP										
T	1	2	3	4	5	6	7	8	9	10
time (μs)	0.38	0.76	1.14	1.52	1.90	2.28	2.66	3.04	3.42	3.80
9mm										
T	1	2	3	4	5	10	15	20	25	30
time (μs)	0.63	1.25	1.88	2.50	3.13	6.26	9.39	12.52	15.65	18.78

3.2.3 Fabric layout

For our FD simulation, we assume axial symmetry in the *x*-and *y*-directions, which also correspond to the weft and warp yarn axes. Therefore, we simulate and graph only one quarter of the fabric, chosen as the first quadrant.

In the laminar crimp model, the fabric system consists of inter-connected springs and masses, as shown in Fig. 3.11(a). With the exception of the nodes at the boundaries, each node is connected to four other nodes. Fig. 3.11(b) shows the corresponding fabric system at rest prior to impact as yarns in an un-crimped state. Fig. 3.11(c) shows a single un-deformed, un-crimped 3-D element with labels.

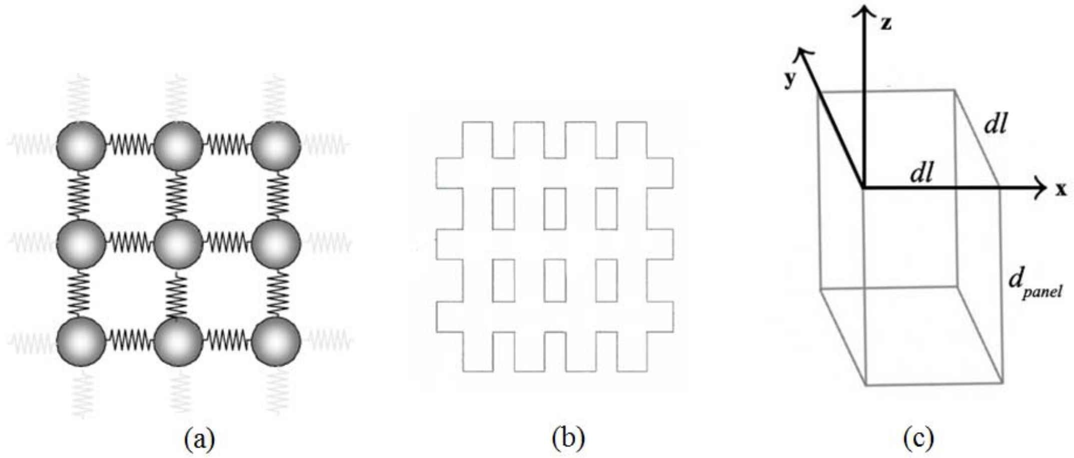

(a) (b) (c)

Figure 3.11. (a) Mass-spring system representing laminar geometry where each node is connected to 4 other nodes. (b) Schematic of (a) with yarns replacing springs and masses. (c) Single un-deformed, un-crimped element.

For each time step increment, nodal positions and velocities are updated using a forward time difference integration scheme. The nodal velocity at time $t+\Delta t$ is calculated by the same equation from Eq. (3.1), written in generalized vector form as:

$$\mathbf{v}_{t+\Delta t} = \mathbf{v}_t + \frac{\Delta t}{m}\sum \mathbf{f} \quad (3.13)$$

where $\mathbf{v} = (v_x, v_y, v_z)$ is a vector of the Cartesian nodal velocities, $\sum \mathbf{f}$ is the resultant force acting on the node from the tensions in the 4 connected yarn elements, and m is the mass of the node. Following this, the nodal position is updated by the generalized version of Eq. (3.3):

$$\mathbf{x}_{t+\Delta t} = \mathbf{x}_t + \mathbf{v}_{t+\Delta t}\Delta t\,, \tag{3.14}$$

where $\mathbf{x} = (x, y, z)$ is a vector of the Cartesian nodal positions. The force $\mathbf{f}$ is computed as a function of strains and relative velocities as given by Eq. (3.5) with further description in Section 3.2.7.

3.2.4 Projectile properties

We simulated ballistic impact using two types of projectiles, the Fragment Simulating Projectile (FSP) and the 9mm projectile. The former has a smaller radius, has less mass, and has a higher V_{50} than the latter in the particular Dyneema® panel considered for each, respectively. Property values used within the program for both types of projectiles are outlined in Table 3.4.

Table 3.4: Input values for two projectile types used in our simulations.

Projectile type	FSP	9mm
Projectile mass (g)	1.1	8.0
Projectile radius (mm)	2.73	4.5
Initial projectile velocity (m/s)	568	406
Dyneema® density (kg/m^3)	0.98	
Areal density (kg/m^2)	4.89E-03	3.00E-03
Young's Modulus (GPa)	101.26	
Strain failure criterion	0.0281	

We note that since the model only consists of a single structural layer, and yet we want to consider the behavior of a single layer as part of a multi-layer system, it was necessary to choose *AD* values that reflected a panel with many layers, perhaps bonded together, to yield d_{panel} much thicker than of a single fabric layer. Conversely, since real ballistic armor consists of multiple layers compressed together, with each layer being extremely thin, using the actual thickness of a layer would result in immediate failure, or penetration, upon impact.

Fig. 3.10 shows all the projectile edge nodes as modeled by our simulation. The difference between this and a perfectly smooth circular edge of a real projectile is evident. Even if the grid/mesh was set to be finer, similar jagged edges would still exist due to the square-by-square nature of our spatial discretization.

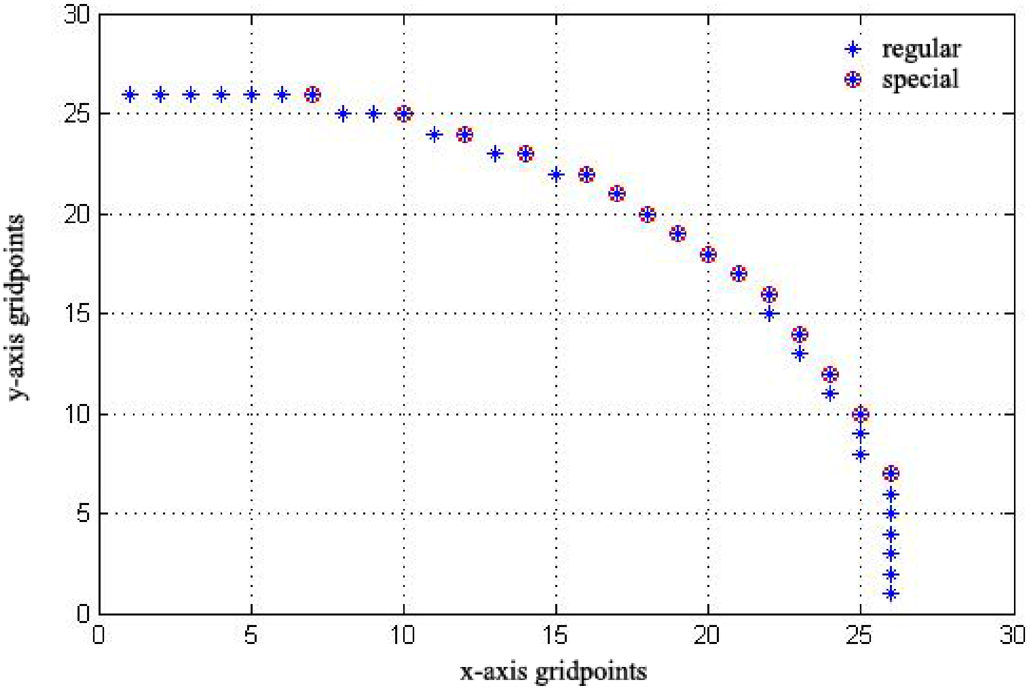

Figure 3.12. Example of simulated projectile edge nodes with grid origin at (1,1). Special nodes indicate locations where a "step" occurs in the jagged representation of a quarter-circle.

From trial-and-error, we observe that in nearly every variation of our numerical model, the special nodes from Fig. 3.10 turn out to be the problematic ones where huge strains occur. This often leads to numerous other unpredictable conditions, which may include overall instability of the simulation. More discussions of these are presented in Section 3.2.10.

To calculate how much projectile mass should be assigned to each node, i.e. the value of $m_{\text{proj,gp}}$, we first determine the value of k from Eq. (3.6). In the case of an FSP, we have:

$$k = \left\lfloor \frac{R_{\text{proj}}}{dl} \right\rfloor = \left\lfloor \frac{0.00273\text{m}}{1.092 \cdot 10^{-4}\text{m}} \right\rfloor = 25 \tag{3.15}$$

Next, we use the value of k to set the boundaries of the projectile, and then loop through all the nodes within (and on) the boundary to count for the total number of nodes representing the surface of the projectile, i.e. $n_{\text{proj,gp}}$. Then to calculate $m_{\text{proj,gp}}$, we have:

$$m_{\text{proj,gp}} = \frac{m_{\text{proj}}}{4n_{\text{proj,gp}} - 9k}, \tag{3.16}$$

where the factor of 4 accounts for the use of only one quadrant for our simulations, and the factor of 9 accounts for double-counting of the axiss nodes as well as edge smoothing.

For the nodes that are in contact with the projectile, we assign the sum of the projectile node mass $m_{\text{proj,gp}}$ and the fabric node mass m_{gp} as its nodal mass. We also assign $v_{\text{proj,0}}$ from Eq. (3.9) as the *z*-direction, or out-of-plane velocity to all those nodes.

3.2.5 Crimp

In a fabric with interlaced yarns, crimp is the out-of-plane undulation or waviness of a yarn and generally occurs in the yarns traveling in both directions, and the magnitude of the crimp is characterized relative to that of a perfectly straight yarn. While crimp is typically present in a yarn as a consequence of the weaving process, recent studies have shown that intentionally introducing crimp in a controlled way can improve its ballistic performance. In our modeling, for simplicity we assume a saw-tooth profile for yarn crimp, as shown in Fig. 3.13. The real path of a crimped yarn, however, is somewhere between a saw-tooth and a sinusoidal profile.

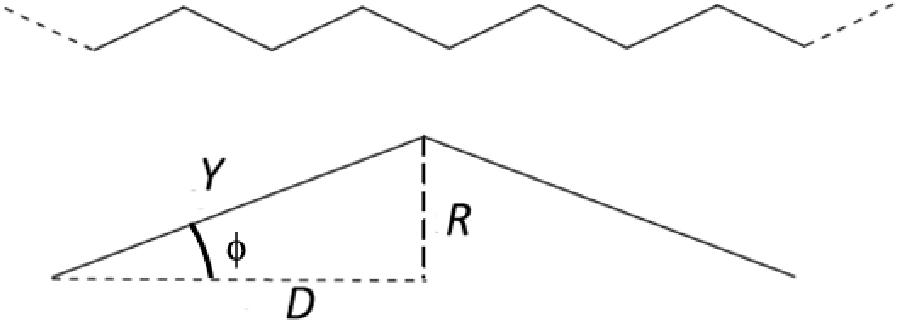

Figure 3.13. Saw-tooth profile of a single crimped yarn with key dimensions labeled according to ISO-7211-3 standard. In our model, *D* corresponds to dl.

To quantitatively characterize the level of crimp in a yarn, there are several commonly used definitions. The percent increase in yarn length due to crimp is defined in the international standard, ISO-7211-3 (ASTM International, 2008) as

$$C = \left[\frac{Y-D}{D}\right] \times 100\% \qquad (3.17)$$

Another intuitive way to define crimp is through the angle ϕ, in Fig. 3.13, also referred to as crimp angle or degree of crimp. Our code currently uses the relation defined by

$$\alpha = \tan(\phi) \tag{3.18}$$

as the crimp factor. From α, we also compute crimp-related length ratio A as one of the initial calculated parameters listed in Table 3.5:

$$\mathrm{A} = \sqrt{1+\alpha^2}\,, \tag{3.19}$$

which can be rewritten as a ratio through the following steps

$$\sqrt{1+\alpha^2} = \sqrt{1+\tan^2(\varphi)} = \sqrt{\sec^2(\varphi)} = \sec(\phi) = \frac{Y}{D} = \mathrm{A}\,. \tag{3.20}$$

Table 3.5 compares α, ϕ, C, and A values for the five test cases chosen for the simulations in our current study.

Table 3.5: Comparison of α, φ, C, and A values to represent crimp in each yarn.

		Crimp-related parameters			
		α	ϕ	C	A
Cases	A	0	0°	0%	1.00
	B	0.10	5.71°	0.496%	1.005
	C	0.15	8.53°	1.12%	1.011
	D	0.24	13.6°	2.84%	1.028
	E	0.366	20.1°	6.49%	1.065

From the table, it can be seen that while the crimp angle ϕ can reach relatively steep angles such as 20.1°, the corresponding increase in yarn length is still relatively small at 6.49%. Also, Case A ($\alpha = \phi = C = 0$) represents the perfectly straightened yarn with no crimp, and we often used it as the standard to compare other cases to. The values used in Cases D and E were taken from previously published literature (Chocron, et al., 2010; Rao, et al., 2009).

The process in which a yarn transforms from an originally crimped state to an un-crimped state (like Case A) is referred to as de-crimping. Physically, the yarns are straightened and flattened, and any angle or waviness is removed, as shown in Fig. 3.14. From this cross-section taken of a single yarn during the de-crimping process, we can see the range of crimp in the yarn from the vertical span. Zone 1 represents the completely de-crimped segment of the yarn. Zone 2 represents the partially de-crimped segment. Zone 3 represents the un-crimped segment.

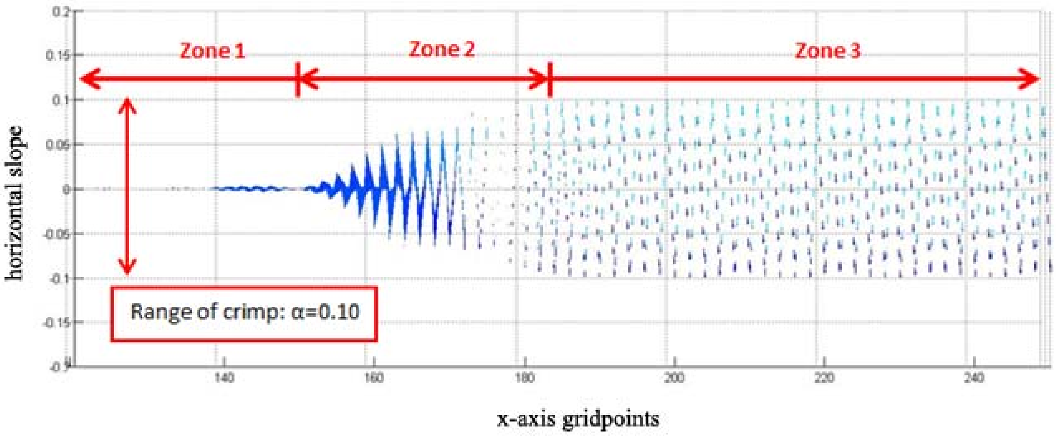

Figure 3.14. Section of a single yarn. Zone 1 is completely straightened and flattened by the traveling tension wave. Zone 2 is currently undergoing de-crimping. Zone 3 is still fully crimped, where the tension wave has yet to reach.

In our laminar crimp code, the initial definition and set-up for zigzag crimp was implemented by assigning either an “up” or “down” *z*-position for alternating nodes, as shown in Fig. 3.15(b).

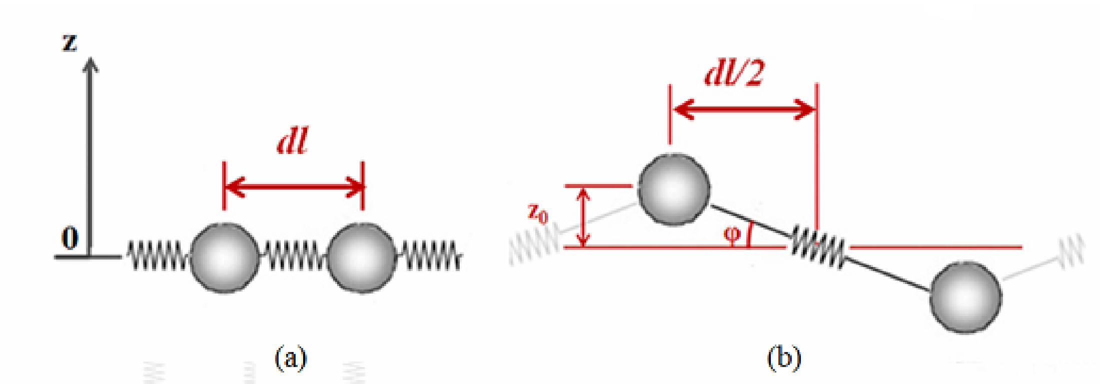

Figure 3.15. (a) Case A: single yarn element with no crimp. (b) Zigzag crimp state, where z_0 corresponds to R/2 from Fig. 3.11.

Compared with the no crimped state where the initial *z*-positions $z_0 = 0$ for all *i,j*, the crimped state defines initial *z*-positions as

$$z_0 = \pm \alpha \frac{dl}{2}, \tag{3.21}$$

where the sign depends on the *i,j* permutation of that specific node. In this laminar crimp model, since each node is connected to 4 other nodes, an "up" node seen from the *x*-direction would also be an "up" node in the *y*-direction, shown in Fig. 3.16. The opposite condition applies for woven fabrics, as presented in the next chapter.

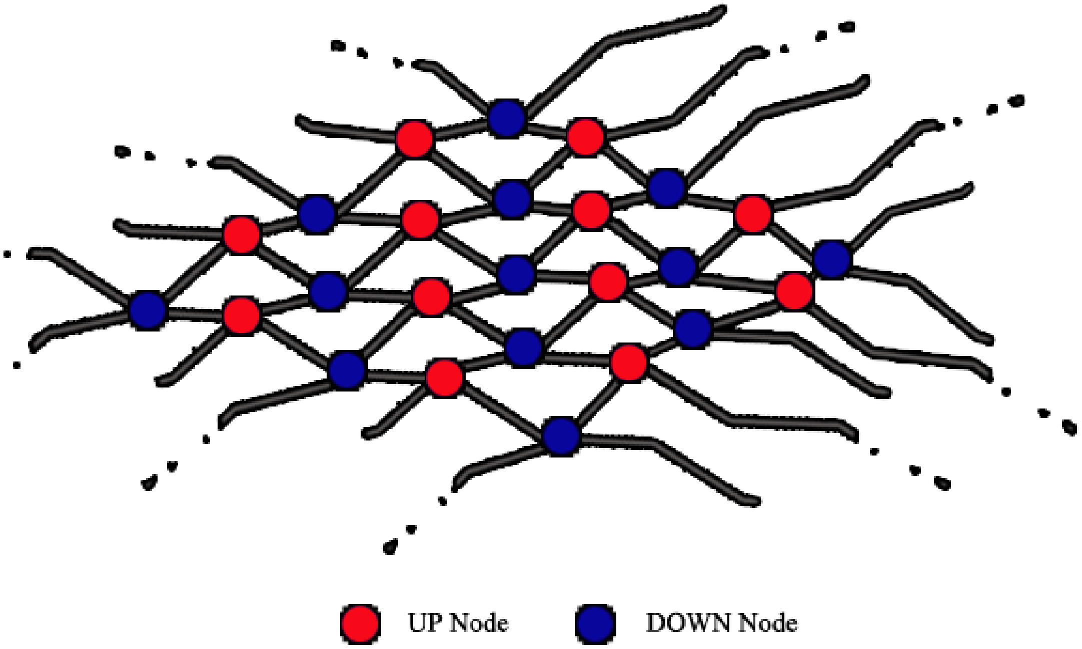

Figure 3.16. Network of nodes in crimped state for laminar model. Gray lines represent yarns, and colored circles represent assigned mass locations at nodes.

3.2.6 Strain and relative velocity calculations

We outline the steps taken to compute strains between two nodes. Our notation uses “hori” to denote the weft yarns and “vert” to denote the warp yarns. There are also x-and y-axes, which denote directions. Initially before impact, the “hori” and “vert” yarns are located exactly along the x- and y-directions respectively, and have no in-plane components in the other direction. However, this changes after impact. We therefore define certain length quantities to characterize the yarn deformation. For instance, x_{hori} describes the x-direction component of the hori yarn segments, and y_{vert}

describes the y-direction component of the vert yarn segments. The nodes, as usual, are defined by their i,j location.

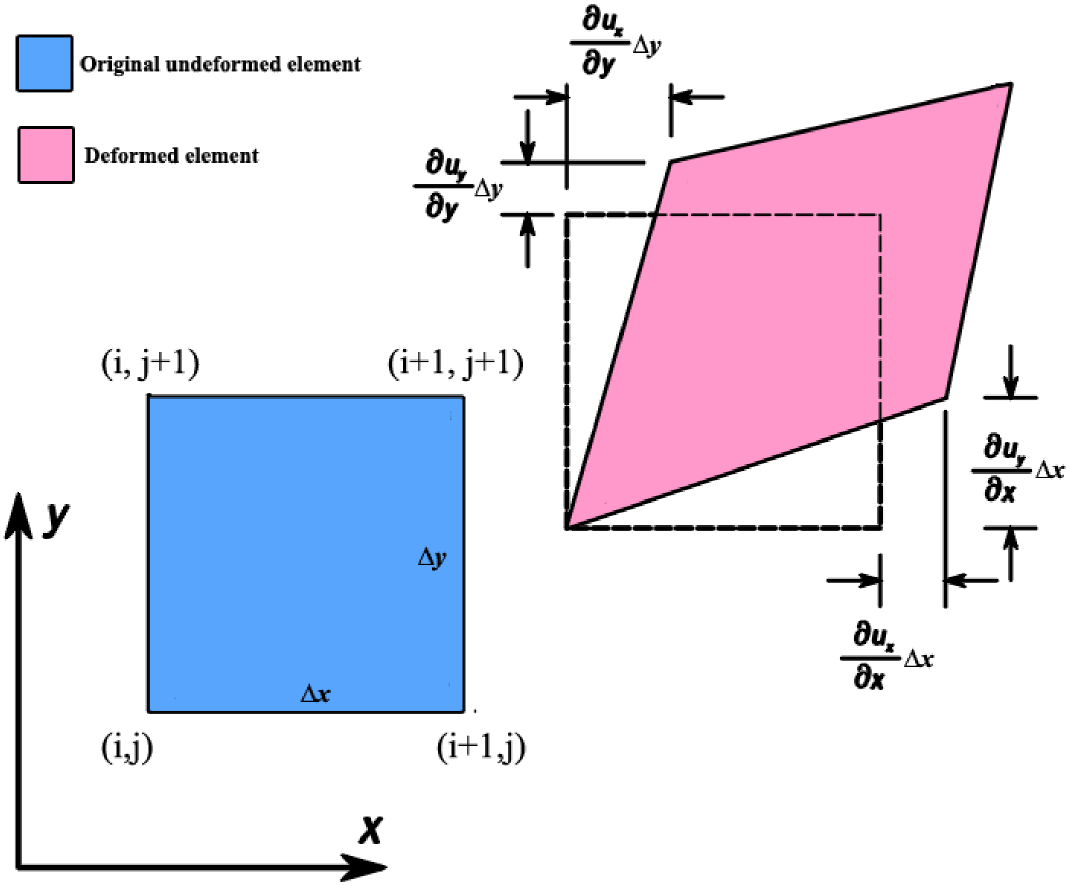

Figure 3.17. Two-dimensional geometric deformation of an infinitesimal material element where blue denotes the original element at time $t = 0$ and purple denotes the deformed element at time $t = \Delta t$.

Using the length definitions in Fig. 3.17, we first define the following lengths:

$$x_{\text{hori}} = \Delta x + \frac{\partial u_x}{\partial x}\Delta x = (1 + \frac{\partial u_x}{\partial x})\Delta x \tag{3.22(a)}$$

$$y_{\text{hori}} = \frac{\partial u_y}{\partial x}\Delta x \tag{3.23(a)}$$

$$x_{\text{vert}} = \frac{\partial u_x}{\partial y}\Delta y \tag{3.24(a)}$$

$$y_{\text{vert}} = \Delta y + \frac{\partial u_y}{\partial y}\Delta y = (1 + \frac{\partial u_y}{\partial y})\Delta y \qquad (3.25(a))$$

Since this is a 3-D problem, we also have the *z*-direction, or out-of-plane direction, which defines the *z*-component of the hori and vert yarns

$$z_{\text{hori}} = \frac{\partial u_z}{\partial x}\Delta x \qquad (3.26(a))$$

$$z_{\text{vert}} = \frac{\partial u_z}{\partial y}\Delta y \qquad (3.27(a))$$

We now represent the above six lengths in terms of nodal differences at a given time *t*, in the same form utilized in our code. Note that in our code, as represented by Fig. 3.10(b), we have two nested loops, one for time and one for space. All of our subsequent variable notations, which include *i,j* represent parameters that are stored for every grid-point location in space. The variables without *i,j* are temporary variables whose values are replaced with every new loop iteration. Specifically

$$x_{\text{hori}} = x_{i+1,j} - x_{i,j} \qquad (3.22(b))$$

$$y_{\text{hori}} = y_{i+1,j} - y_{i,j} \qquad (3.23(b))$$

$$x_{\text{vert}} = x_{i,j+1} - x_{i,j} \qquad (3.24(b))$$

$$y_{\text{vert}} = y_{i,j+1} - y_{i,j} \qquad (3.25(b))$$

$$z_{\text{hori}} = z_{i+1,j} - z_{i,j} \qquad (3.26(b))$$

$$z_{vert} = z_{i,j+1} - z_{i,j} \qquad (3.27(b))$$

Using the above parameters, we also define the physical length of a hori or vert yarn element between two nodes by the following

$$r_{\text{hori}} = \sqrt{x_{\text{hori}}^2 + y_{\text{hori}}^2 + z_{\text{hori}}^2} \quad (3.28(a))$$

$$r_{\text{vert}} = \sqrt{x_{\text{vert}}^2 + y_{\text{vert}}^2 + z_{\text{vert}}^2} \quad (3.28(b))$$

For stability purposes, we also use r_{hori} and r_{vert} to prevent compressive forces in the in-plane directions, but ensure that the nodal positions are not affected. From Fig. 3.13, we note that *Y* is the yarn length between two nodes in a crimped state, and *D* is *dl*, the original mesh size in our simulations. Using the crimp length ratio A, we impose the following conditions

$$r_{\text{hori}} = dl \cdot \mathrm{A} \qquad (\text{if } r_{\text{hori}} < dl \cdot \mathrm{A}) \quad (3.29(a))$$

$$r_{\text{vert}} = dl \cdot \mathrm{A} \qquad (\text{if } r_{\text{vert}} < dl \cdot \mathrm{A}) \quad (3.29(b))$$

We next define a strain-related parameter with units of [1/length]:

$$ir_{\text{hori}} = \frac{1}{dl \cdot \mathrm{A}} - \frac{1}{r_{\text{hori}}} \quad (3.30(a))$$

$$ir_{\text{vert}} = \frac{1}{dl \cdot \mathrm{A}} - \frac{1}{r_{\text{vert}}}\,. \quad (3.30(b))$$

To compute strains in hori and vert yarns in our code, we use the parameters above to get the following relations

$$\varepsilon_{\text{hori}} = (dl \cdot \mathrm{A}) \cdot ir_{\text{hori}} \quad (3.31(a))$$

$$\varepsilon_{\text{vert}} = (dl \cdot \mathrm{A}) \cdot ir_{\text{vert}}\,. \quad (3.31(b))$$

These strains can also be written in the form:

$$\begin{aligned}\varepsilon_{\text{hori}} &= (dl \cdot \mathrm{A}) \cdot ir_{\text{hori}} \\ &= (dl \cdot \mathrm{A}) \cdot \left[\frac{1}{(dl \cdot \mathrm{A})} - \frac{1}{r_{\text{hori}}} \right] \\ &= 1 - \frac{dl \cdot \mathrm{A}}{r_{\text{hori}}} \\ &= \frac{r_{\text{hori}} - dl \cdot \mathrm{A}}{r_{\text{hori}}} \end{aligned} \tag{3.32}$$

In addition to calculating the strains between two nodes, we also calculate the relative velocities between two nodes by:

$$\Delta vx_{\text{hori}} = vx_{i+1,j} - vx_{i,j} \tag{3.33(a)}$$

$$\Delta vy_{\text{hori}} = vy_{i+1,j} - vy_{i,j} \tag{3.33(b)}$$

$$\Delta vx_{\text{vert}} = vx_{i,j+1} - vx_{i,j} \tag{3.33(c)}$$

$$\Delta vy_{\text{vert}} = vy_{i,j+1} - vy_{i,j} \tag{3.33(d)}$$

$$\Delta vz_{\text{hori}} = vz_{i+1,j} - vz_{i,j} \tag{3.33(e)}$$

$$\Delta vz_{\text{vert}} = vz_{i,j+1} - vz_{i,j} \tag{3.33(f)}$$

We note that with the exception of the strains, all the variables presented in this section are not stored in a vector or matrix. Upon reviewing the flow chart of the code from Section 3.2.1, we observe that these calculations are located within the nested time and space loops, are re-calculated per iteration, and not stored to save computation space.

Now we look at how positions and velocities are updated outside of that space loop (but still within the time loop) yet still for all *i,j* covering the fabric. We write Eq. (3.13) and Eq. (3.14) for the *x*-direction in the code as:

$$vx_{i,j}^{t} = vx_{i,j}^{t-\Delta t} + \frac{fx_{i,j}^{t}}{massx_{i,j}} \cdot dt \tag{3.34}$$

$$x_{i,j}^{t} = x_{i,j}^{t-\Delta t} + vx_{i,j}^{t} \cdot dt\,, \tag{3.35}$$

where the *y*- and *z*-directions position and velocity updates take the same form.

3.2.7 Force calculations

We summarize our process for determining forces at all nodes after impact by the following process:

(i) Compute individual element forces shown in Figs. 3.8(b) and 3.11(a)

(ii) Resolve all the element forces applied to each node with conditions based on the location of the node, i.e. if it's located on the boundary or not

(iii) Sum and redistribute *z*-forces for nodes in contact with the projectile

(iv) Apply slip damping for nodes in contact with projectile

Similar to the length definitions and notations, we have six individual element forces, where a name such as fx_{hori} represents the *x*-component of the force in the hori yarn. We model these element forces like a mass-spring-damper system, shown in Fig. 3.18 and described generically by the equation

$$m\ddot{x} + c\dot{x} + kx = 0\,, \tag{3.36}$$

where *m* is the mass, *c* is the damping coefficient, and *k* is the spring stiffness.

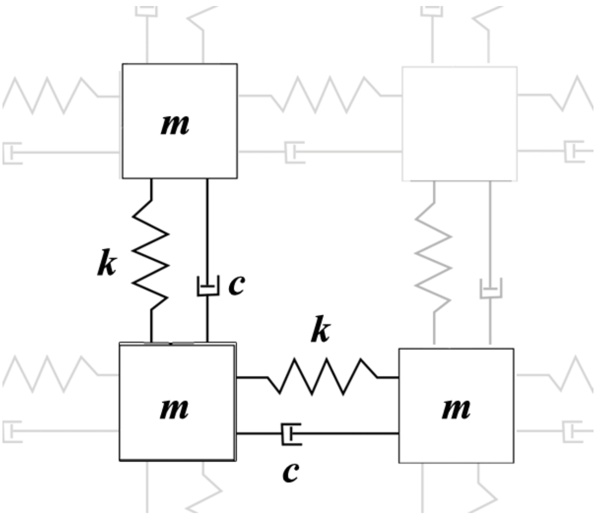

Figure 3.18. Mass-spring-damper system network used for modeling individual element tension forces in our simulations, which also include (but is not shown here) shear slip and rocking viscosity used for damping oscillations.

Our six element forces are:

$$fx_{\text{hori}} = E_x A_0 \cdot (ir_{\text{hori}} \cdot x_{\text{hori}} + \eta \cdot \Delta vx_{\text{hori}}) \tag{3.37(a)}$$

$$fy_{\text{hori}} = E_x A_0 \cdot (ir_{\text{hori}} \cdot y_{\text{hori}} + \eta \cdot \Delta vy_{\text{hori}}) \tag{3.37(b)}$$

$$fx_{\text{vert}} = E_y A_0 \cdot (ir_{\text{vert}} \cdot x_{\text{vert}} + \eta \cdot \Delta vx_{\text{vert}}) \tag{3.37(c)}$$

$$fy_{\text{vert}} = E_y A_0 \cdot (ir_{\text{vert}} \cdot y_{\text{vert}} + \eta \cdot \Delta vy_{\text{vert}}) \tag{3.37(d)}$$

$$fz_{\text{hori}} = E_x A_0 \cdot (ir_{\text{hori}} \cdot z_{\text{hori}} + \eta \cdot \Delta vz_{\text{hori}}) \tag{3.37(e)}$$

$$fz_{\text{vert}} = E_y A_0 \cdot (ir_{\text{vert}} \cdot z_{\text{vert}} + \eta \cdot \Delta vz_{\text{vert}}) \tag{3.37(f)}$$

where $E_x A_0 \cdot ir_{\text{hori}} \cdot x_{\text{hori}}$ corresponds to the kx term from Eq. (3.36) and $E_x A_0 \cdot \eta \cdot \Delta vx_{\text{hori}}$ corresponds to the $c\dot{x}$ term from Eq. (3.36). Since all the forces have units of N, and $E_x A_0$ also has units of N, $\eta \cdot \Delta vx_{\text{hori}}$ must be dimensionless, making η have units of time/length, or seconds/meters.

We then resolve all the element forces per direction using the equations above at each *i,j* node location. For most nodes, which are not located on the projectile or fabric boundaries, we use the following summation scheme (shown here for the *x*-direction and within loops that update over time):

$$fx_{i,j}^{t} = fx_{i,j}^{t-\Delta t} + fx_{\text{hori}} + fx_{\text{vert}} \tag{3.38(a)}$$

$$fx_{i+1,j}^{t} = fx_{i+1,j}^{t-\Delta t} - fx_{\text{hori}} \tag{3.38(b)}$$

$$fx_{i,j+1}^{t} = fx_{i,j+1}^{t+\Delta t} - fx_{\text{vert}} \tag{3.38(c)}$$

Each *i+1* and *j+1* node includes a subtraction of the same force added at the *i,j* node because every force applied at a node is equal in magnitude and opposite in sign to the same force applied to its direct neighboring node. For the *y*- and *z*-directions, we assign the same set of boundaries as Eq. (3.38).

Nodal force calculation at boundaries is discussed in the next section.

Next, we identify the nodes in contact with the projectile and loop through all of them, and in the process sum up the corresponding $fz_{i,j}$ forces into a single total value $fz_{\text{proj,gp,tot}}$. We divide this number by $n_{\text{proj,gp}}$ to obtain $fz_{\text{proj,gp}}$, the new, evenly distributed, *z*-force to be assigned per node (in contact with the projectile).

Within another loop, we assign $fz_{i,j}$ to be equal to $fz_{\text{proj,gp}}$ for all nodes in contact with the projectile. The physical reasoning behind this equal redistribution in our simulation is that since we have an RCC projectile with a flat nose, all nodes in contact with the projectile should move as one entity, as shown in Fig. 3.19. Therefore, the *z*-forces acting on those nodes are assumed to be the same for any given time.

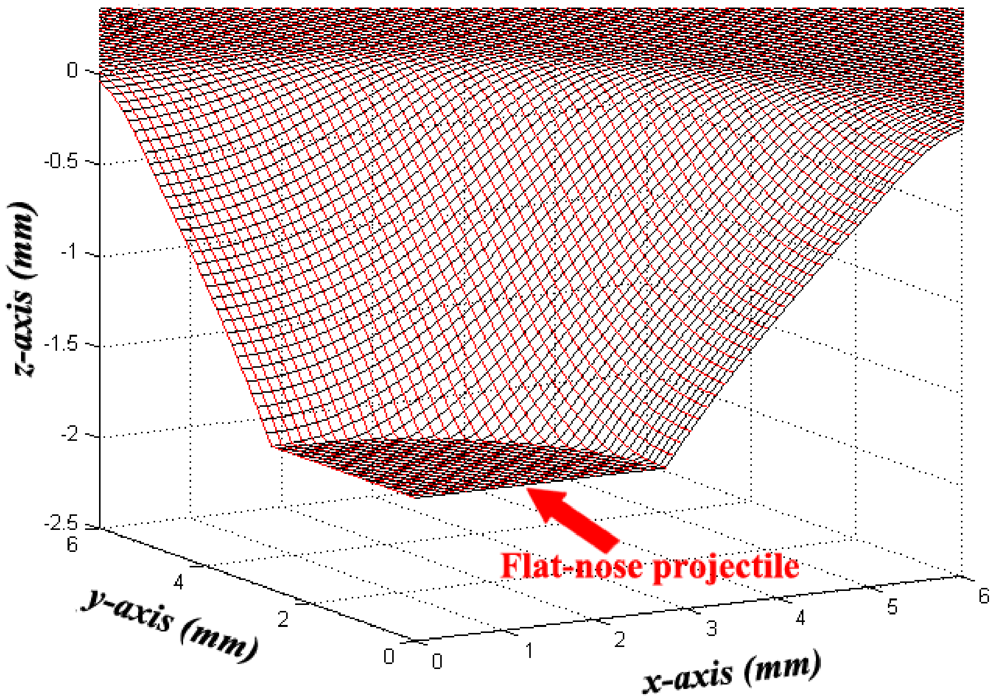

Figure 3.19. Fabric yarn positions at some arbitrary time t after impact but before failure. Black lines represent weft or "hori" yarns. Red lines represent warp or "vert" yarns.

Finally, for the in-plane x- and y-directions, we apply slip damping to the forces in the nodes (in contact with the projectile) through the computations (as part of an updating scheme):

$$fx_{i,j}^{t} = fx_{i,j}^{t-\Delta t} + \zeta \cdot \min(fz_{i,j}^{t}, 0) \cdot vx_{i,j}^{t} \tag{3.39(a)}$$

$$fy_{i,j}^{t} = fy_{i,j}^{t-\Delta t} + \zeta \cdot \min(fz_{i,j}^{t}, 0) \cdot vy_{i,j}^{t} . \tag{3.39(b)}$$

Here, we are modeling frictional slip as proportional to the out-of-plane force $fz_{i,j}$ but still dependent on the in-plane velocity. The $\min(fz_{i,j}, 0)$ shows that only when $fz_{i,j}$ is negative should its value be used, since that means the z-force is a compressive force, which causes the projectile to be in contact with the fabric. When $fz_{i,j}$ is positive, there is no contact between projectile and fabric, and therefore no slip is to be considered, hence the 0 value. ζ is the slip viscosity factor, and is used as a damping term similar to η, and also has units of seconds/meters. We note that in cases where we assume no slip to occur underneath the projectile, the value of ζ plays no noticeable role in simulation results. More discussion of this topic can be found in Section 3.2.9.

3.2.8 Boundary conditions

As mentioned in Section 3.2, we always set our fabric size to a large-enough value so that we do not need to consider interference from wave reflections at the fabric boundaries. This is also the assumption made in all of our previous analytical models, which is unlike many experimental setups where a rectangular layer of ballistic fabric is clamped on two or four sides prior to being shot at by a projectile.

Since we only use one quarter of the actual-sized fabric to save computational space, but want the calculated results to represent the entire piece of fabric, we impose boundary conditions to describe and account for the *x*- and *y*-axial symmetries. Fig. 3.20 shows the three types of boundary conditions present in our code. Non-boundary nodal force calculations were presented in Eq. (3.38) from Section 3.2.7.

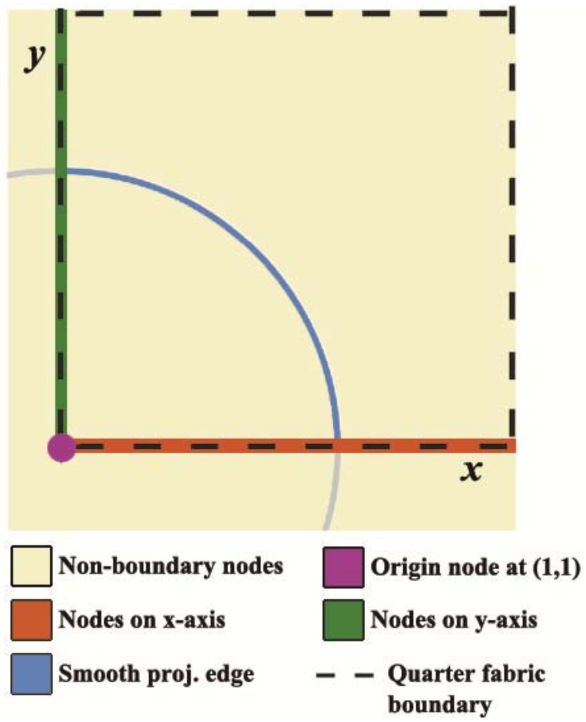

Figure 3.20. Location of critical boundaries in our simulation.

The 3 types of boundary conditions in Fig. 3.18 are:

(i) Nodes on x-axis

(ii) Nodes on y-axis

(iii) Origin node.

For (i), we impose the following conditions for nodal forces in the x-direction:

$$fx_{i,j}^{t} = fx_{i,j}^{t-\Delta t} + fx_{\text{hori}} + 2 \cdot fx_{\text{vert}} \tag{3.40(a)}$$

$$fx_{i+1,j}^{t} = fx_{i+1,j}^{t-\Delta t} - fx_{\text{hori}} \tag{3.40(b)}$$

$$fx_{i,j+1}^{t} = fx_{i,j+1}^{t-\Delta t} - fx_{\text{vert}} \tag{3.40(c)}$$

We observe that compared with Eq. (3.38(a)) from Section 3.2.7, Eq. (3.40(a)) multiplies fx_{vert} by a factor of two. This is because for nodes located on the x-axis, the

x-component of the vert yarn's force should be included twice to account for the axial symmetry.

For (i), we impose the following conditions for nodal forces in the y-direction:

$$fy_{i,j}^{t} = fy_{i,j}^{t-\Delta t} + fy_{\mathrm{hori}} \qquad (3.40(d))$$

$$fy_{i+1,j}^{t} = fy_{i+1,j}^{t-\Delta t} - fy_{\mathrm{hori}} \qquad (3.40(e))$$

$$fy_{i,j+1}^{t} = fy_{i,j+1}^{t-\Delta t} - fy_{\mathrm{vert}} \qquad (3.40(f))$$

We observe that for Eq. (3.40(d)), there are no y-component of vert forces present for nodes located on the x-axis.

Finally for (i), we impose the following conditions for nodal forces in the z-direction:

$$fz_{i,j}^{t} = fz_{i,j}^{t-\Delta t} + fz_{\mathrm{hori}} + 2\cdot fz_{\mathrm{vert}} \qquad (3.40(g))$$

$$fz_{i+1,j}^{t} = fz_{i+1,j}^{t-\Delta t} - fz_{\mathrm{hori}} \qquad (3.40(h))$$

$$fz_{i,j+1}^{t} = fz_{i,j+1}^{t-\Delta t} - fz_{\mathrm{vert}} \qquad (3.40(i))$$

Similar to the nodal forces in the x-direction, for Eq. (3.40(g)) we have fz_{vert} multiplied by a factor of two to reflect axial symmetry along the x-axis.

Condition (ii) is written similar to condition (i), except to reflect symmetry about the y-axis.

For the origin located at (1,1), we impose conditions which are significantly different from the DSM version of the code. Previously, all in-plane x- and y-direction forces were set to zero and only z-forces were nonzero. For our more general version but with no fabric slip underneath the projectile, such conditions were not problematic, since there was no motion in-plane for those nodes. However, for cases where slip occurred between projectile and fabric, such conditions created zero strain at a single node point amidst nonzero strains all around it, thus causing a non-physical singularity at the origin in the strain plots.

We therefore impose a set of different boundary conditions for (iii), with the *x*-direction nodal forces being

$$fx_{i,j}^{t} = fx_{i,j}^{t-\Delta t} + 2 \cdot fx_{\text{vert}} \tag{3.41(a)}$$

$$fx_{i+1,j}^{t} = fx_{i+1,j}^{t-\Delta t} - fx_{\text{hori}}, \tag{3.41(b)}$$

and the y-direction nodal forces being

$$fy_{i,j}^{t} = fy_{i,j}^{t-\Delta t} + 2 \cdot fy_{\text{hori}} \tag{3.41(c)}$$

$$fy_{i,j+1}^{t} = fy_{i,j+1}^{t-\Delta t} - fy_{\text{vert}}. \tag{3.41(d)}$$

We note that, like the equations listed above for symmetry about the *x*- and *y*-axes, at the origin, when we consider *x*-axis symmetry, we multiply by a factor of two for the vert yarn force, and vice versa for *y*-axis symmetry. We also purposely do not define *z*-direction nodal forces here, thus allowing previously defined *z*-conditions to apply themselves depending on other conditions such as crimp and/or slip.

For each time step iteration, we impose a separate set of conditions for the two outer edges of the fabric that do not include the *x*- or *y*-axes. To make sure these boundaries are kept in their original positions, we define the following for nodes there:

$$fx_{i,j}^{t} = fy_{i,j}^{t} = fz_{i,j}^{t} = 0. \tag{3.42}$$

3.2.9 Slip underneath the projectile

For our laminar crimp model, we include in our studies of post-impact behavior the effects of slip vs. no slip underneath the projectile. While there is more than one way to impose a no-slip condition, we chose to implement this by setting the in-plane *x*- and *y*-direction nodal masses, which are in contact with the projectile, to an extremely large value *M*. This is done before looping through time increments:

$$massx_{i,j} = M \tag{3.43(a)}$$

$$massy_{i,j} = M \ , \tag{3.43(b)}$$

where *M* was given a relatively high value of 100, which is three to four orders of magnitude greater than regular nodal masses defined by m_{gp} and $m_{\mathrm{proj,gp}}$. With a large *M* in Eq. (3.13), the in-plane velocities are thus restricted for nodes in contact with the projectile.

At each time step iteration, we also restrict any changes in position for these nodes by resetting its in-plane positions to their original values prior to impact:

$$x_{i,j} = (i-1) \cdot dl \tag{3.44(a)}$$

$$y_{i,j} = (j-1) \cdot dl \, . \tag{3.44(b)}$$

We note that for slip cases, we omit Eqs. (3.43) and (3.44).

Although slip underneath the projectile is not considered in our analytical membrane model, we anticipate the following scenario, shown in Fig. 3.21.

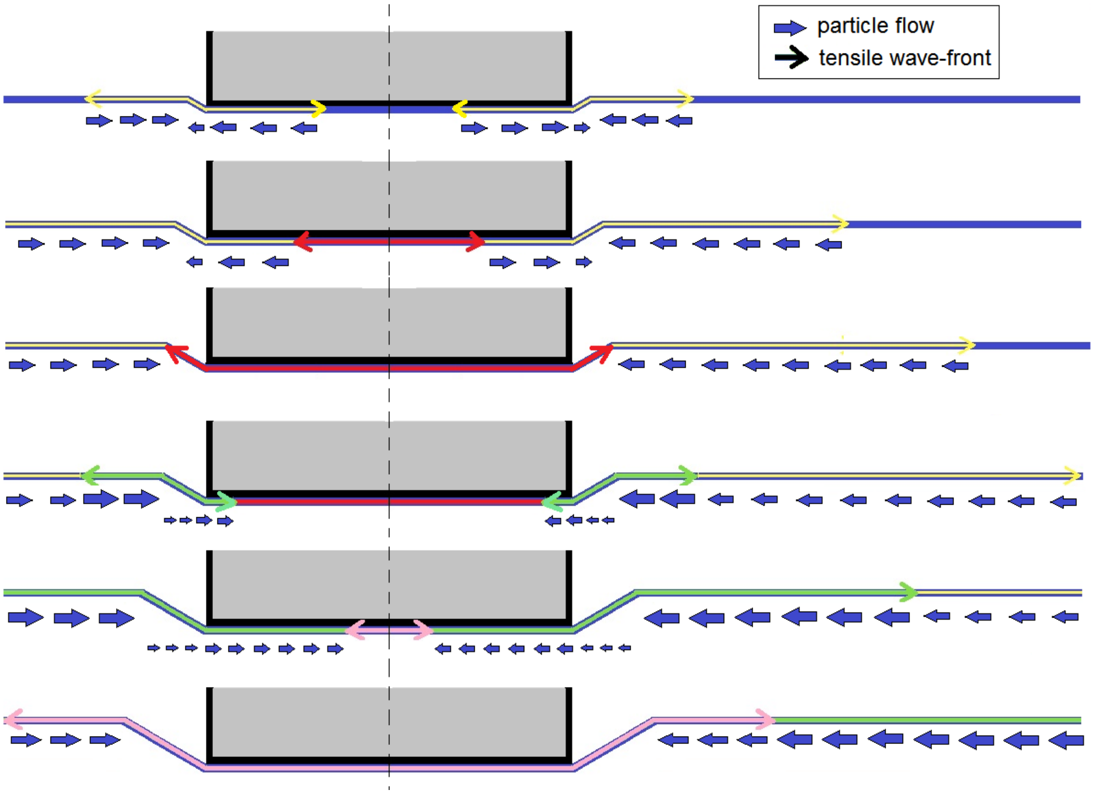

Figure 3.21. Sequential diagram showing wave propagation and particle flow post-impact for cases with slip allowed between projectile and fabric (looking at cross-sectional cut through the *x*-*z* plane).

The first diagram at the top in Fig. 3.21 shows two outward bound (towards fabric edge) as well as two inward bound (underneath the projectile) waves (all in yellow). At this initial stage, the outward bound waves bring particles inwards towards the projectile edge, while the inward bound waves bring particles outwards towards the projectile edge. Interestingly, we note that between the first and second diagrams, the inward bound waves (yellow) have collided at the projectile center, and are now also outward bound waves (red). This trend continues in the rest of the diagrams, although as more waves become outward bound, much more particle or material is drawn into the center, forming the cone wave.

For the no-slip case, because the in-plane velocities for the nodes in contact with the projectile are low, Eq. (3.39) determines that the term with ζ in it would also be small, which diminishes the influence of ζ. However, in the case of slip, ζ directly controls how much projectile-yarn friction is modeled in our system. The effects of ζ are presented in the results section of this chapter.

Despite our comparison of slip vs. no slip underneath the projectile, we observe that neither of the two cases' results would be completely representative of impact with real projectiles, which typically have conical shaped noses, as shown in Fig. 3.22. Due to its nose shape, there would most likely be no observable wave collision at the projectile center that could impact the post-impact fabric behavior. There would be slip present between projectile and yarns, but the magnitude of the contact surface area would be quite different from what our model assumes.

Figure 3.22. Comparison of various types of projectiles shapes.

3.2.10 Smoothing mechanisms

One key distinction between our model and the original DSM version is the addition of smoothing mechanisms in our code. After many trial-and-error runs, the two areas that needed smoothing were projectile edge *z*-positions and strains.

As discussed in Section 3.2.4, due to the nature of the square grid, the projectile edge in our simulation consists of a series of square or rectangular steps (Fig. 3.12), which is quite different from the perfectly circular edge of a real projectile. These protruding edges caused strain concentrations in those nodes in the original DSM code, which we discovered were results of the simulation's geometry, not actual physical behavior. Hence we seek to alleviate this effect by tapering down the projectile edge nodes, or giving them new *z*-positions that are smaller than their initially designated ones.

From Fig. 3.23, we first separate the projectile edge nodes into two types: regular or special. For the regular nodes, we use the *z*-position at the origin as the starting value, subtracting from it a percentage of the distance from the origin to the specific edge node by the following equation:

$$z_{i,j}^{t} = z_{1,1}^{t-\Delta t} - \frac{0.65 \cdot [0.9997 \cdot R_{\text{proj}} - \sqrt{(i-1)^2 + (j-1)^2} \cdot dl \cdot ((z_{k+2,1}^{t-\Delta t} - z_{k+1,1}^{t-\Delta t})]}{dl}. \tag{3.45}$$

For the special nodes, we use a similar scheme but with the node's own initial position $z_{i,j}$ as the starting value since these points may actually lie outside a perfectly circular edge, and therefore should not use the origin as its starting value:

$$z_{i,j}^{t} = z_{i,j}^{t-\Delta t} - \frac{0.07 \cdot [0.9997 \cdot R_{\text{proj}} - \sqrt{(i-1)^2 + (j-1)^2} \cdot dl \cdot ((z_{k+2,1}^{t-\Delta t} - z_{k+1,1}^{t-\Delta t})]}{dl} . \tag{3.46}$$

The constants used in Eqs. (3.45) and (3.46) were chosen through trial and error, and slight adjustments can be made to the values to obtain similarly acceptable results, which were based on scaling back strain values around the projectile edge that were over 1.5 times that of the average strain value in that region.

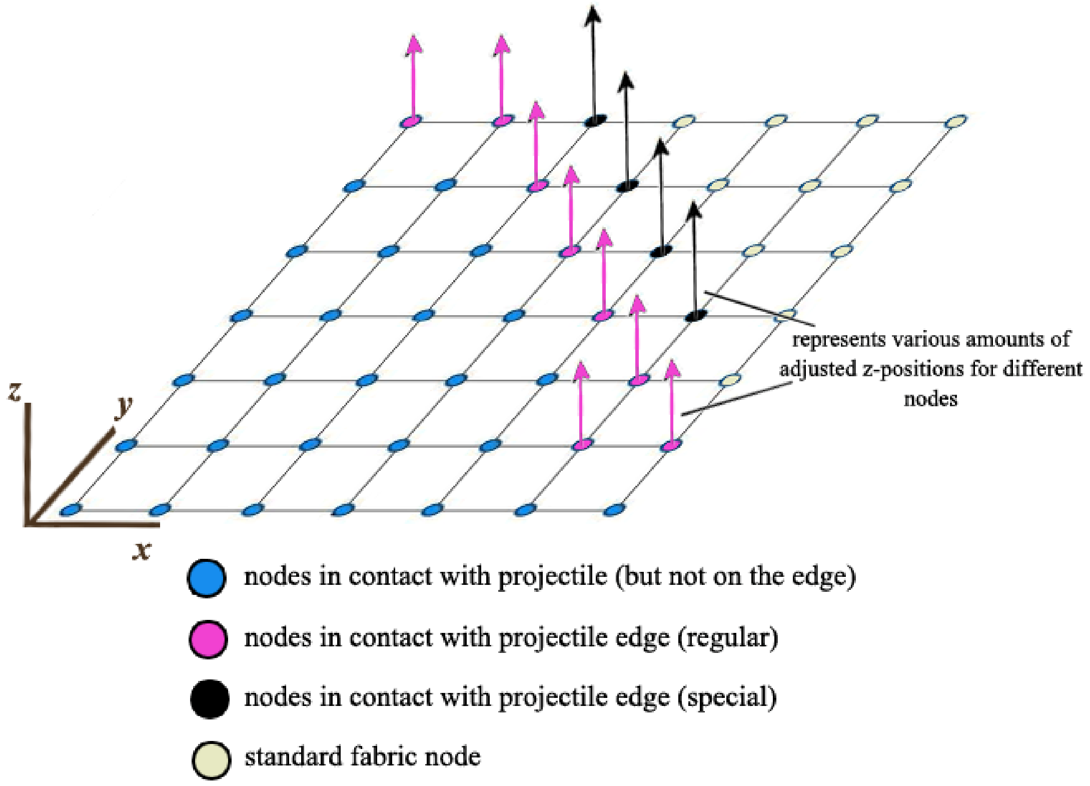

Figure 3.23. Tapering up of projectile edge nodes. Note that node locations shown in the figure do not necessarily represent actual node locations. For exact node locations, see Fig. 3.12.

We next discuss the smoothing of strains, which is necessary due to the network-of-discrete-masses nature of our model. In reality the yarns are continuous entities with mass relatively evenly distributed along their lengths. With our model, space and time are both looped through in finite increments, and one extremely high value at a certain node may render the program unstable. Even if it doesn't, such occurrences are most often products of the simulation set-up and not of the physical impact behavior. Hence in addition to the standard methods of computing strains from Eq. (3.31), we smooth, or recalculate the strains at each node to be a combination of those of its 12 neighbors.

First we revisit the values $k_1 - k_4$ described in Section 3.2.4, which are fractions of k and all smaller than k. Their locations relative to k on the grid are shown on Fig. 3.24 for the x-direction. By symmetry, the same values apply in the y-direction.

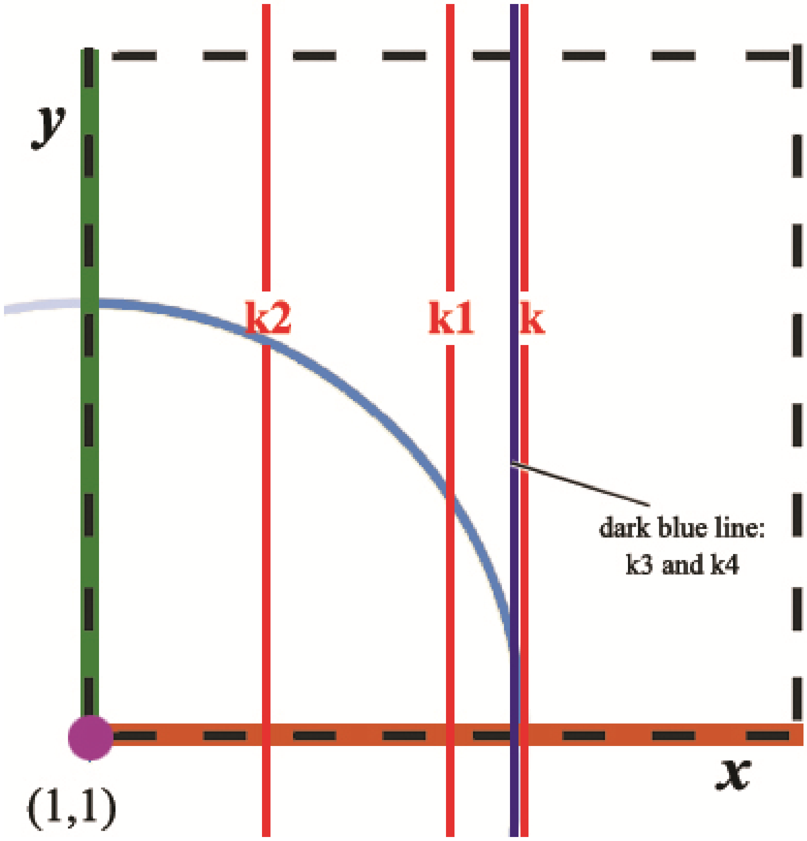

Figure 3.24. Locations of $k_1 - k_4$ in relation to k, shown in the x-direction.

Next we consider patches of fabric material whose *i,j* coordinates are defined by $k_1 - k_4$ and the fabric boundary node number n_{upper}. As we loop through those patches, we smooth the strains using relationships such as the following (with nodes shown in Fig. 3.25(a)):

$$\begin{aligned}\varepsilon_{\text{hori}}(i,j) = [&\varepsilon_{\text{hori}}(i-1,j) + \varepsilon_{\text{hori}}(i-1,j+1) + \varepsilon_{\text{hori}}(i-1,j+2) \\ &+\varepsilon_{\text{hori}}(i-1,j+3) + \varepsilon_{\text{hori}}(i,j) + \varepsilon_{\text{hori}}(i,j+1) \\ &+\varepsilon_{\text{hori}}(i,j+2) + \varepsilon_{\text{hori}}(i,j+3) + \varepsilon_{\text{hori}}(i+1,j) \\ &+\varepsilon_{\text{hori}}(i+1,j+1) + \varepsilon_{\text{hori}}(i+1,j+2) + \varepsilon_{\text{hori}}(i+1,j+3)]/12\end{aligned} \tag{3.47}$$

We repeat strain smoothing calculations similar to Eq. (3.47) a total of six times, three times for hori yarn strains and three times for vert yarn strains, each over a different patch. Fig. 3.25 provides two examples showing the neighboring nodes which were used for this “averaging” process.

Hence we suppress the extremely high strain values resulting from singular-like protrusions occurring along the projectile edge (due to the square mesh) generated by the original DSM code, shown in Figs 3.2 and 3.3.

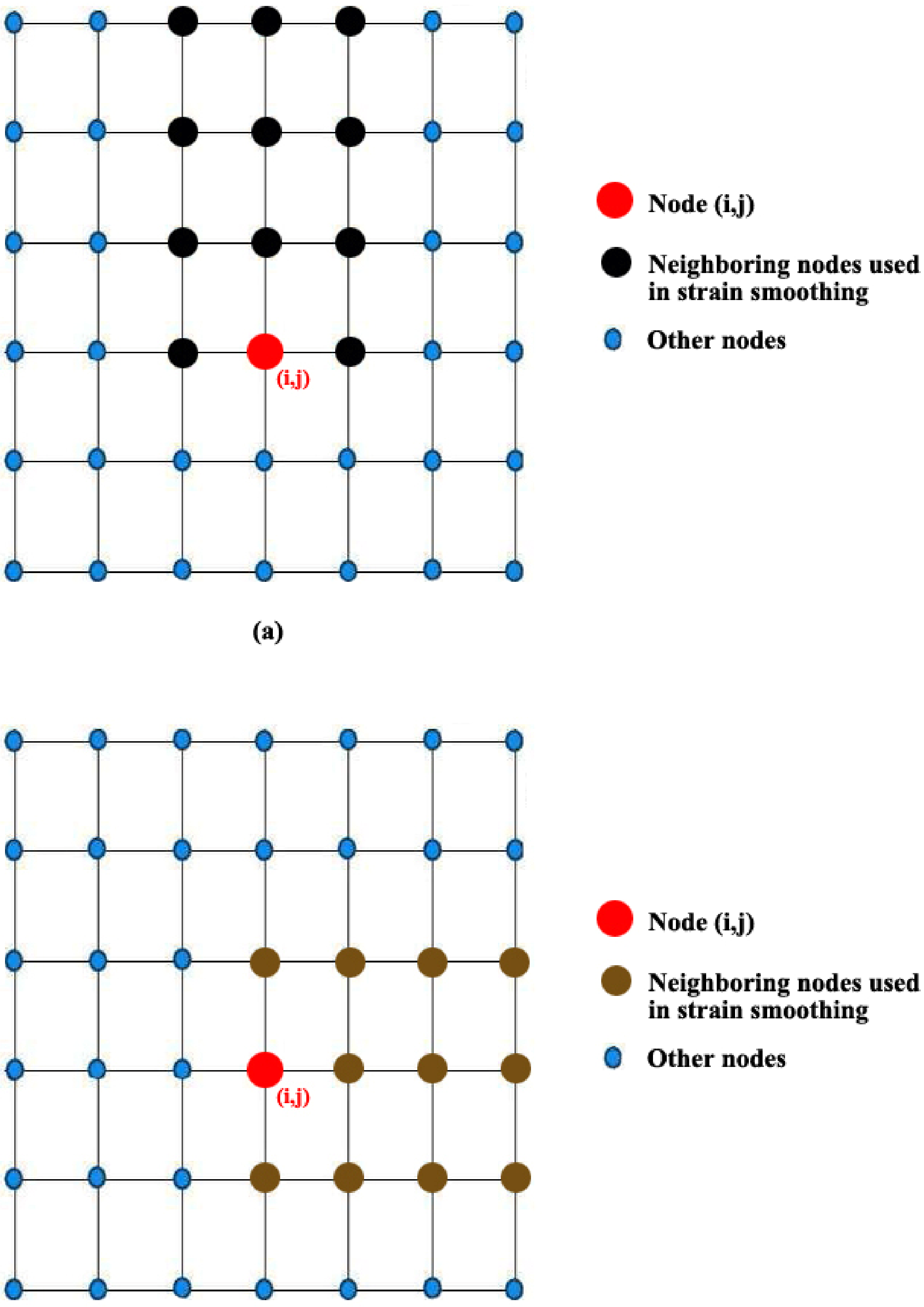

(a)

(b)

Figure 3.25. Two examples of the 12 nodes which are used in (a) $\varepsilon_{\text{hori}}$ and (b) $\varepsilon_{\text{vert}}$ averaging calculations.

3.3 Guide to reading graphs

We present a condensed tutorial for reading several types of graphs which are presented in the results section. The plots with only two axes are simple and straightforward to read, and are therefore not included for explanation in this section.

3.3.1 Horizontal strain around projectile edge over time

Since we know that the highest strain(s) in the fabric material post-impact occur in the vicinity of the projectile edge, we plot all the strains in this region over time to see how they develop. The result is a 3-D surface plot shown in Fig. 3.26 with axis labels. The color bar and third (strain) axis both show the magnitude of $\varepsilon_{\text{hori}}$; hence in graphs which derive from this original surface plot, no color key is provided as long as the third axis is visible and clearly labeled.

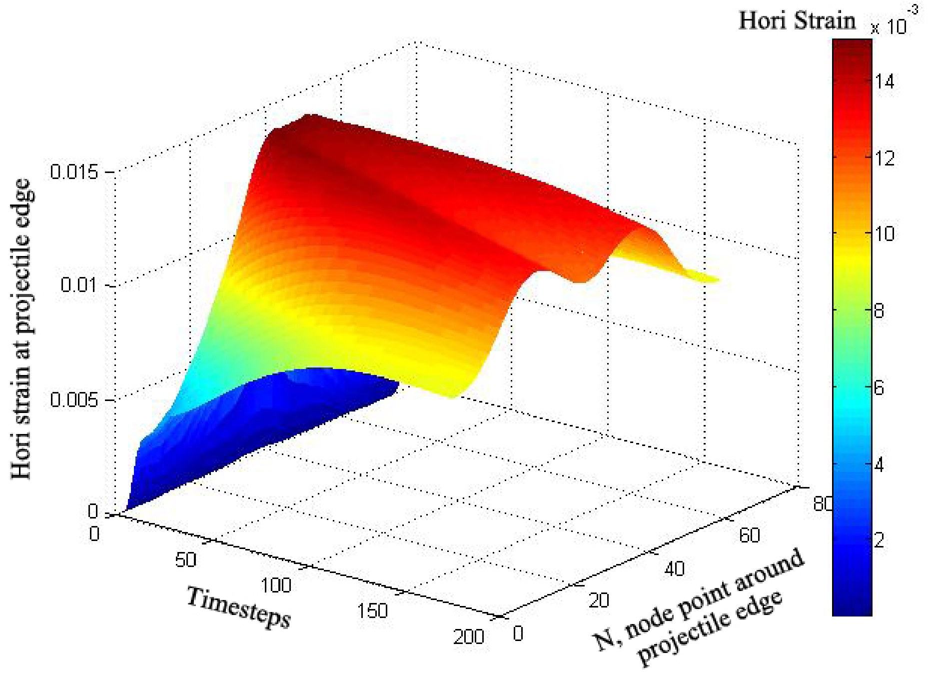

Figure 3.26. 3-D surface plot of hori strain around projectile edge over time.

Besides the 3-D version shown in Fig. 3.26, we can also take a 2-D cross-section of this plot, looking at either the Y-Z plane or the X-Z plane. Fig. 3.27 presents the two types of 2-D cross-sections made into plots.

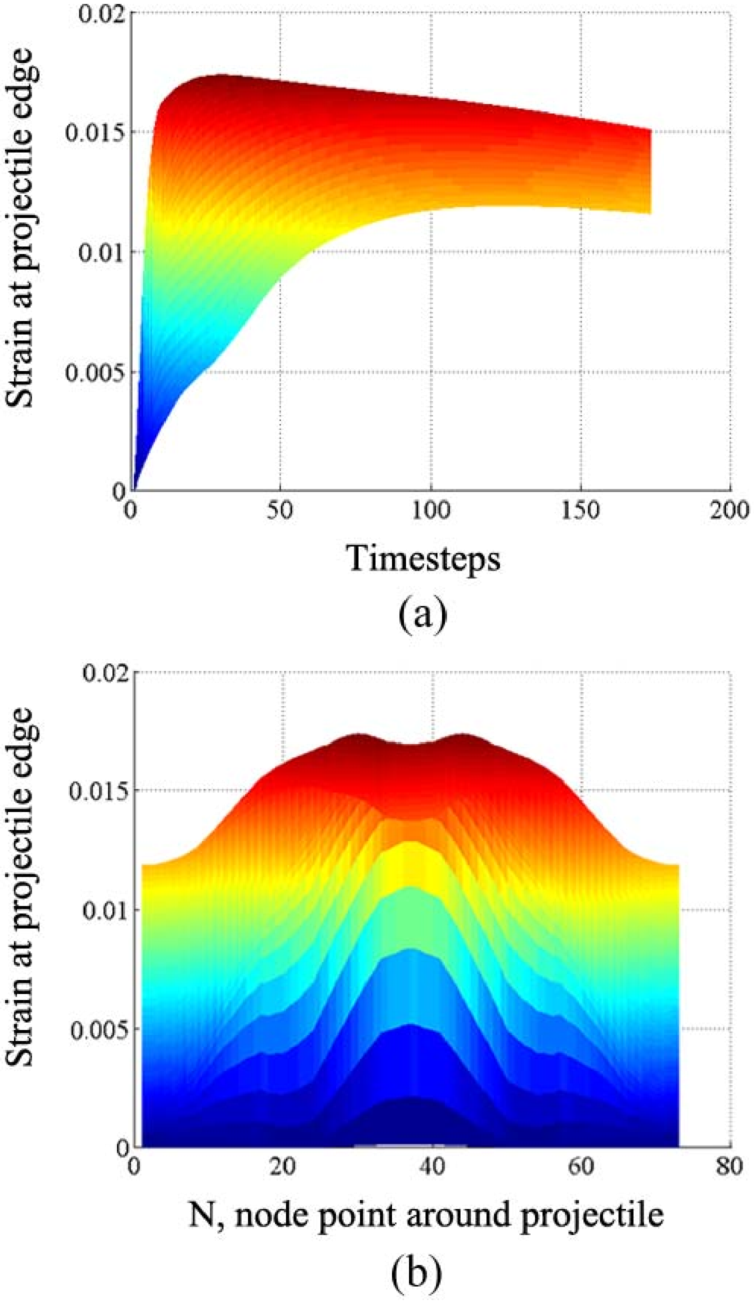

(a)

(b)

Figure 3.27. 2-D perspectives of 3-D surface strain plot shown in Fig. 3.26.

To understand what the variable N refers to, we look at Fig. 3.28. This number represents the number of nodes around the projectile edge, but starts counting at zero where $\theta = -90°$. As a result, $N = 38$ is located at the middle of Fig. 3.27(b), but represents $\theta = 0°$, or the node point which lies on the x-axis. N and θ are related, approximately, by the linear equation

$$\theta \approx 2.3684N - 90°. \tag{3.48}$$

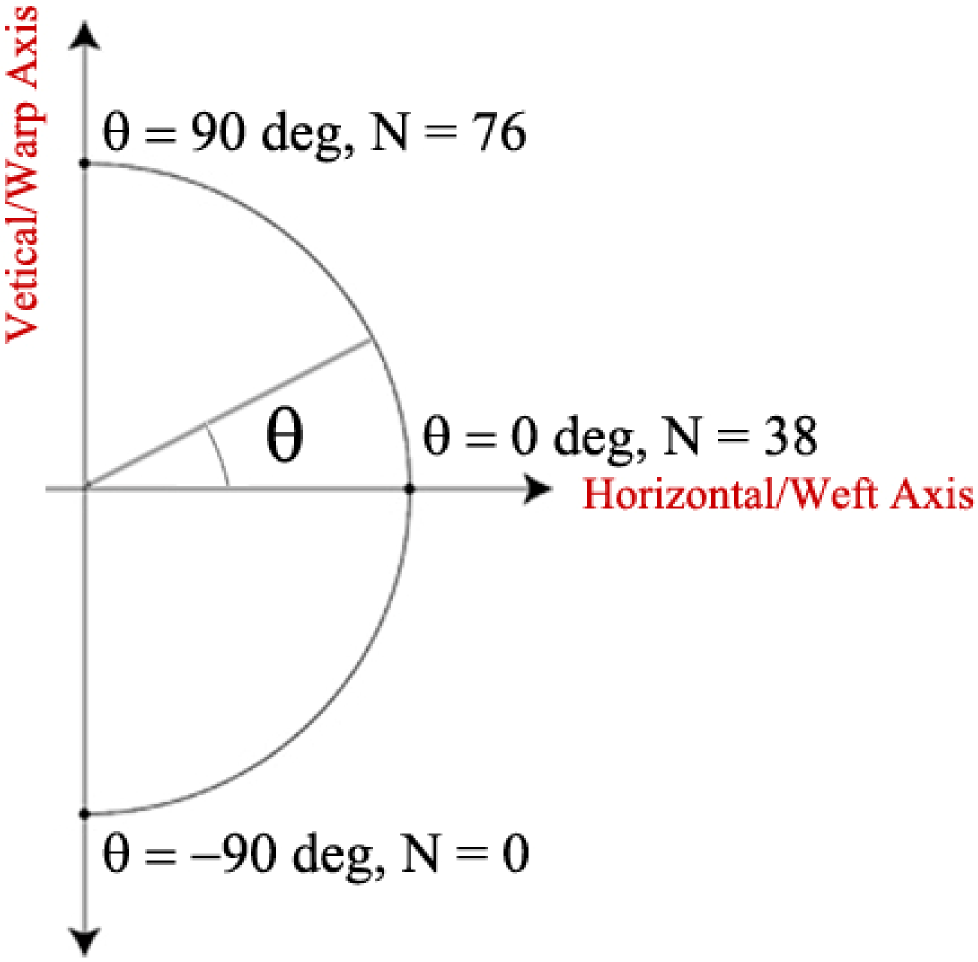

Figure 3.28. Schematic of half of actual circular projectile edge showing relationship between N and θ.

3.3.2 Horizontal slopes

Because the main focus of this dissertation is on crimp, it is crucial to be able to visualize the amount of crimp in the fabric material. Since our crimp is defined to be in the out-of-plane *z*-direction and has an up-down zigzag shape, we can calculate crimp in the *x*-direction by calculating horizontal slopes:

$$Slope_{\mathrm{hori}}(i,j) = [z(i+1,j) - z(i,j)]/dl \qquad (3.49)$$

Shortly after impact, the removal of yarn crimp in certain areas can be seen from a 3-D surface plot like the example shown in Fig. 3.29.

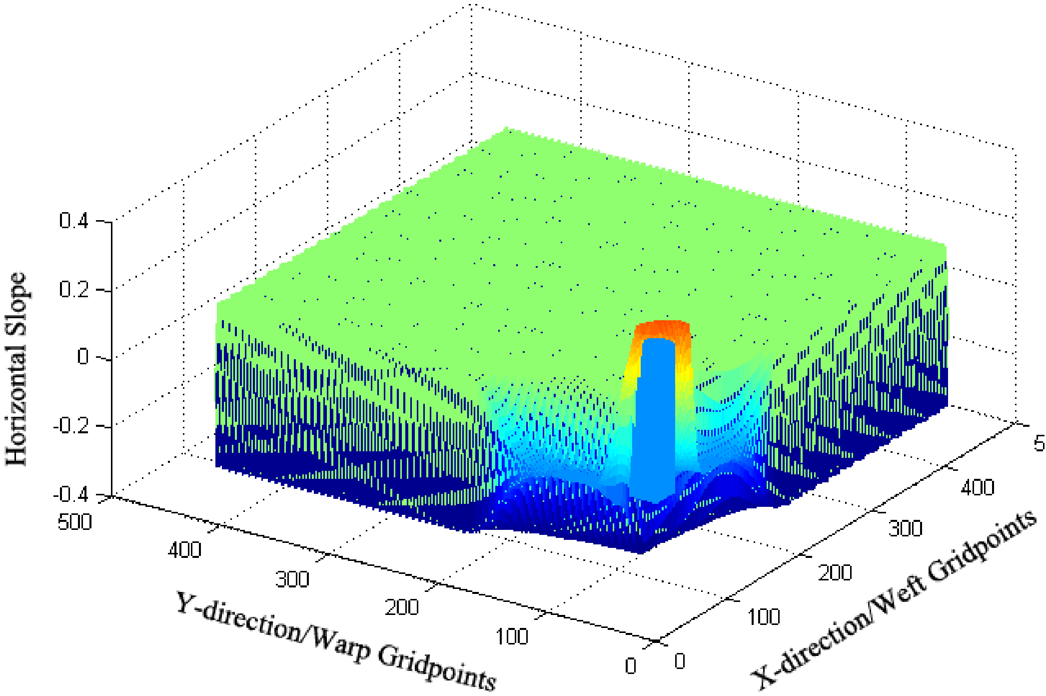

Figure 3.29. 3-D surface plot of horizontal slopes across the fabric material.

To be able to see what happens in both *x*- and *y*-directions clearly, we often prefer to look at the top-down view, or bird's eye-view of Fig. 3.29, shown in Fig. 3.30(a).

However, neither Fig. 3.29 nor Fig. 3.30(a) provide enough detail on specific, single yarn crimp behavior, and so we zoom in on a single yarn, anywhere within the fabric, to observe its de-crimping process, as shown in Fig. 3.30(b).

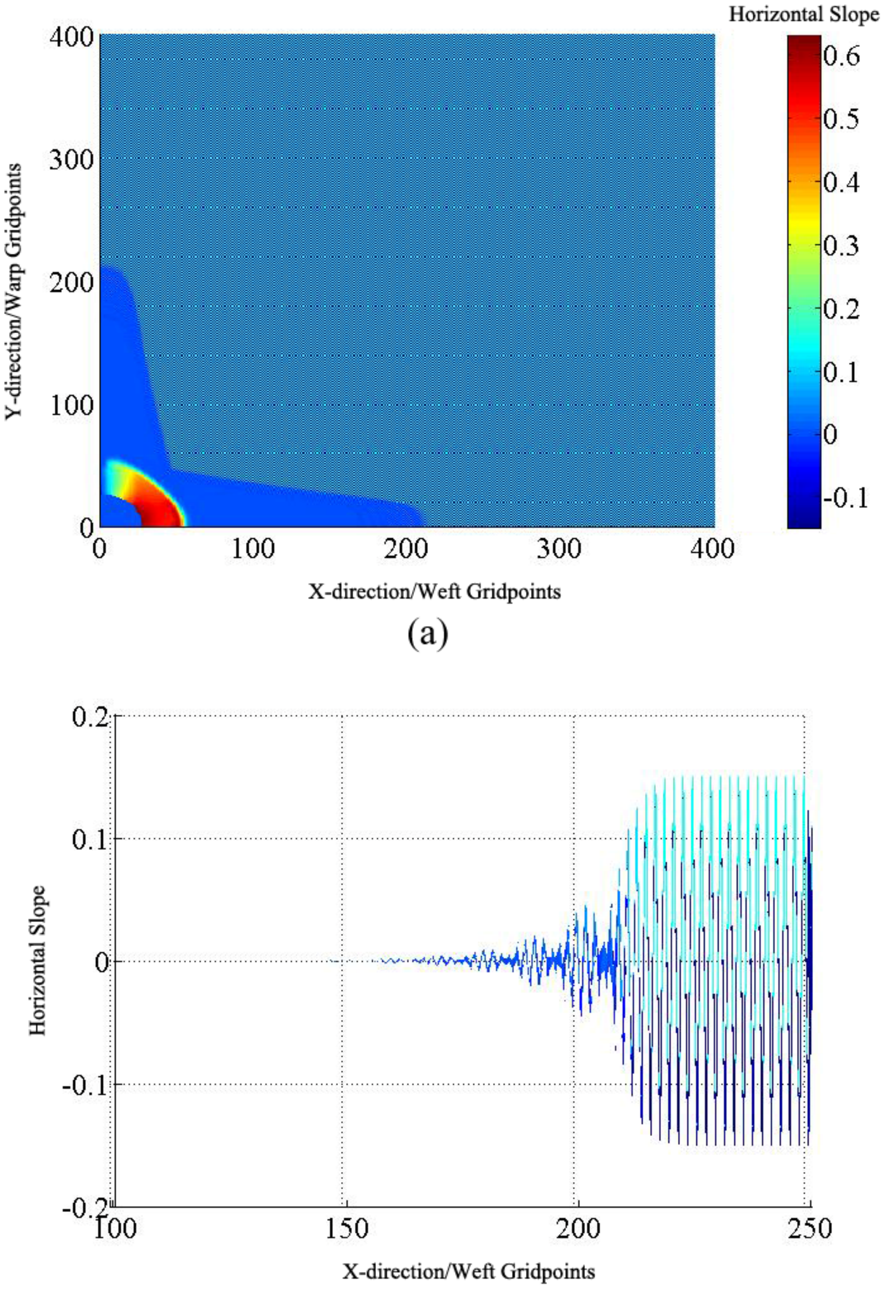

(a)

(b)

Figure 3.30. 2-D perspectives of 3-D surface slope plot shown in Fig. 3.29.

3.3.3 Cone wave features

We track the location of the cone wave front by plotting out-of-plane, or *z*-direction forces. At that cone wave front, material particles rapidly make the transition from moving in-plane to moving out-of-plane into the pyramid-shaped cone; hence in conjunction with this sudden change in material particle momentum, the *z*-direction forces show a sharp rise at the wave front, as shown in Fig. 3.31.

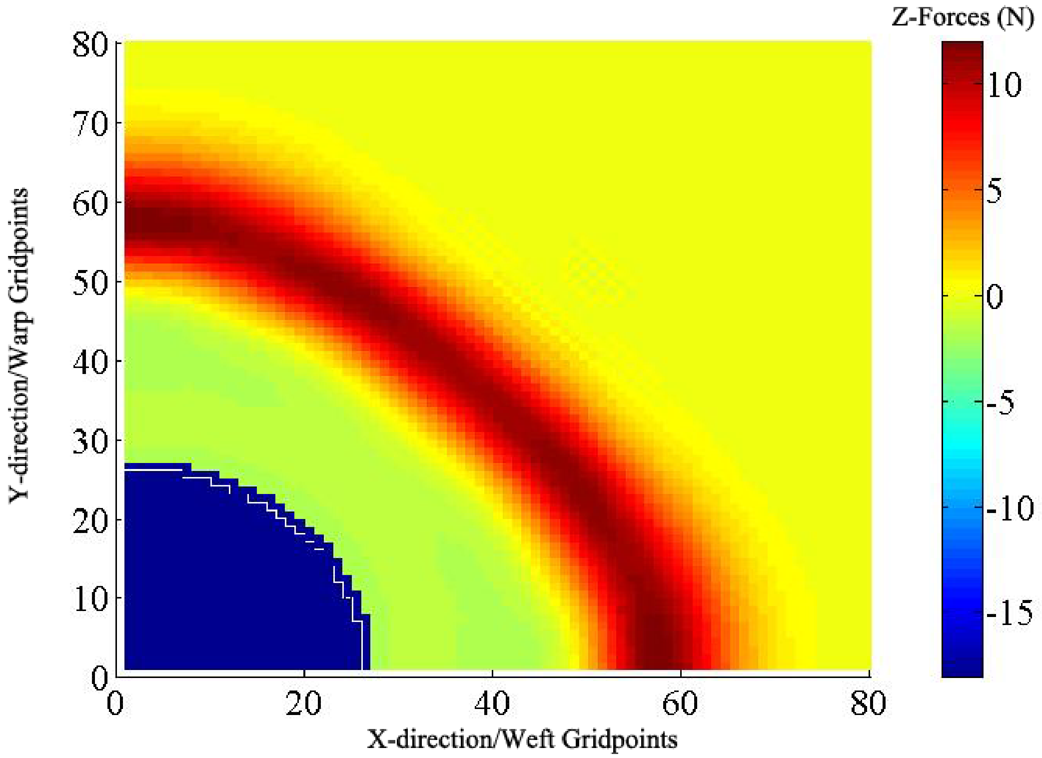

Figure 3.31. *Z*-direction, out-of-plane forces showing cone wave font post-impact.

Additionally, it is possible to see the evolution or growth of the cone wave over time as it slowly transforms from a circle like the shape of the projectile nose to a pyramid with rounded edges. We plot the out-of-plane position $z_{i,j}$ to observe this process in Figure 3.32.

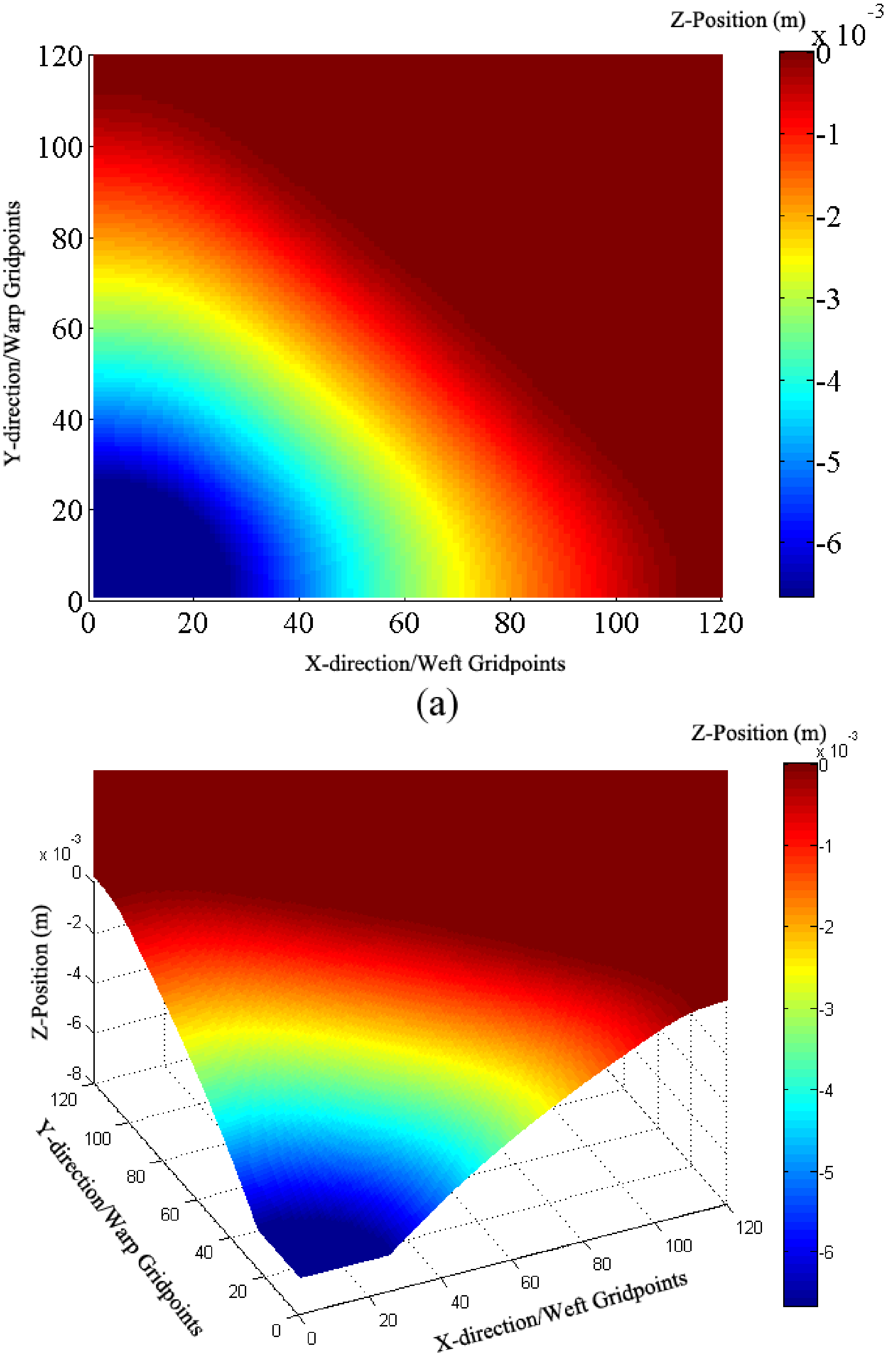

(a)

(b)

Figure 3.32. Fabric out-of-plane, *z*-positions with (a) top view and (b) 3-D-view.

3.3.4 In-plane velocities and displacements

From our mass-spring-damper modeling system, we know that forces are caused by changes in velocity and position. Since our rocking viscosity parameter, η, multiplies all the Δv terms in Eq. (3.37), and we can track its effects in the out-of-plane direction by Fig. 3.31, we now track its effects in-plane by plotting $vx(i,j)$ as a 3-D surface plot, shown in Fig. 3.33.

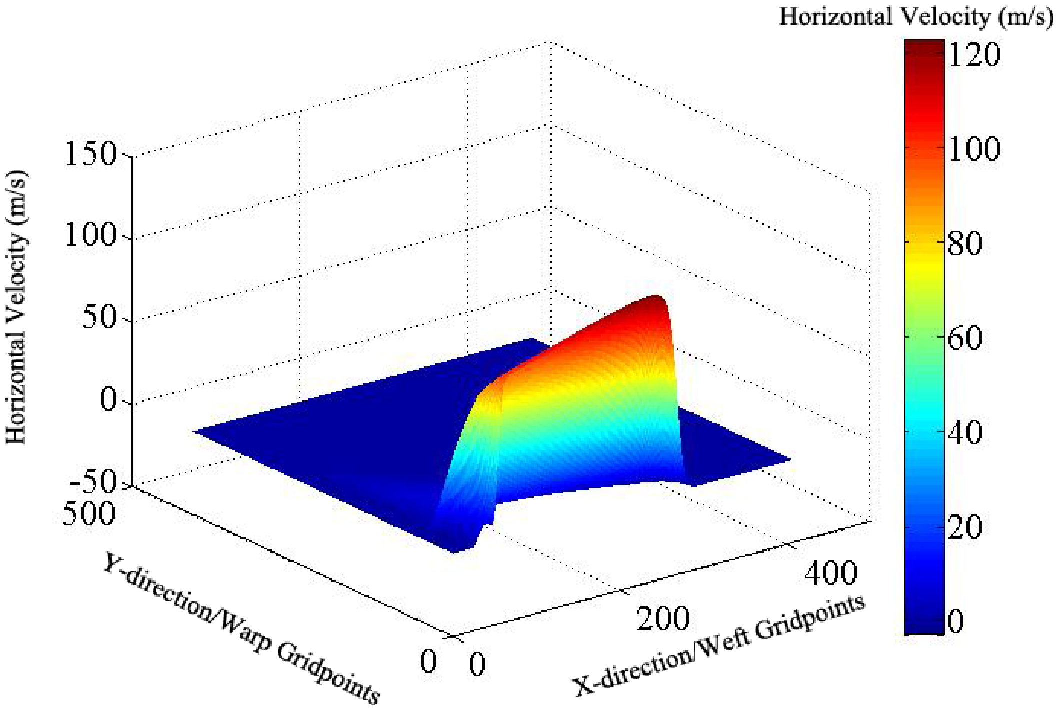

Figure 3.33. 3-D surface plot of in-plane x-velocities $vx(i,j)$ post-impact.

Fig. 3.33 can also be analyzed in more detail by looking at its various cross-sections, including views of the X-Y plane and Y-Z plane, as shown in Fig. 3.34. In-plane displacements can be calculated by subtracting initial positions from current ones and plotted in similar fashion as Figs. 3.33 and 3.34.

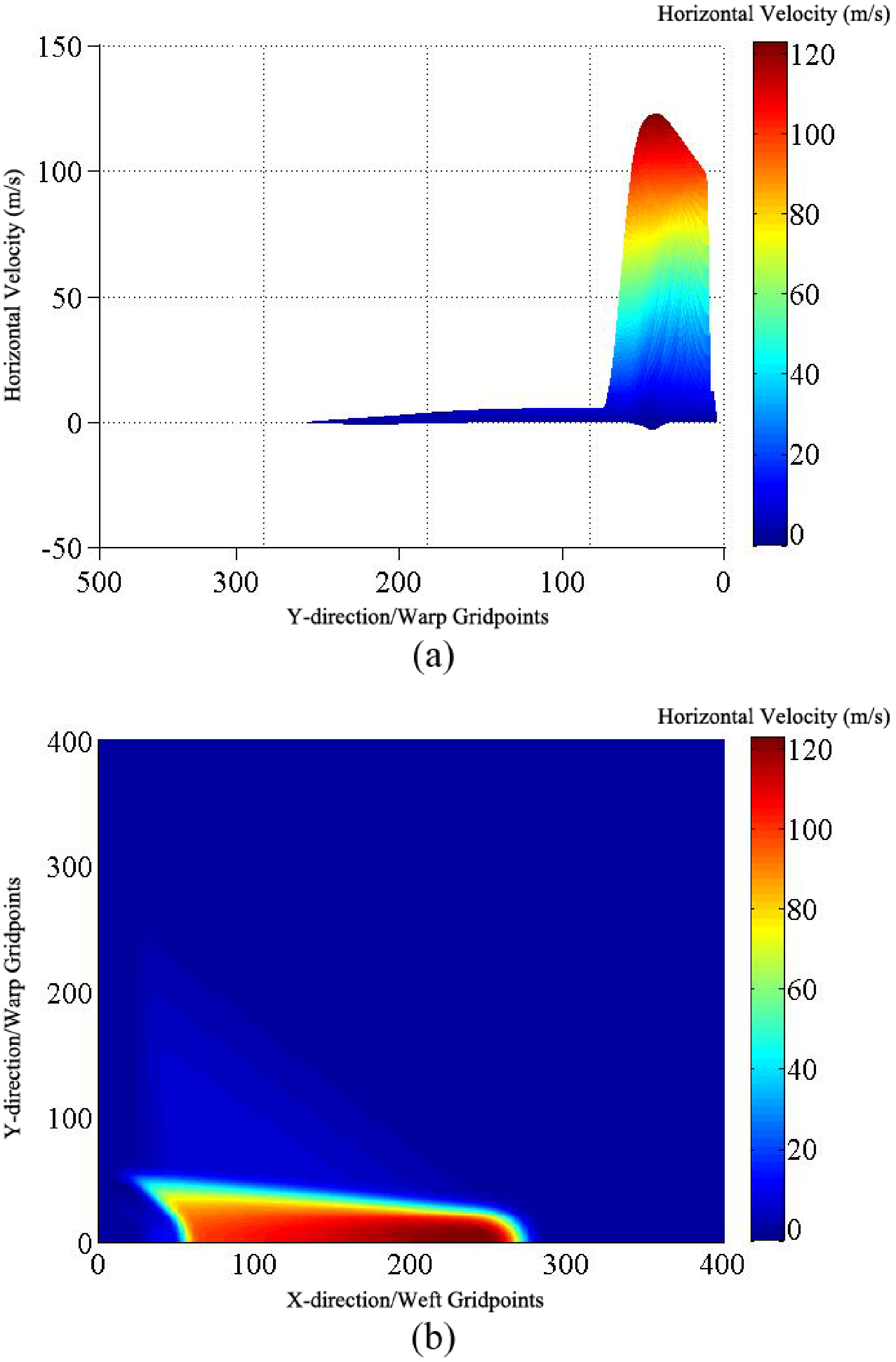

Figure 3.34. (a) Top view and (b) side view of 3-D plot of in-plane velocities shown in Figure 3.33.

3.3.5 In-plane tension waves

We observe the location of the tension wave front as well as its magnitude and shape by plotting tension strains in-plane. Plotted separately, $\varepsilon_{\text{hori}}(i,j)$'s 3-D surface profile is of the same type as Fig. 3.33. Occasionally we would like to see both hori and vert strains, and so we compute

$$StrainSqrt(i,j)=\sqrt{\varepsilon_{\text{hori}}(i,j)^2+\varepsilon_{\text{vert}}(i,j)^2}\,, \tag{3.50}$$

with the resulting graph in Fig. 3.35.

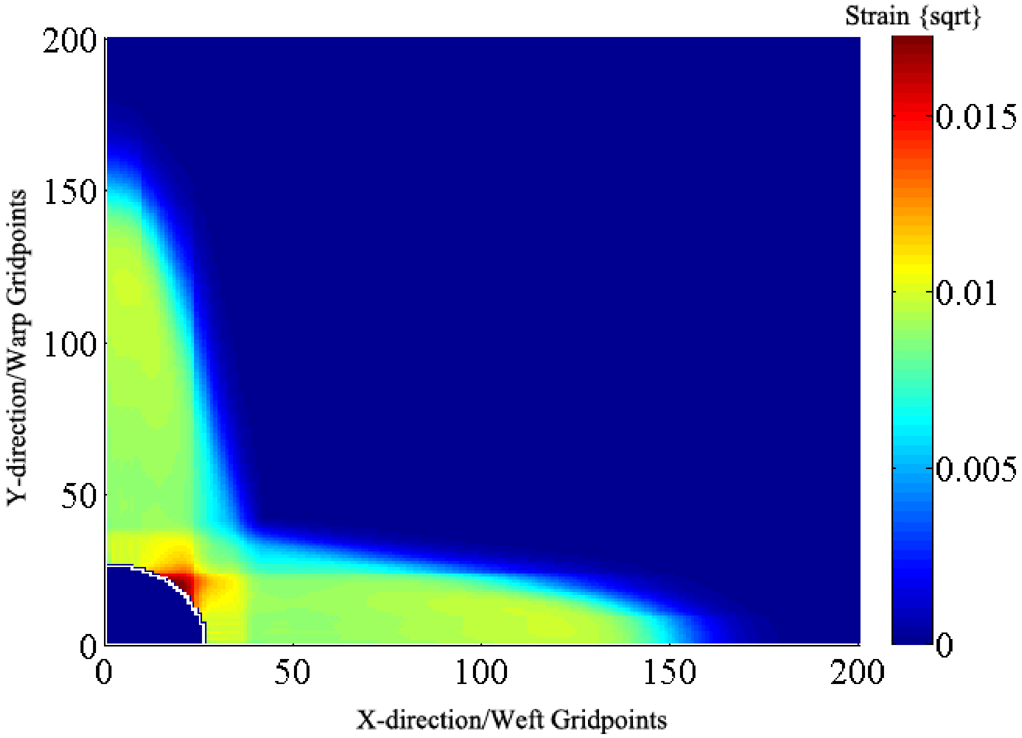

Figure 3.35. Top view of square root of hori and vert strains squared.

We note that the "star" shape of the tension waves propagating outwards in Fig. 3.35 resembles the schematic we use for understanding the "big picture" in Fig. 3.6.

3.4 Results and discussion

We present the results for our laminar crimp model in this section along with analysis and discussion. First, we discuss the influence of crimp on ballistic performance. Next, we discuss the roles of η and ζ and what, if any, of their effects depend on whether slip is allowed to occur underneath the projectile. Comparisons with analytical findings presented in Chapter 2 are interspersed throughout.

3.4.1 Key parameter and value combinations

The values we used in our simulations for η and ζ are listed in Table 3.6. We note that for each one of the cases there, all five crimp cases from Table 3.5 were run, as well as both projectile cases from Table 3.4. Selected plots of interest from the cases listed below are presented in the next section.

Table 3.6: Initial input values for parameters η and ζ in the laminar crimp model.

		Parameters	
Type	Case	η	ζ
No Slip	1a	1.60E-05	0.08
	1b	2.00E-05	0.08
	1c	2.00E-06	0.08
	1d	8.00E-06	0.08
	2a	2.00E-05	0.0004
	2b	8.00E-06	0.0004
Slip	3a	1.60E-05	0.08
	3b	2.00E-05	0.08
	3c	8.00E-06	0.08
	4a	2.00E-05	0.0004
	4b	8.00E-06	0.0004
	4c	8.00E-06	0.2

3.4.2 Effects of varying crimp on strain profiles

The most significant result of adding more crimp into a fabric system is the reduction in the maximum, average, and axis strains (strain in the most central yarn where $\theta = 0$) around the projectile edge regardless of projectile size, as shown in Figs. 3.36 and 3.37. Because maximum allowable yarn strain $\varepsilon_{\max}$ is used as the failure criterion when interpreting experimental data, any change in its value will also directly impact the V_{50}.

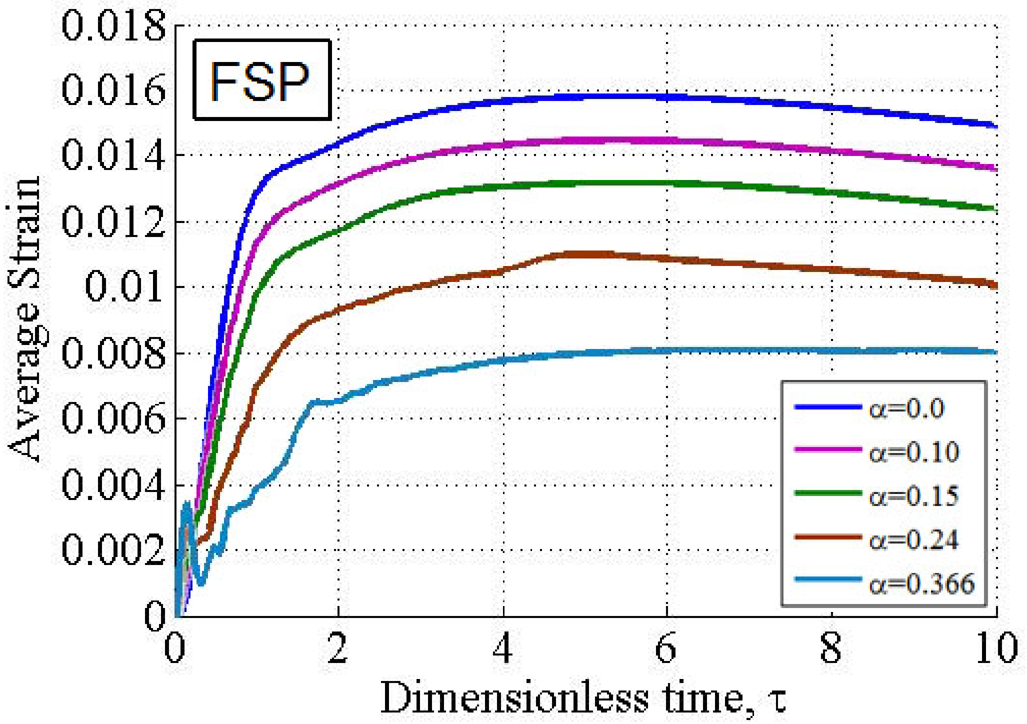

Figure 3.36. Comparison of average strain around the FSP for five cases of crimp using the laminar model. Results for Case 3c from Table 3.6 is shown here.

However, we also realize that failing one or two yarns may not necessarily result in failing the entire fabric and allowing the projectile to pass through. Therefore, we include average strain plots rather than maximum strain plots in our analysis of whether or not the fabric will fail. If the yarn strains around the projectile exceed the average strain, there is a much greater likelihood that failure will occur and the projectile will pass through.

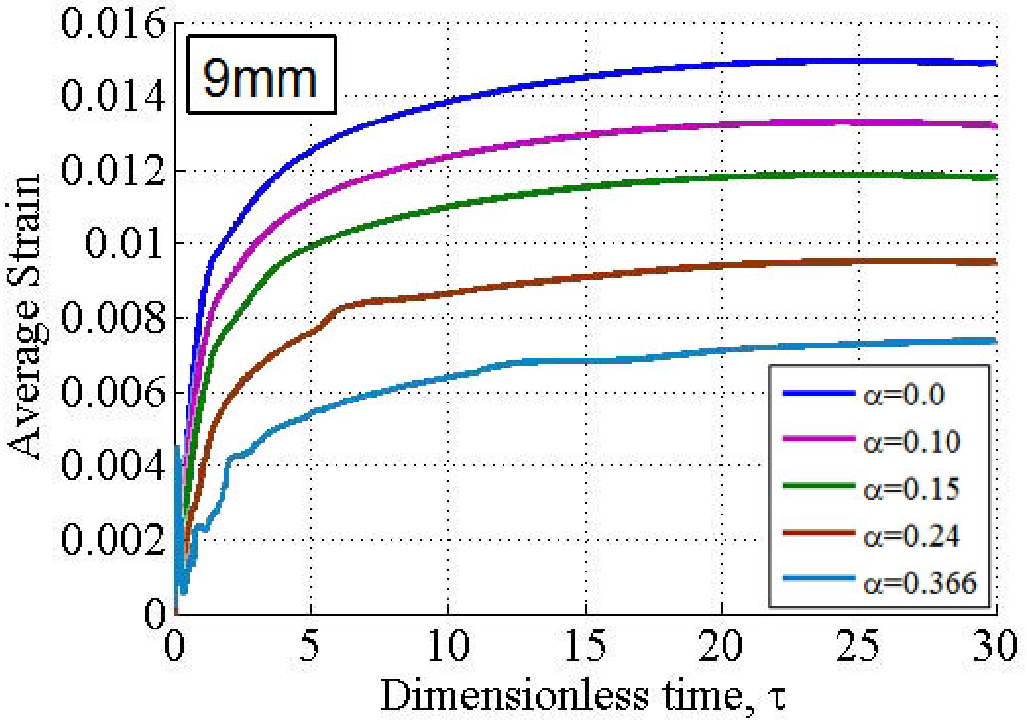

Figure 3.37. Comparison of average strain around the 9mm projectile for five cases of crimp using the laminar model. Results for Case 3c from Table 3.6 is shown here.

Figs. 3.36 and 3.37 clearly indicate that ε_{avg} varies inversely with the crimp factor, independent of fabric geometry and projectile dimensions. Hence, we predict that fabrics made with higher crimp in the yarns will have lower strains and higher V_{50} than fabrics with lesser and/or no crimp in their yarns (all other things being equal, particularly overall areal density). Increasing V_{50} is a top priority in the ballistic fabric making process, and crimp appears to play a beneficial role.

We note that results here agree with analytical prediction (2) from Section 2.6, where the 9mm average strain peaks at a much later time than the FSP average strain.

3.4.3 Effects of varying crimp on projectile velocity and displacement

From Fig. 3.38, we first observe that although having more crimp lowers overall strain in the yarns, its disadvantage is in causing slower deceleration of the projectile.

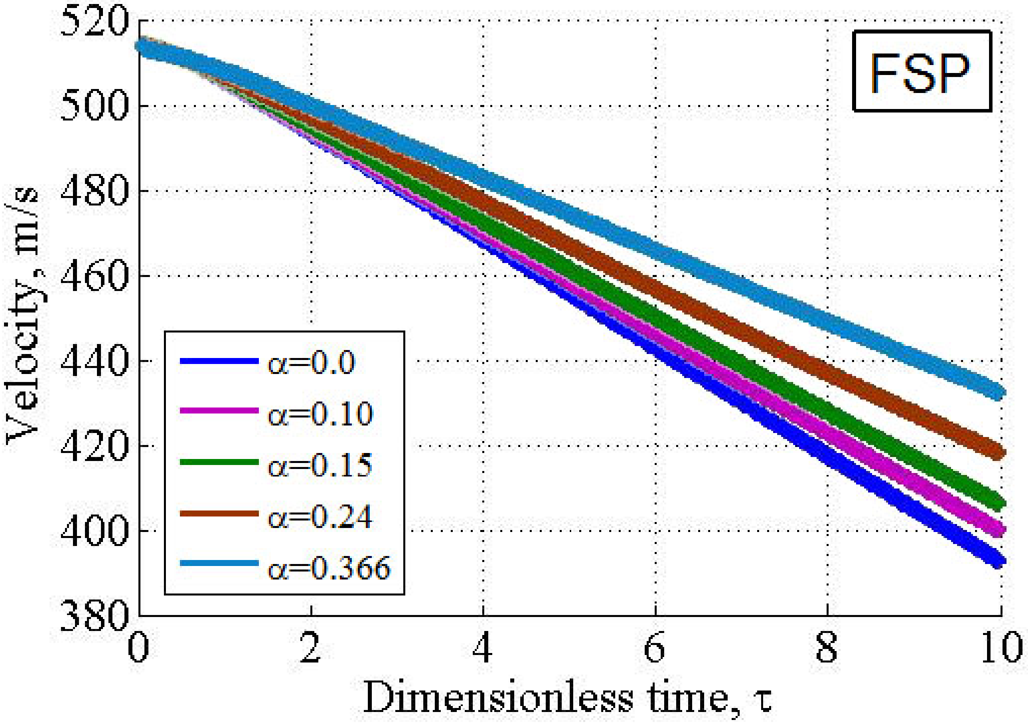

(a)

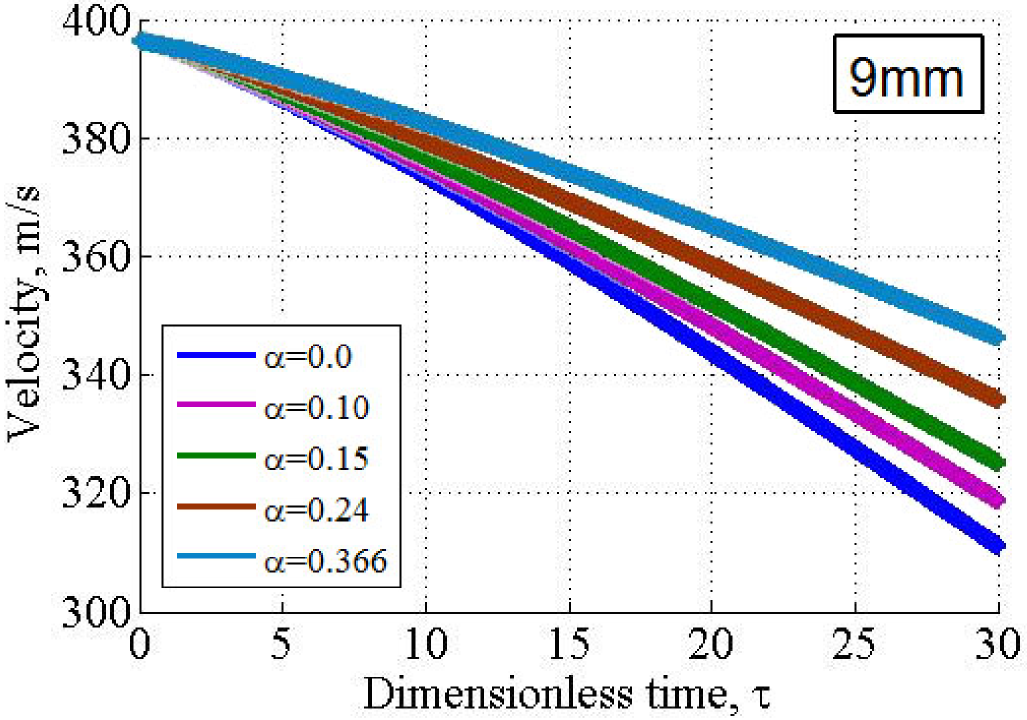

(b)

Figure 3.38. Comparison of velocity deceleration around the (a) FSP and (b) 9mm projectile for five cases of crimp using the laminar model.

Slower deceleration results in higher projectile velocities at the same points in time, which also means a greater distance/displacement that the projectile has traveled, as shown in Fig. 3.39.

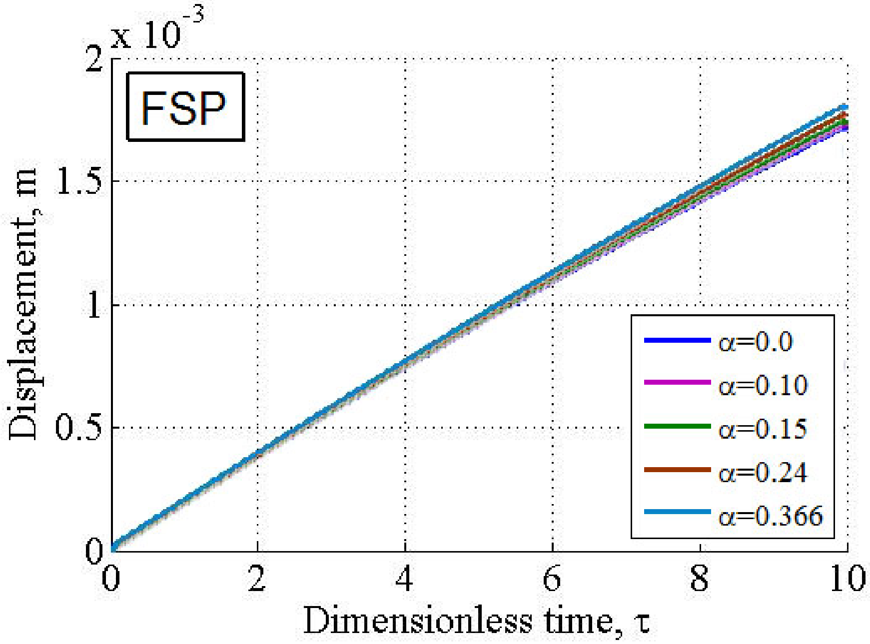

(a)

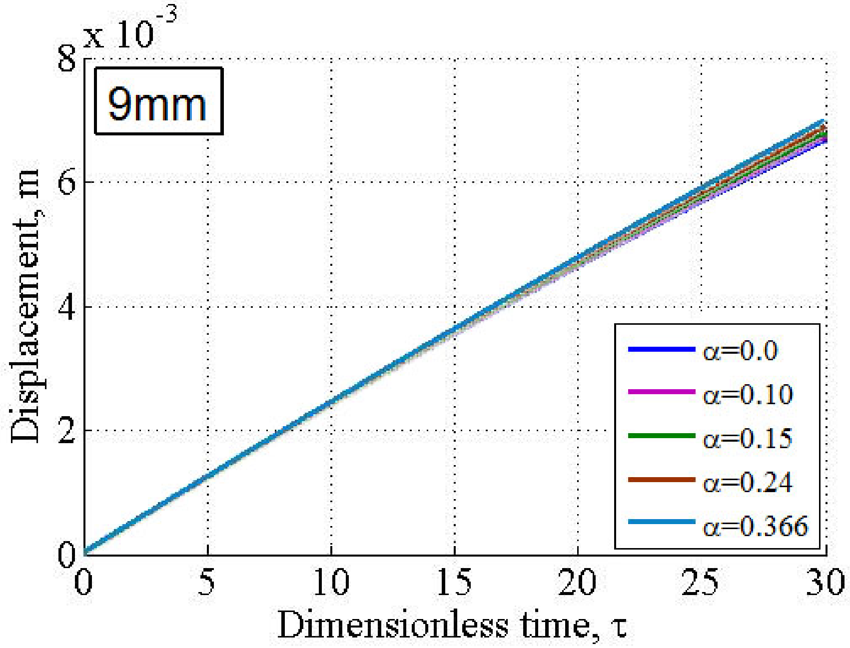

(b)

Figure 3.39. Comparison of out-of-plane displacement for the (a) FSP and (b) 9mm projectile for five cases of crimp using the laminar model.

Although projectile displacement is not a commonly used failure criterion for ballistic fabrics and experiments have shown scenarios where the projectile has advanced a significant distance into the fabric and was still completely stopped, such scenarios are not ideal. This is due to blunt trauma, where the human target's organs are still damaged to a life-threatening degree even though the projectile has stopped, illustrated in Fig. 3.40.

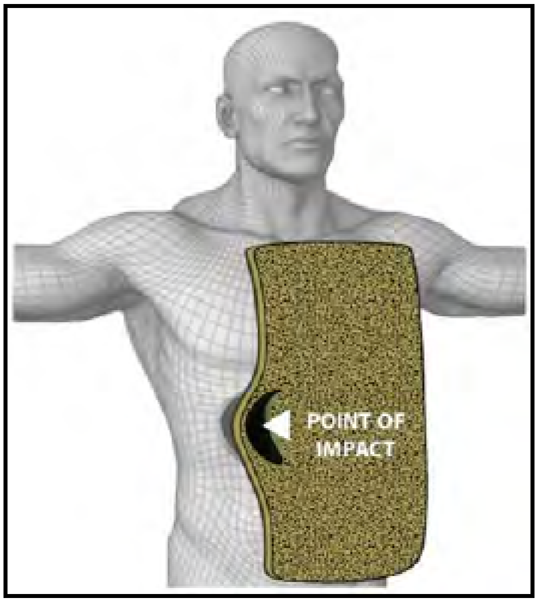

Figure 3.40. Blunt trauma resulting from excessive back face deflection, a.k.a. displacement from Fig. 3.39.

The maximum allowable BFS (back face signature) as defined by NIJ standards is 44mm. Because we assume the velocity and displacement profiles in Figs. 3.38 and 3.39 are linear, we do a quick estimate by extrapolating the velocity to 0 m/s and first look at the corresponding final displacement for the most extreme case of $\alpha = 0.366$. For the FSP, displacement at V = 0 approximates to no more than 11mm, which is well below the BFS limit given by the NIJ. However, for the 9mm, which decelerates much slower, displacement at V = 0 approximates to 56mm, which is definitely above the NIJ's BFS limit. This suggests that $\alpha = 0.366$ is not a viable amount of crimp to have in a fabric panel of this areal density. Luckily, for the second extreme case of $\alpha = 0.24$, the 9mm displacement approximates to 36mm, which is safely under the BFS limit. Overall, we believe the disadvantage in BFS caused by increasing crimp is small compared to the benefit from lowering strains. We summarize our findings from these two sections in Fig. 3.41 and note that although we only include data from Case 3c - FSP, the trends shown are representative of all the cases from Table 3.6.

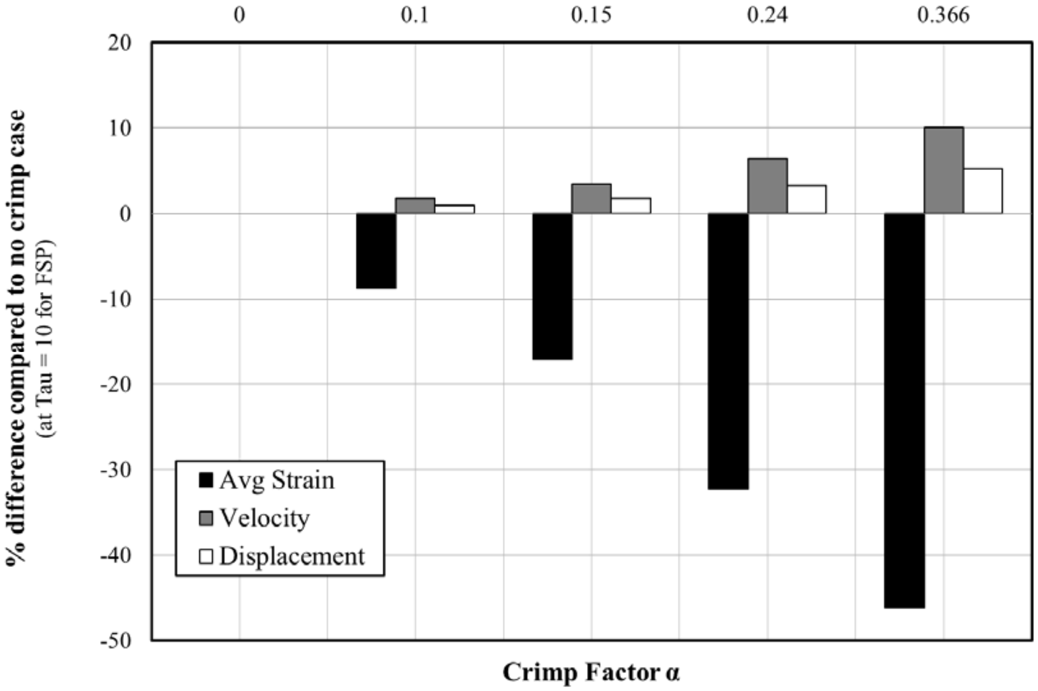

Figure 3.41. Bar graph comparing gains (lower strains) and losses (higher velocities and displacements) for ballistic performance due to crimp.

3.4.4 Effects of varying crimp on tension and cone wave propagation

From Figs. 3.42 and 3.43, we see that the tension and cone wave speeds are inversely proportional to the crimp factor α. This makes physical sense, because the more crimp in the yarns, the longer it takes to straighten them out, which slows down the waves. The decreasing intensity of color in the waves from $\alpha = 0$ (dark red) to $\alpha = 0.366$ (light blue) agrees with the trend shown in Fig. 3.36.

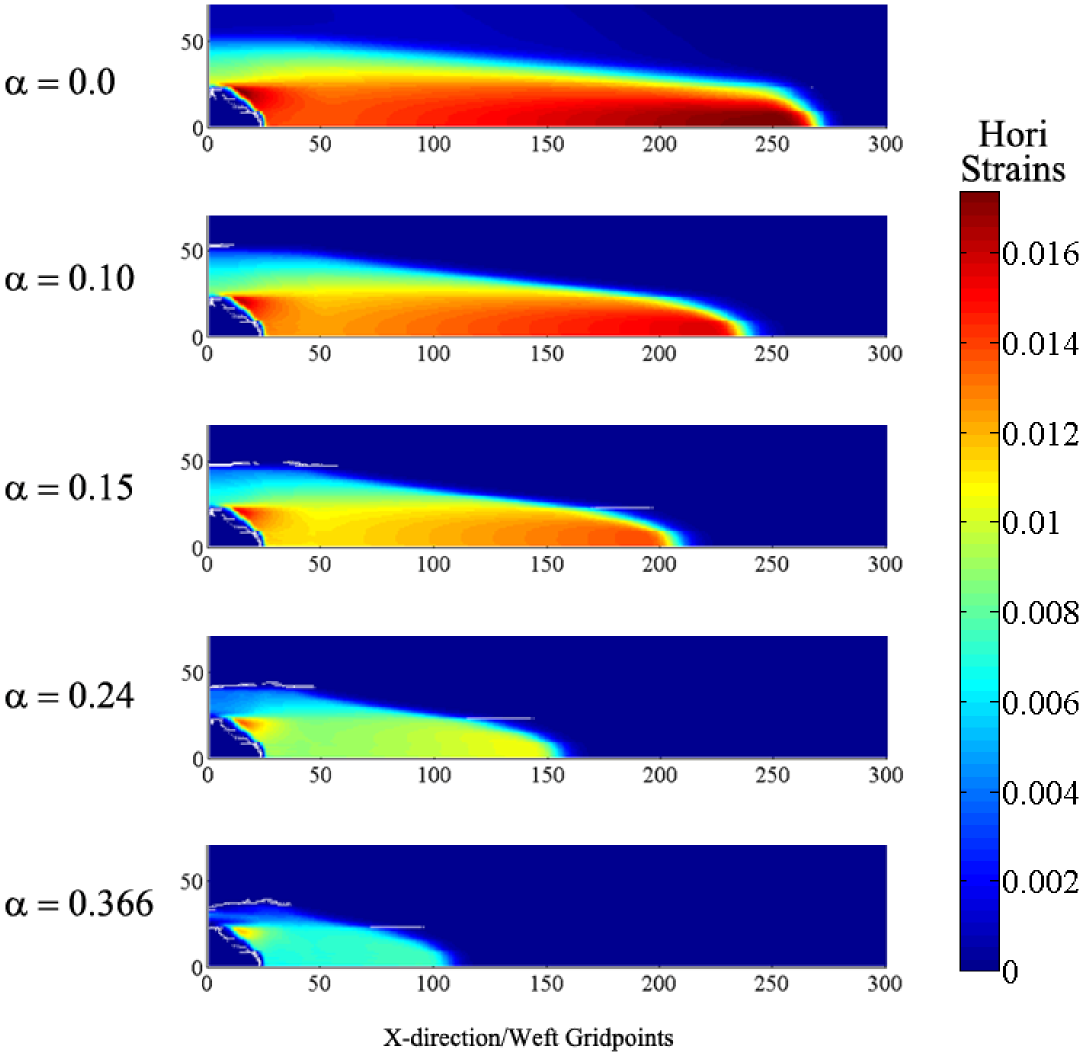

Figure 3.42. Top view of tension strain surface profile showing how far the tension wave has traveled at $T = 10$ for Case1d – FSP.

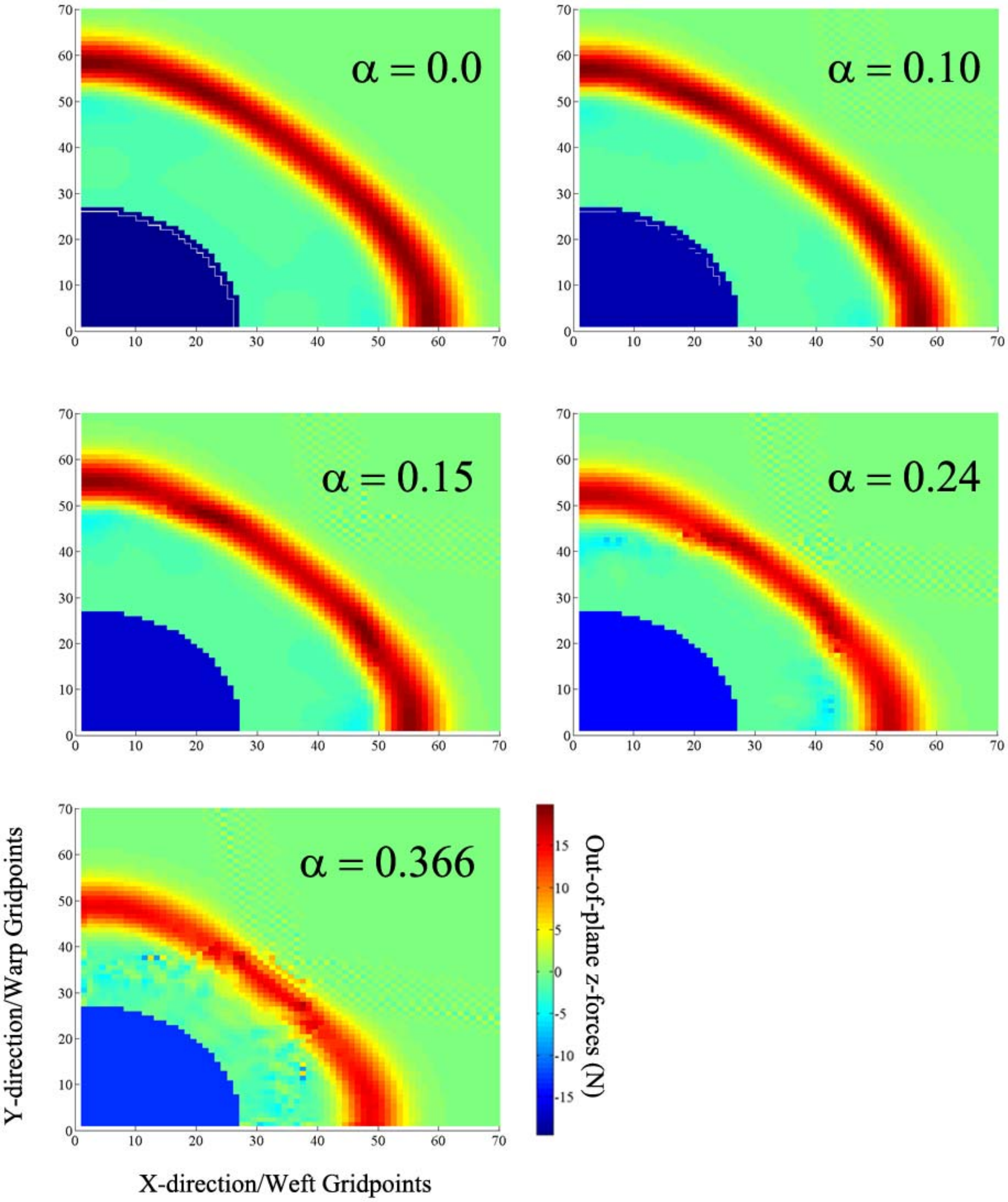

Figure 3.43. Top view of out-of-plane *z*-forces at $\mathrm{T}=10$ for $\mathrm{Case1d}-\mathrm{FSP}$.

Compared to the tension wave, which experienced a 60% decrease in waves speed from $\alpha=0$ to $\alpha=0.366$, the cone wave speed only decreased about 17%. This is expected, as the cone wave relies on in-flow material from the tension wave to grow and the lower distance traveled by the tension wave is compensated by the increased in-flow from de-crimping the yarns discussed next.

3.4.5 The de-crimping process

From Fig. 3.44, we see a similar trend as that of Fig. 3.36, indicating that the amount of de-crimped, or flattened out yarns, is proportional to how far the tension wave has traveled. Another point of interest is that although we are plotting horizontal slopes, we see that yarns along the vertical, or warp direction, are simultaneously being de-crimped. We attribute this to the way the nodes are connected to each other for the laminar model, illustrated in Fig. 3.11(a).

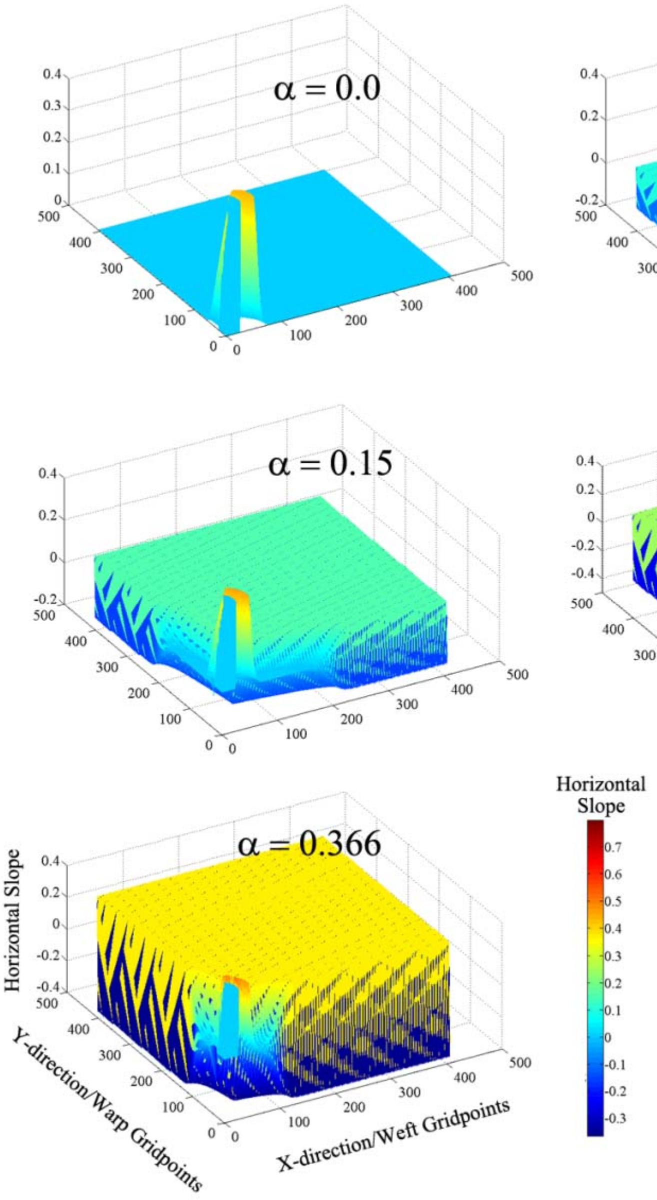

Figure 3.44. 3-D view of the fabric de-crimping process for all five crimp cases at $T = 10$ for Case1b – FSP.

In order get a better glimpse at how specific yarns within the fabric de-crimp, we take different cross-sections of Fig. 3.44 and plot them in Fig. 3.45.

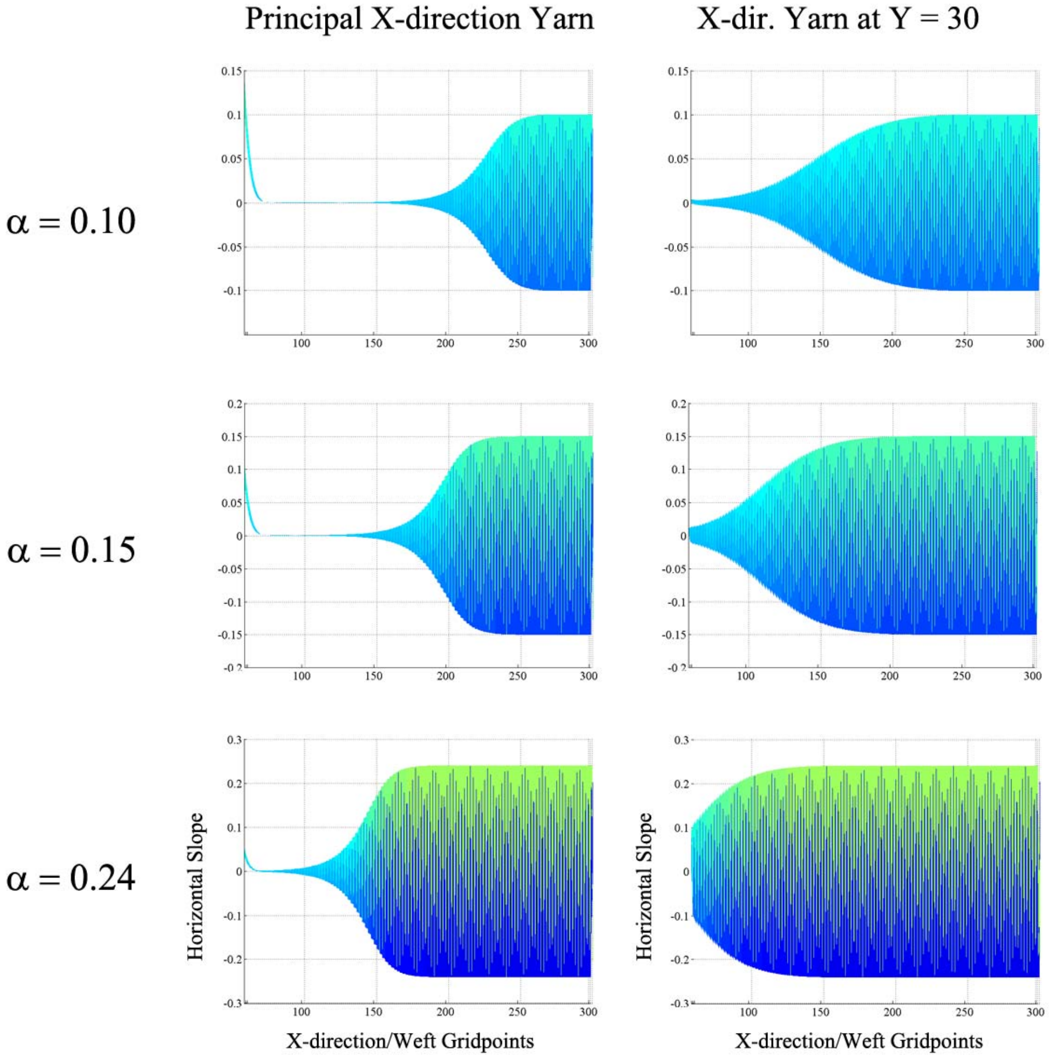

Figure 3.45. 2-D views of hori slopes along different x-axis yarns for three crimp cases at $\mathrm{T} = 10$ for Case1b – FSP.

Fig. 3.45 shows several features of the de-crimping process. First, we see that just like Fig. 3.44, principal weft yarns are de-crimped along with other secondary weft yarns, chosen to be located at Y=30 for the figure. However, the principal weft yarn experienced de-crimping before all the secondary weft yarns, hence the difference in shape between the two columns. For example, in the $\alpha = 0.1$ case, at X = 150, the principal yarn has been fully de-crimped and flattened out to have zero slope, but the secondary weft yarn is still partially crimped. Finally, we observe that for all three crimp cases, the distance it takes to fully de-crimp a yarn is the same along the same yarns.

3.4.6 Effects of varying η on ballistic performance

From Section 3.2.7, we know that η is the rocking viscosity term used to dampen oscillations. While η is included in force calculations for all three directions, it has the most effect on the *z*-direction oscillations. We first look at Fig. 3.46 to compare the effects of varying η on average strain at $\mathrm{T} = 10$.

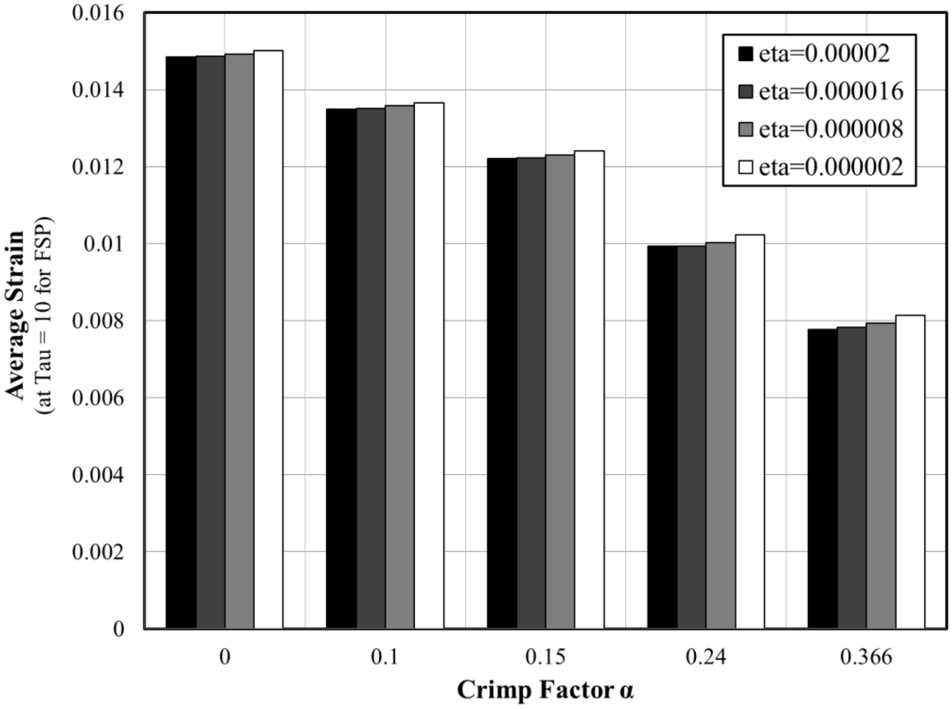

Figure 3.46. Bar graph showing effects of varying η on average strain for all five crimp cases at $\mathrm{T} = 10$ for Cases1a-1d – FSP.

While Fig. 3.46 shows that average strains at $T = 10$ (and probably for longer times) are slightly higher as η decreases, we realize that $T = 10$ is a somewhat late time for the FSP, whose strains peak around $T = 5$. We now plot Fig. 3.47 to see the effects of varying η on average strain at earlier times for the case of $\alpha = 0.15$.

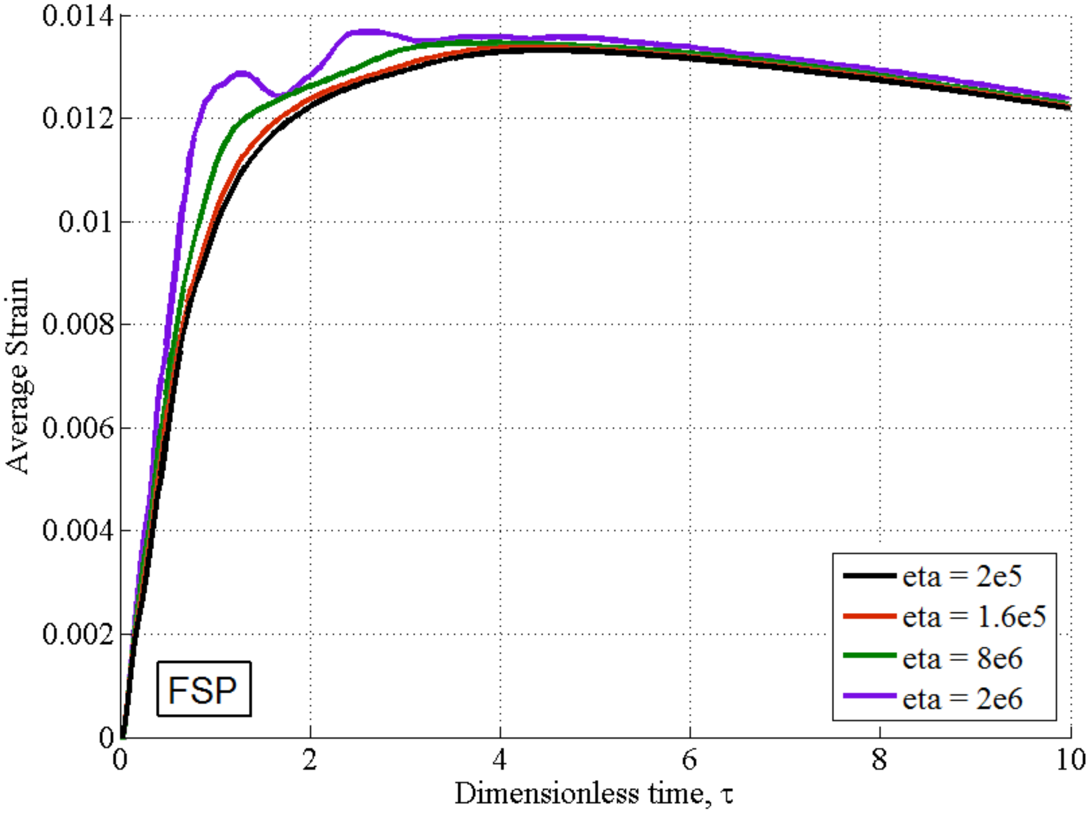

Figure 3.47. Comparison of average strain around the FSP for all four cases of η using the laminar model. Results include Cases1a-1d – FSP – $\alpha = 0.15$.

With Fig. 3.47, it is very clear which oscillations would occur before T = 4 in the case of a low η value. To see the very large effect η has on out-of-plane *z*-forces, we plot the two extreme cases of η = 2e5 and η = 2e6 in Fig. 3.48.

After looking at the effect of η in the z-direction, we would also like to see what effects, if any, η has in the in-plane directions.

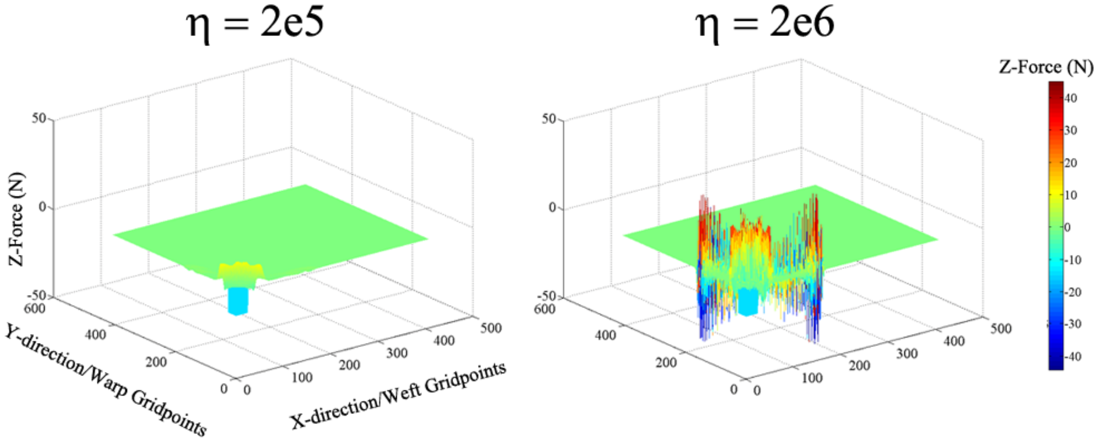

Figure 3.48. 3-D view of the out-of-plane z-forces for two extreme η values. Results include Cases1b and 1c – FSP – $\alpha = 0.24$.

We now plot the in-plane velocities, for the two cases in Fig. 3.49. From this figure, we see that the edges of the in-plane velocity profile for the higher η is round and smooth, while the profile for the lower η is sharp and jagged. This makes sense because a higher η means more damped motion, and although the velocity rapidly changes from 0 m/s (flat blue region) to 136.5 m/s (red region), it cannot do so in a sharp, sudden manner because it is limited by the higher η.

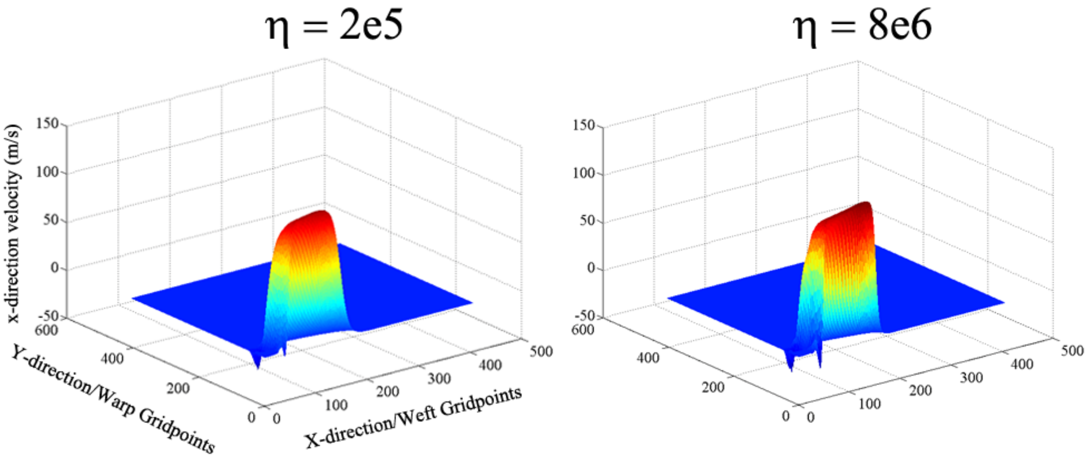

Figure 3.49. 3-D view of the out-of-plane *z*-forces for two different η values. Results include Cases3b and 3c – FSP – α = 0.24.

3.4.7 Effects of varying ζ on ballistic performance

From Section 3.2.7, we know that ζ is the slip viscosity term used to determine how much slip or sliding occurs between the projectile and the yarns in contact with it underneath. When this slip is allowed to occur, we observe a wave collision within the impact region very soon after impact, as described by the schematic in Fig. 3.21. This event is also discussed in Section 2.5. We now track this event in real-time from a sequence of images produced from our simulation in Fig. 3.50.

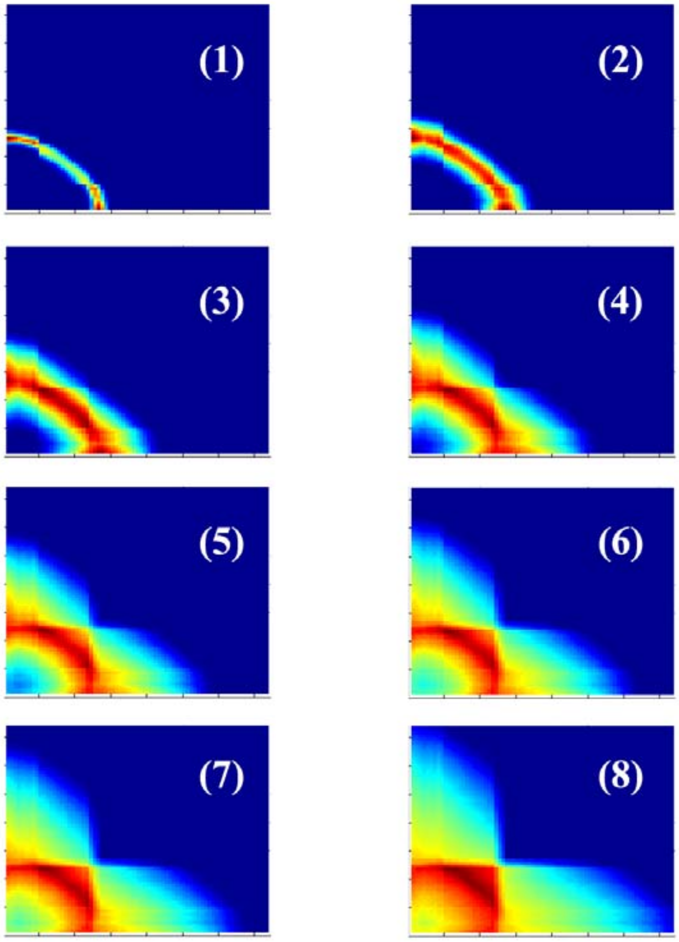

Figure 3.50. Plot of Eq. (3.45) in real-time as a sequence of (1) – (8), showing the inward wave collision and the outward propagating waves.

To see the impact of this wave collision (shock) on the projectile edge strain over time, we plot Fig. 3.51 for two extreme cases of ζ .

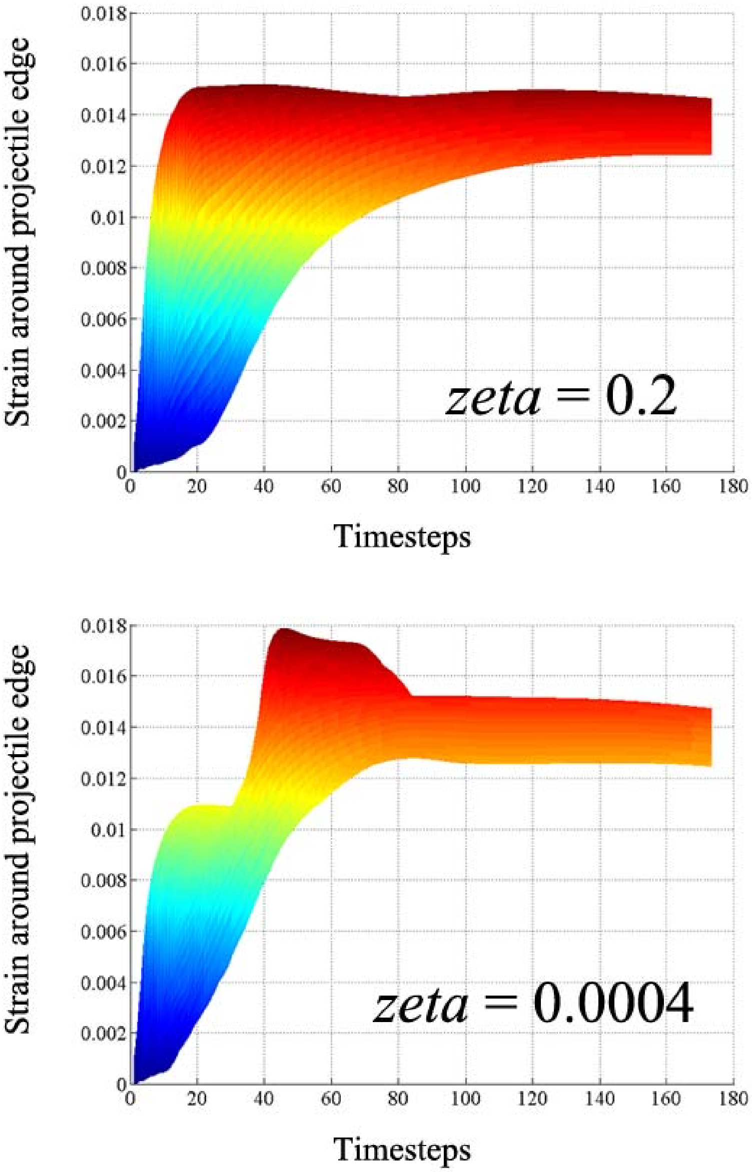

Figure 3.51. Plot of strain around the projectile edge over time for two extreme ζ . Results include Cases4c and 4b – FSP – $\alpha = 0.10$.

We first conclude that ζ is proportional to friction force and inversely proportional to slip. When $\zeta = 0.2$ (higher value), barely any slip occurs between the projectile and yarns underneath it. Hence we hardly see much of a shock wave effect in the upper plot. However, when there is low friction and lots of slip ($\zeta = 0.0004$), we see the shock wave effect very clearly in the lower plot. There is a jump in strain (i) starting around Timestep = 30, (ii) reaching its peak around Timestep = 48, and (iii) ending at Timestep = 84. These coincide with the times when (i) the fringes of the inner propagating waves are in contact with one another, (ii) the waves collide at the origin point, (iii) the waves propagate outwards past the projectile edge. Nevertheless, if we look closely at the upper plot, we notice that these events still occurred since there is a minor dip in strain at Timestep = 84.

Another very fascinating aspect of this strain jump is its agreement with the analytical prediction from Section 2.5, namely Eq. (2.33). For the ζ = 0.0004, $\alpha = 0.1$ case shown in Fig. 3.51, we track the peak strain to be 0.1781 and take the strain at the end of the simulation to be 0.1469. Substituting these values into Eq. (2.32) gives

$$K_{sc} = \frac{\varepsilon_{SC}}{\varepsilon_{\infty}} = \frac{0.1781}{0.1469} = 1.21, \tag{3.51}$$

which yields a remarkable 3% error when compared with $K_{\mathrm{SC}} \approx \sqrt[3]{2}$! This result is remarkable because (i) the analytical model does not account for crimp, (ii) the analytical result was derived for a 1-D impact case, and (iii) the time we picked for reading ε_{∞} occurred at $\mathrm{T} = 10$, which is not really a long time. At very long times, the value of ε_{∞} would actually be a bit smaller than the value we used in Eq. (3.51), which would make the agreement even closer.

3.5 Summary

We developed a FD-numerical model which incorporated laminar crimp to study fabric performance (esp. the de-crimping process) under the impact of a flat-nosed cylindrical projectile. We modeled the yarns as a network of pin-jointed nodes (where each node was connected to its four surrounding neighbors) with mass-spring-damper characteristics. The following conclusions can be made from our simulation results:

(1) Increasing crimp in yarns has the benefit of lowering yarn strains, which would in turn increase critical velocities (V_{50}). The tradeoff with lower strains is slower projectile deceleration and more BFS. However, we show with our results that for most impact cases where the crimp factor is not excessively high, the BFS does not exceed the limit set by NIJ.

(2) Increasing crimp lowers the velocity of the tension waves, since now the waves have to straighten out the crimp, before it can move forward.

(3) The de-crimping process for our laminar model is unique in the sense that when crimp is pulled out in one direction, the in-plane perpendicular direction's crimp is pulled out as well.

(4) The parameter η is important to our simulations because it dampens out large oscillations in the system, especially in the out-of-plane *z*-direction.

(5) The parameter ζ is important to our model because it controls the amount of projectile-yarn slip that can occur. For small ζ, friction is also small, and we observe a wave collision underneath the projectile, which has significant effects on strain.

CHAPTER 4

WOVEN CRIMP MODEL FOR BI-AXIAL FABRICS

4.1 Introduction

After the development of our laminar crimp model, presented in Chapter 3, we observed that (i) most ballistic fabrics are made from weaving yarns one over another, which did not resemble the geometry of our model, (ii) the crimp interchange phenomenon was not observed in our modeling results, and (iii) our model did not include many features such as out-of-plane compression and in-plane yarn-yarn slip.

4.2 Finite-difference simulation

We still use the forward finite-difference (FD) method to numerically solve the single-layer ballistic impact problem with woven crimp. The assumptions we make are the same as in our previous model, listed in Section 3.2. We also follow the same general algorithm as shown in Fig. 3.8. The main differences between our two models are: (i) interlaced geometry of the yarn and (ii) force definitions. While the boundary conditions remain unchanged from a physical perspective, the resolving of forces at each node is different between the two models due to the change in geometry.

4.2.1 Initial input and calculated parameter values

We present a list of additional physical parameters necessary to execute our numerical code in Table 4.1, which supplements Table 3.1. Table 3.2 remains the same for our woven crimp model.

Table 4.1: A list of additional physical parameters used as initial programming values

Additional User-Input Parameters		
Name	Notation	Description
mu_x_inter	$\mu_{x,\text{inter}}$	yarn-yarn slip viscosity constant in the *x*-direction
mu_y_inter	$\mu_{y,\text{inter}}$	yarn-yarn slip viscosity constant in the *y*-direction
kx_inter	$k_{x,\text{inter}}$	shear spring stiffness in the *x*-direction
ky_inter	$k_{y,\text{inter}}$	shear spring stiffness in the *y*-direction
kz_inter	$k_{z,\text{inter}}$	out-of-plane tension-compression spring stiffness
etaz	η_z	stretch viscosity constant
Additional Calculated Parameters		
Name	Notation	Description
AD_alpha	AD_α	adjusted areal density due to extra material from crimp
m_gp_alpha	$m_{\text{gp},\alpha}$	adjusted mass of fabric due to change in AD_α
v_proj0_a	$v_{\text{proj},0,\alpha}$	adjusted velocity right after impact due to change in AD_α

We show a visual of the forces influenced by $\mu_{x,\text{inter}}$, $\mu_{y,\text{inter}}$, $k_{x,\text{inter}}$, $k_{y,\text{inter}}$, $k_{z,\text{inter}}$, and η_z in relation to other forces in Section 4.2.2. Their use in specific force calculations is presented in Section 4.2.4.

AD_α is the adjusted areal density due to the presence of extra material once yarns are crimped in the fabric. We calculate it by

$$AD_\alpha = AD \cdot (\mathrm{A})^2, \tag{4.1}$$

where the crimp-related length ratio A is given by Eq. (3.14). From Table 3.5, we note that A values are just slightly above unity for crimped cases, and when squared and multiplied by *AD*, they cause the adjusted AD_α to be no higher than 14% more than the original *AD*. This change in *AD* has been observed previously (Shim, et al., 1995).

Due to this adjustment, we also have corresponding adjustments for $m_{\mathrm{gp},\alpha}$ and $v_{\mathrm{proj},0,\alpha}$, given by

$$m_{\mathrm{gp},\alpha} = AD_{\alpha} \cdot dl^{2} \tag{4.2}$$

$$v_{\mathrm{proj},0,\alpha} = v_{\mathrm{proj}} \cdot \frac{m_{\mathrm{proj}}}{(\pi R_{\mathrm{proj}}^{2} \cdot AD_{\alpha} + m_{\mathrm{proj}})}. \tag{4.3}$$

We should note that, in principle, these same adjustments apply to the laminar crimp model of Chapter 3, but were not exploited there.

4.2.2 Fabric layout and crimp

To model the over-under interlacing of woven yarns in the fabric, we must double the number of mass nodes (one set for each yarn orientation, hori and vert), and change the way our nodes are connected to each other. In contrast to the laminar crimp model in Fig. 3.9(a), where each node was connected to four other nodes, we now have each node connected to two other nodes along the same yarn, as shown in Fig. 4.1(a) and (b). Fig. 4.1(c) shows the un-crimped state of woven yarns, and Fig. 4.2 shows the fabric in a crimped state with yarns represented by the network of nodal masses. Our model's resulting fabric layout with hori and vert yarns is shown in Fig. 4.3.

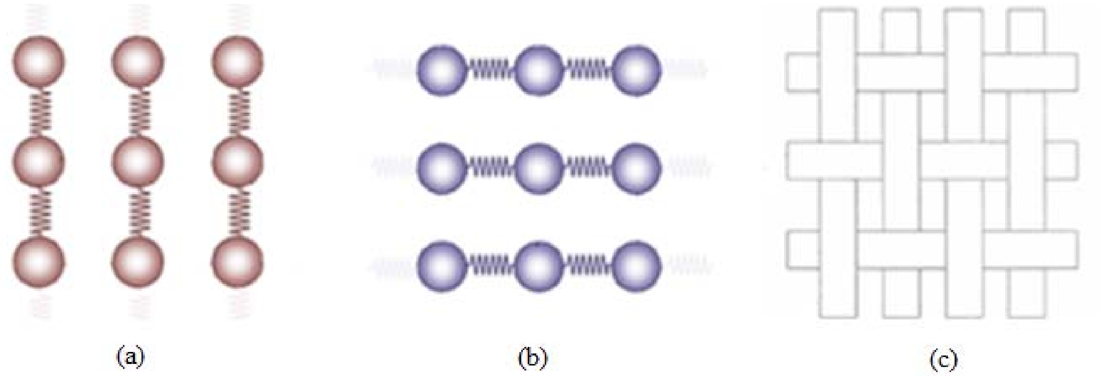

Figure 4.1. Mass-spring system representing woven geometry where each node is connected to two other nodes for (a) vert yarns and (b) hori yarns. (c) Schematic of interlaced vert and hori yarns, represented in (a) and (b), respectively, by springs and masses.

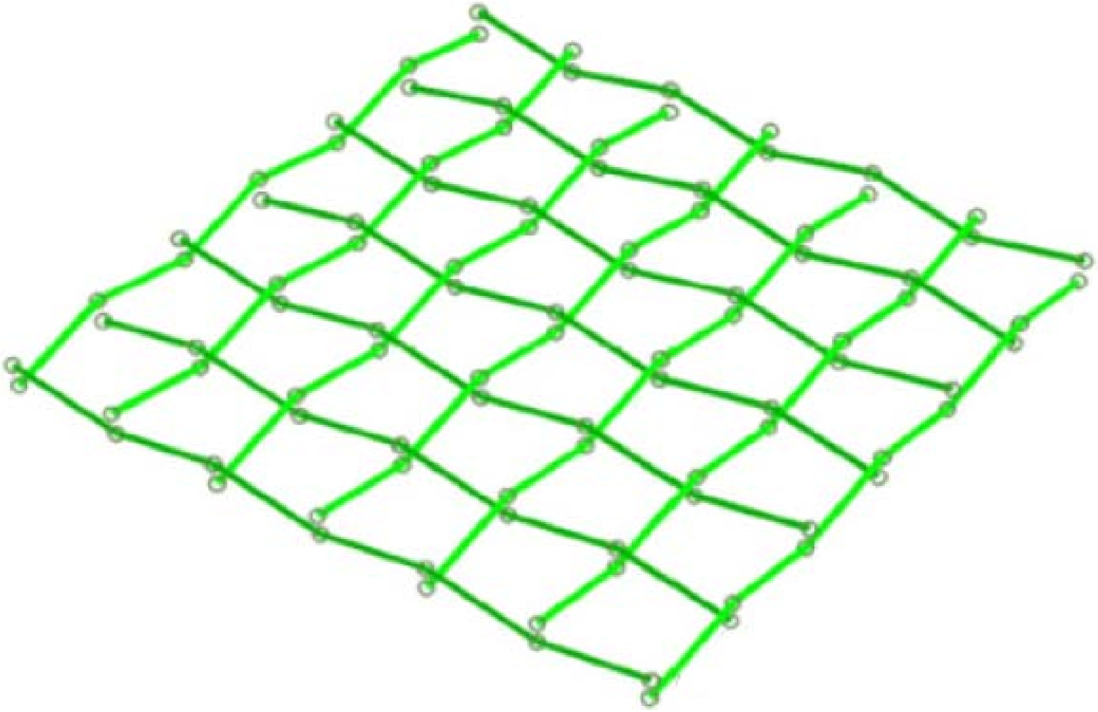

Figure 4.2. Network of nodes in crimped state for woven model (Zeng et al., 2006).

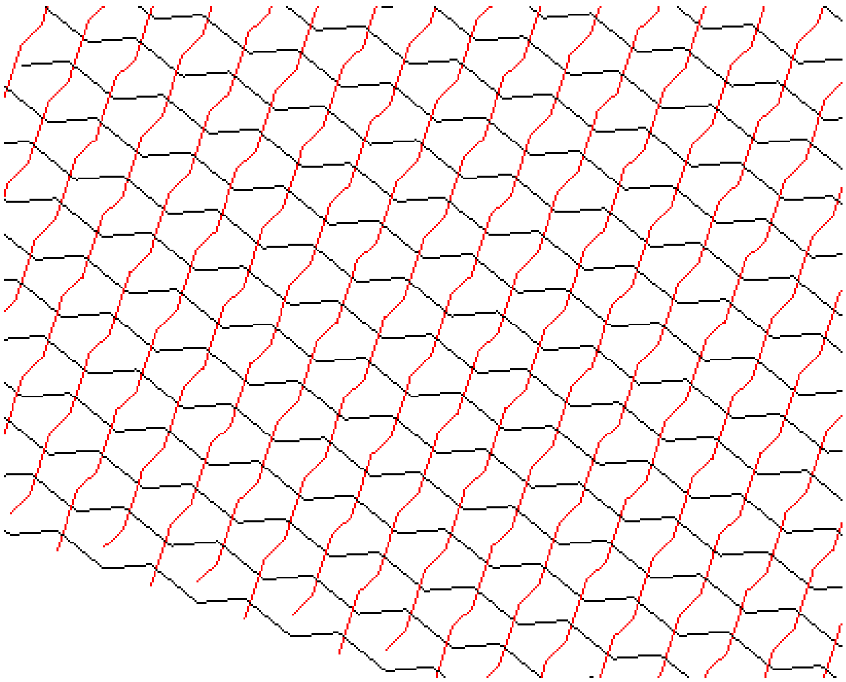

Figure 4.3. Graphical output from our model showing fabric yarn positions at some arbitrary time *t* after impact but before failure. Black lines represent weft or "hori" yarns. Red lines represent warp or "vert" yarns.

We note from Fig. 4.2 and 4.3 that in this woven crimp model, since each node is connected to only two other nodes, an "up" node on a hori yarn at location *i,j* would correspond to a "down" node on a vert yarn at that same location, and vice versa. This is the opposite of the laminar crimp model shown in Fig. 3.14, where the "up" node for a hori yarn at location *i,j* would also be an "up" node for a vert yarn at that location. Nevertheless, we still define the *z*-positions of crimped nodes by Eq. (3.16). An additional yet crucial condition of this geometrical change is the relative motion between the hori and vert yarn at every cross-over *i,j* location. There can be out-of-plane tension and/or compression, as well as in-plane sliding due to nodal relative position and velocity differences, once deformation begins, as shown in Fig. 4.4.

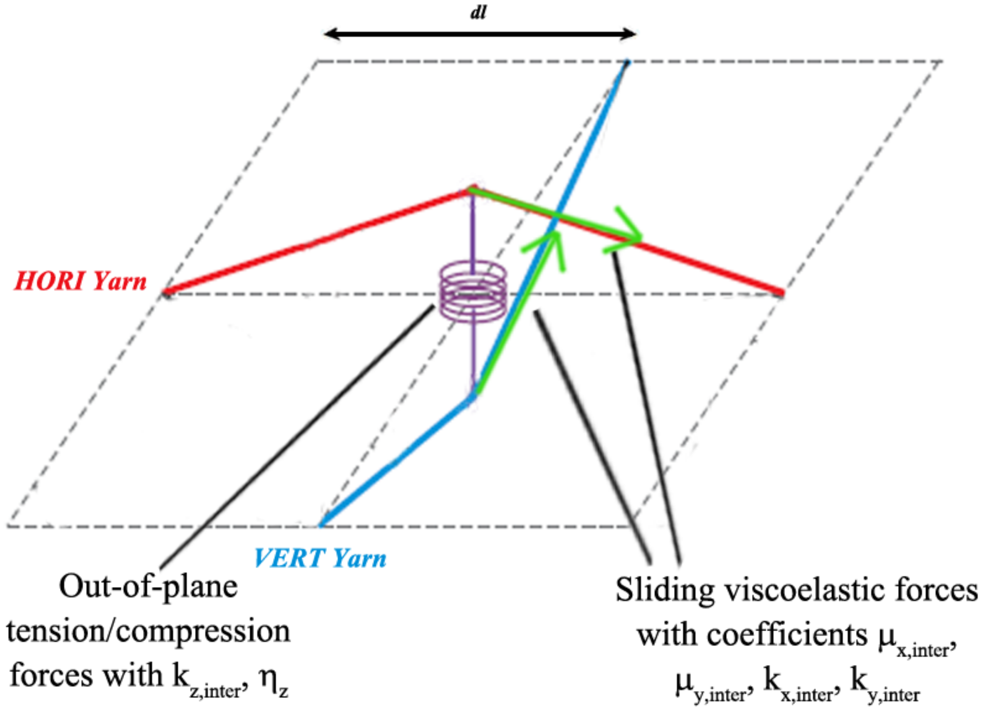

Figure 4.4. Schematic of a cross-over node point where there are various forces which describe the “inter” yarn motion between hori and vert yarns.

We observe from Fig. 4.4 that due to the existence of the “inter” yarn forces, if we attempt to de-crimp or flatten out one yarn, it would actually cause the other yarn to become more crimped, and vice versa. This is a property of woven fabrics known as crimp interchange, and has been well-documented in the literature since the 1970s (Cavallaro, 2011; Grujicic et al., 2008; King et al., 2005; Parsons, et al., 2013).

4.2.3 Strain and relative velocity formulations

We retain the set of various length differences and strain definitions given by Eq. (3.17) – (3.26) from Section 3.2.6. However, since we now have the inter-yarn forces in our woven crimp model, it is necessary to define six new length differences:

$$x_{\text{inter,vert}} = x_{\text{HORI}}(i,j) - x_{\text{VERT}}(i,j) \qquad (4.4(a))$$

$$x_{\text{inter,hori}} = x_{\text{VERT}}(i,j) - x_{\text{HORI}}(i,j) \qquad (4.4(b))$$

$$y_{\text{inter,vert}} = y_{\text{HORI}}(i,j) - y_{\text{VERT}}(i,j) \qquad (4.5(a))$$

$$y_{\text{inter,hori}} = y_{\text{VERT}}(i,j) - y_{\text{HORI}}(i,j) \qquad (4.5(b))$$

$$z_{\text{inter,vert}} = z_{\text{HORI}}(i,j) - z_{\text{VERT}}(i,j) \qquad (4.6(a))$$

$$z_{\text{inter,hori}} = z_{\text{VERT}}(i,j) - z_{\text{HORI}}(i,j)\,. \qquad (4.6(b))$$

We do not model rotations between spring/damping elements, representing out-of-plane, inter-nodes between vert and hori yarns, since these elements act as virtual 'spacers' keeping the yarns separated at cross-overs (which of course is always the case since yarns cannot inter-penetrate each other). Thus we do not have a need for the equivalent of Eqs. (3.23) and (3.24). However, we still define the strain-related parameters with units of [1/Length] similar to Eq. (3.25) particularly to reflect yarn squishing and the Hertzian contact effects that bring the centers of the crossing yarns vertically closer together. To calculate *x*-and *y*-direction shear strains between crossover nodes, we define:

$$ix_{\text{inter,vert}} = \frac{x_{\text{inter,vert}}}{(dl \cdot \alpha)^2} \qquad (4.7(a))$$

$$ix_{\text{inter,hori}} = \frac{x_{\text{inter,hori}}}{(dl \cdot \alpha)^2} \qquad (4.7(b))$$

$$iy_{\text{inter,vert}} = \frac{y_{\text{inter,vert}}}{(dl \cdot \alpha)^2} \qquad (4.8(a))$$

$$iy_{\text{inter,hori}} = \frac{y_{\text{inter,hori}}}{(dl \cdot \alpha)^2}\,. \qquad (4.8(b))$$

For the out-of-plane *z*-direction tensile driver between crossover nodal masses, we define the following:

$$iz_{\text{inter,vert}} = \frac{1}{dl \cdot \alpha} - \frac{1}{\left|z_{\text{inter,vert}}\right|} \tag{4.9(a)}$$

$$iz_{\text{inter,hori}} = \frac{1}{dl \cdot \alpha} - \frac{1}{\left|z_{\text{inter,hori}}\right|}, \tag{4.9(b)}$$

where the absolute value sign is used to ensure that the iz_{inter} terms are appropriately positive when the element separating two nodes is in tension (which rarely occurs) or negative in compression.

For relative velocities, we retain Eq. (3.2.8) but define additional terms to describe the motion between hori and vert nodes at crossover points:

$$\Delta vx_{\text{inter,vert}} = vx_{\text{HORI}}(i,j) - vx_{\text{VERT}}(i,j) \tag{4.10(a)}$$

$$\Delta vx_{\text{inter,hori}} = vx_{\text{VERT}}(i,j) - vx_{\text{HORI}}(i,j) \tag{4.10(b)}$$

$$\Delta vy_{\text{inter,vert}} = vy_{\text{HORI}}(i,j) - vy_{\text{VERT}}(i,j) \tag{4.11(a)}$$

$$\Delta vy_{\text{inter,hori}} = vy_{\text{VERT}}(i,j) - vy_{\text{HORI}}(i,j) \tag{4.11(b)}$$

$$\Delta vz_{\text{inter,vert}} = vz_{\text{HORI}}(i,j) - vz_{\text{VERT}}(i,j) \tag{4.12(a)}$$

$$\Delta vz_{\text{inter,hori}} = vz_{\text{VERT}}(i,j) - vz_{\text{HORI}}(i,j). \tag{4.12(b)}$$

To update the positions for each time step increment, we modify Eq. (3.8) for the *x*-direction in the simpler laminar crimp version of the code to now read

$$vx^{t}_{\text{VERT}}(i,j) = vx^{t-\Delta t}_{\text{VERT}}(i,j) + \frac{fx^{t}_{\text{VERT}}(i,j)}{massx_{\text{VERT}}(i,j)} \cdot dt \tag{4.13(a)}$$

$$vx^{t}_{\text{HORI}}(i,j) = vx^{t-\Delta t}_{\text{HORI}}(i,j) + \frac{fx^{t}_{\text{HORI}}(i,j)}{massx_{\text{HORI}}(i,j)} \cdot dt\,. \tag{4.13(b)}$$

We also update the velocities per time step increment by writing Eq. (3.9) for the *x*-direction in simpler laminar crimp version of the code as

$$x^{t}_{\text{VERT}}(i,j) = x^{t-\Delta t}_{\text{VERT}}(i,j) + vx^{t}_{\text{VERT}}(i,j) \cdot dt \tag{4.14(a)}$$

$$x^{t}_{\text{HORI}}(i,j) = x^{t-\Delta t}_{\text{HORI}}(i,j) + vx^{t}_{\text{HORI}}(i,j) \cdot dt\,. \tag{4.14(b)}$$

4.2.4 Force formulations

We retain the set of force definitions given by Eq. (3.32) from Section 3.2.7 and add six more forces to model inter-yarn motion. In the *x*- and *y*-directions we have:

$$fx_{\text{inter,vert}} = \mu_{\text{x,inter}} \cdot \Delta vx_{\text{inter,vert}} + k_{\text{x,inter}} \cdot ix_{\text{inter,vert}} \cdot dl \cdot \alpha \tag{4.15(a)}$$

$$fx_{\text{inter,hori}} = \mu_{\text{x,inter}} \cdot \Delta vx_{\text{inter,hori}} + k_{\text{x,inter}} \cdot ix_{\text{inter,hori}} \cdot dl \cdot \alpha \tag{4.15(b)}$$

$$fy_{\text{inter,vert}} = \mu_{\text{y,inter}} \cdot \Delta vy_{\text{inter,vert}} + k_{\text{y,inter}} \cdot iy_{\text{inter,vert}} \cdot dl \cdot \alpha \tag{4.16(a)}$$

$$fy_{\text{inter,hori}} = \mu_{\text{y,inter}} \cdot \Delta vy_{\text{inter,hori}} + k_{\text{y,inter}} \cdot iy_{\text{inter,hori}} \cdot dl \cdot \alpha\,, \tag{4.16(b)}$$

where $kx_{\text{inter}} \cdot ix_{\text{inter,hori}} \cdot dl \cdot \alpha$ corresponds to the kx term from Eq. (3.31) and $\mu_{\text{x,inter}} \cdot \Delta vx_{\text{inter,vert}}$ corresponds to the $c\dot{x}$ term from Eq. (3.31) in the previous laminar crimp code. Since all the forces have units of N, and $ix_{\text{inter,hori}} \cdot dl \cdot \alpha$ is dimensionless, we find that kx_{inter} has units of N and $\mu_{\text{x,inter}}$ has units of $\left[mass/length^{2} \cdot time\right]$, or $\left[kg/m^{2} \cdot s\right]$.

For the out-of-plane *z*-direction inter-motion, we allow for compression to occur by not putting any restrictions on Eq. (4.6). However, we realize that within the simulation it would be possible for the masses to get close and mathematically interpenetrate and pass through one another, as shown in Fig. 4.5. Obviously, such an occurrence is physically impossible.

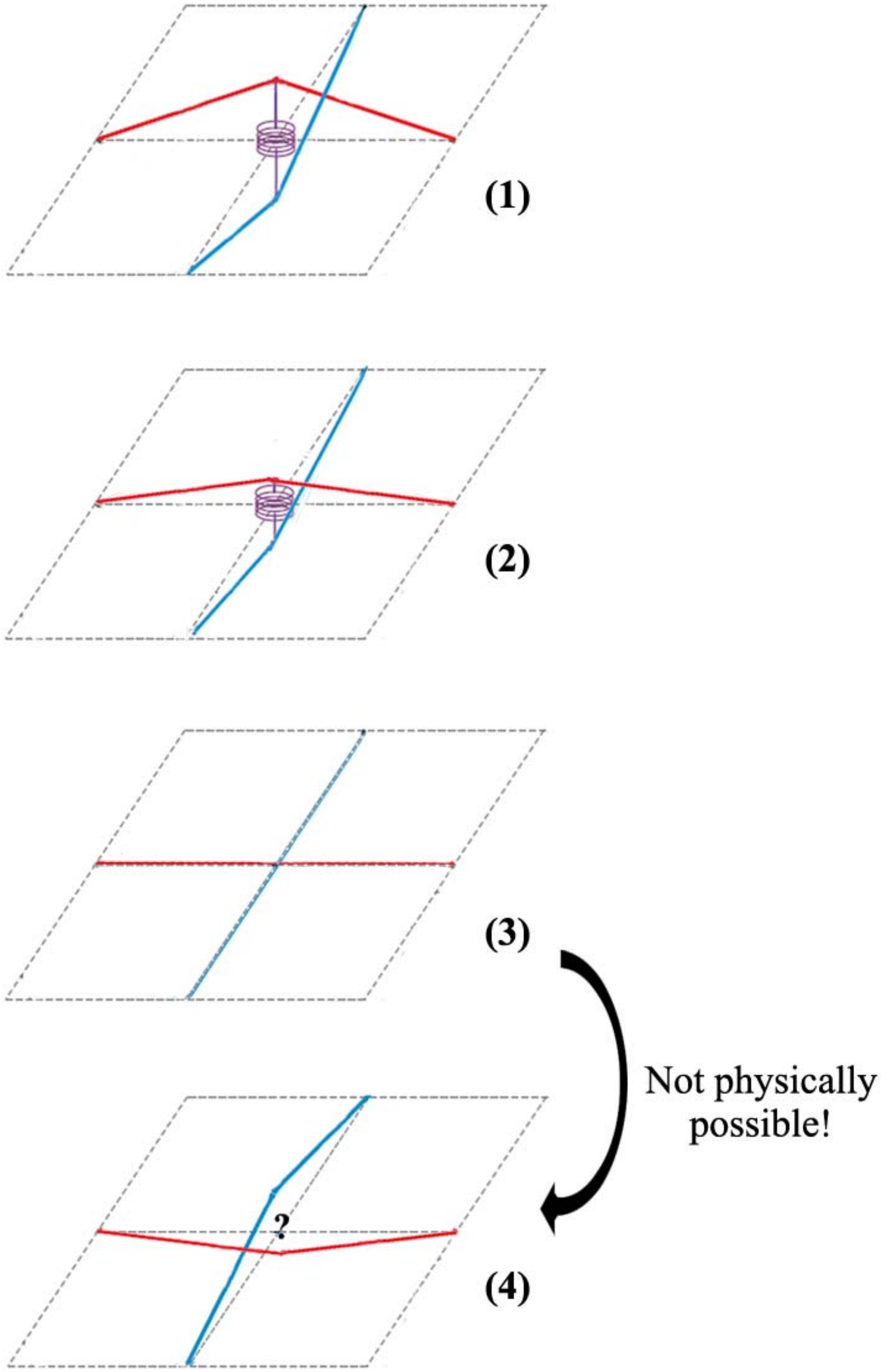

Figure 4.5. Series of diagrams showing too much compression between nodes at a cross-over point leading to non-physical switching of over-under positions for the two yarns.

To prevent the phenomenon in Fig. 4.5 from occurring in our simulation, we define the position-related term in our force calculations such that it resembles a "Hertzian" force:

$$fz_{\text{inter,vert}} = \frac{kz_{\text{inter}} \cdot iz_{\text{inter,vert}} \cdot z_{\text{inter,vert}}}{\min\left(\left|1 + iz_{\text{inter,vert}} \cdot \left|z_{\text{inter,vert}}\right|\right|, 1\right)} + \eta_z \cdot \Delta vz_{\text{inter,vert}} \tag{4.17(a)}$$

$$fz_{\text{inter,hori}} = \frac{kz_{\text{inter}} \cdot iz_{\text{inter,hori}} \cdot z_{\text{inter,hori}}}{\min\left(\left|1 + iz_{\text{inter,hori}} \cdot \left|z_{\text{inter,hori}}\right|\right|, 1\right)} + \eta_z \cdot \Delta vz_{\text{inter,hori}} \cdot \tag{4.17(b)}$$

Fig. 4.6 shows the qualitative concept of a "Hertzian"-like force applied to our geometry. As z_{inter} gets smaller, the two nodal masses get closer, and the force increases rapidly to infinity, thus making it impossible for the nodes to go through each other.

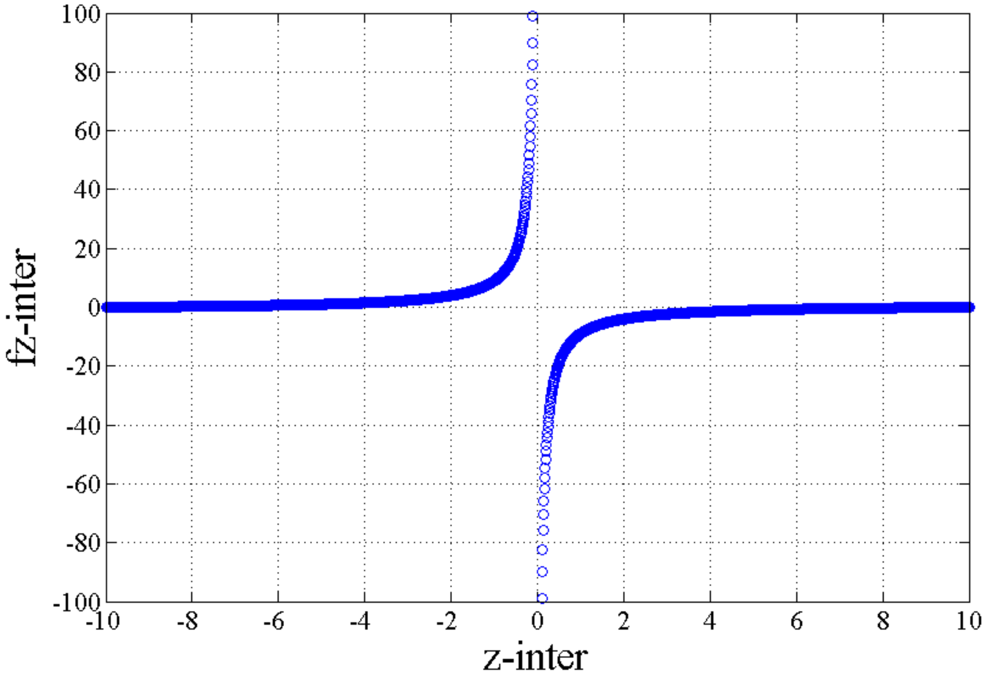

Figure 4.6. Graph of "Hertzian"-like force fz_{inter} as a function of z_{inter}.

We then resolve all the element forces per direction using the equations above at each *i,j* node location, similar to Eq. (3.33), listed here for the *x*-direction:

$$fx^{t}_{\text{VERT}}(i,j) = fx^{t-\Delta t}_{\text{VERT}}(i,j) + fx_{\text{vert}} + fx_{\text{inter,vert}} \tag{4.18(a)}$$

$$fx^{t}_{\text{VERT}}(i,j+1) = fx^{t-\Delta t}_{\text{VERT}}(i,j+1) - fx_{\text{vert}} \tag{4.18(b)}$$

$$fx^{t}_{\text{HORI}}(i,j) = fx^{t-\Delta t}_{\text{HORI}}(i,j) + fx_{\text{hori}} + fx_{\text{inter,hori}} \tag{4.18(c)}$$

$$fx^{t}_{\text{HORI}}(i+1,j) = fx^{t-\Delta t}_{\text{HORI}}(i+1,j) - fx_{\text{hori}}\,. \tag{4.18(d)}$$

We follow the same process outlined in Section 3.2.7 for summing and redistributing *z*-forces for nodes in contact with the projectile and for applying slip damping to those nodes. Our equations for incorporating frictional forces due to slip in the *x*-direction are the following:

$$fx^{t}_{\text{HORI}}(i,j) = fx^{t-\Delta t}_{\text{HORI}}(i,j) + \zeta \cdot \min(fz^{t}_{\text{HORI}}(i,j),0) \cdot vx^{t}_{\text{HORI}}(i,j) \tag{4.19(a)}$$

$$fx^{t}_{\text{VERT}}(i,j) = fx^{t-\Delta t}_{\text{VERT}}(i,j) + \zeta \cdot \min(fz^{t}_{\text{VERT}}(i,j),0) \cdot vx^{t}_{\text{VERT}}(i,j)) \tag{4.19(b)}$$

Finally, we note that forces at the boundaries are treated in the same fashion as described in Section 3.2.8, and the two types of smoothing mechanisms were applied in the same fashion as described in Section 3.2.10.

4.3 Guide to reading graphs

In addition to the graphs shown for the laminar crimp model in Chapter 3, we present two types of new graphs unique to the woven crimp model here.

4.3.1 Yarn contact compression

To determine how much compression between nodes at crossover points, we define:

$$Compression(i,j) = \frac{z_{\mathrm{VERT}}(i,j) - z_{\mathrm{HORI}}(i,j)}{dl \cdot \alpha} \quad , \tag{4.20}$$

with the corresponding plot shown in Fig. 4.7(a). We use $dl \cdot \alpha$ as the standard for comparison because it is the z-distance between the two nodes initially before impact and in a fully crimped state. When this compression value crosses over the $z = 0$ line from positive to negative or vice versa, we know that the nodal masses have gone through each other, which is physically impossible, signifying that the simulation needs to be redone with different parameter values (see Fig. 4.5). However, it is difficult to determine whether this unrealistic event occurred without zooming into Fig. 4.7(a), so we define its absolute value

$$Compression_{\mathrm{ABS}}(i,j) = \frac{\left| z_{\mathrm{VERT}}(i,j) - z_{\mathrm{HORI}}(i,j) \right|}{dl \cdot \alpha} \tag{4.21}$$

and graph it in Fig. 4.7(b) to get an easier reading. For general scenarios where the nodal masses have not gone through each other, we can still look at graphs like Fig. 4.7 to see how much compression has occurred at the cross-over points, and relate this to the magnitude of certain parameter values.

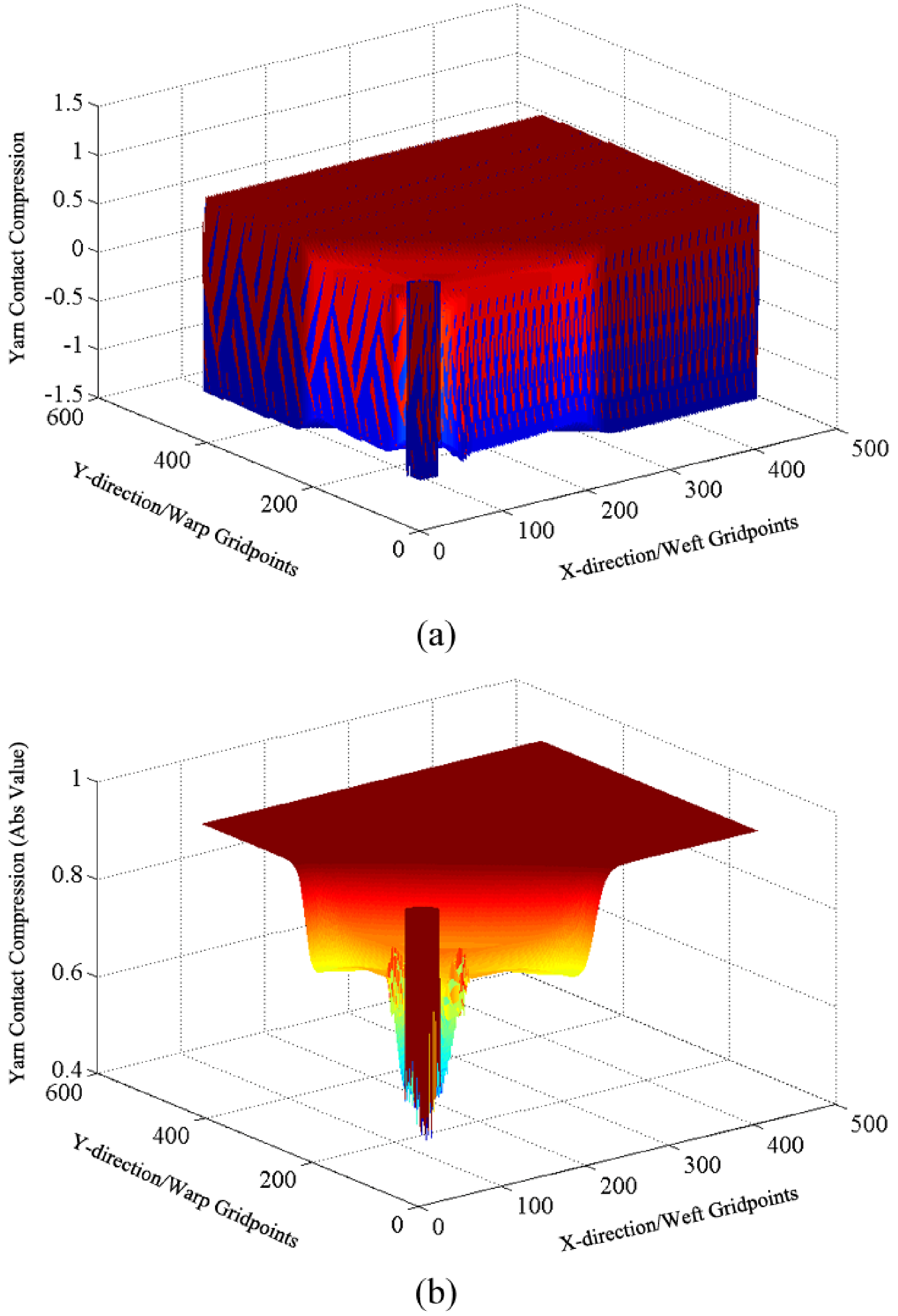

Figure 4.7. Graph of (a) the amount of compression between hori and vert nodes at cross-over points, and (b) its absolute value.

4.3.2 Yarn contact sliding

To determine how much sliding occurs between nodes at crossover points, we define:

$$Sliding(i,j) = \frac{x_{\mathrm{VERT}}(i,j) - x_{\mathrm{HORI}}(i,j)}{dl \cdot \mathrm{A}}, \qquad (4.22)$$

with the plot shown in Fig. 4.8. *Sliding(i,j)* is a dimensionless ratio representing the current in-plane distance between the two nodes at a crossover point relative to the original distance between two adjacent nodes lying on the same yarn. In our results, we observe the shape of this surface profile to see the effects of varying the coefficients $\mu_{\mathrm{x,inter}}$, $\mu_{\mathrm{y,inter}}$, $k_{\mathrm{x,inter}}$, and $k_{\mathrm{y,inter}}$. Note in this example plot (representing a fairly extreme case) that the maximum amount of sliding is one or two node spacings along a yarn.

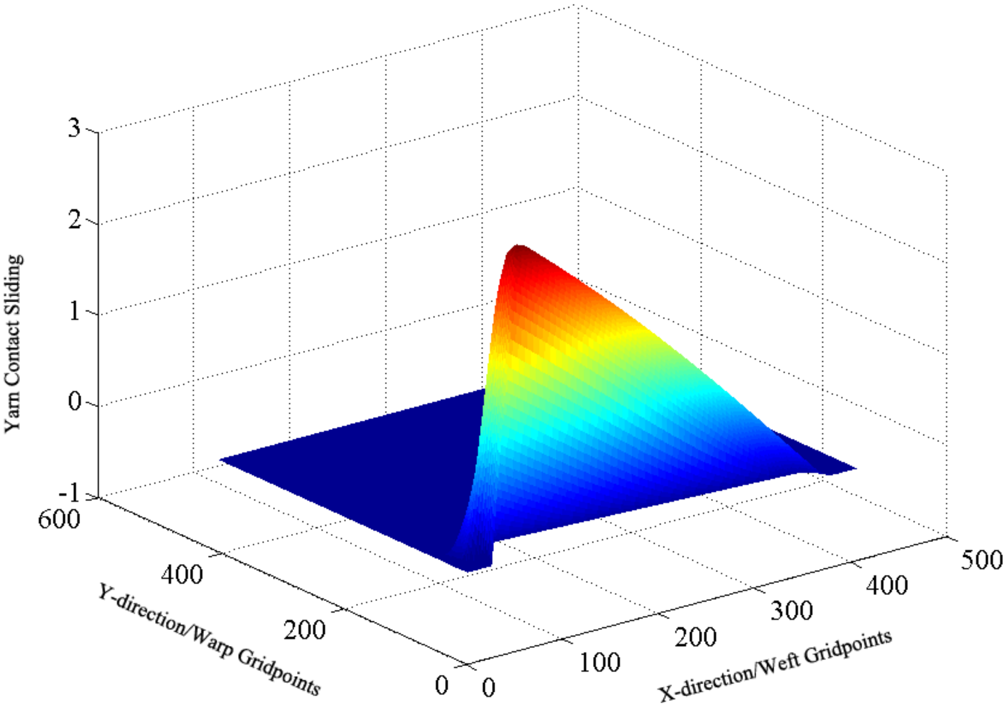

Figure 4.8. Graph of showing amount of sliding between hori and vert nodes at cross-over points.

4.4 Results and discussion

We present the results for our woven crimp model in this section along with analysis and discussion. First, we discuss the influence of crimp on post-ballistic fabric behavior. Next, we compare our results from this model to the laminar crimp model results (from Chapter 3), followed by discussion of compression (out-of-plane) and slip (in-plane) effects involving the role of various coefficients. Comparisons with analytical findings presented in Chapter 2 are interspersed throughout.

4.4.1 Key parameter value combinations

The values we used in our simulations for the additional user-input parameters from Table 4.1 are listed in Table 4.3. We also provide a summary in Table 4.2 of which coefficients were applied to which relative displacement and velocity terms in the force calculations from Section 4.2.4.

Table 4.2: Summary of which position or velocity term each coefficient controls

Parameter	Applied to $(\cdot)$ for nodes at crossover points
$\mu_{x,\text{inter}}$	x-component of relative hori and vert velocities
$\mu_{y,\text{inter}}$	y-component of relative hori and vert velocities
$k_{x,\text{inter}}$	x-component of relative hori and vert positions
$k_{y,\text{inter}}$	y-component of relative hori and vert positions
$k_{z,\text{inter}}$	z-component of relative hori and vert positions
η_z	z-component of relative hori and vert velocities

Table 4.3: Initial input values for additional parameters in the woven crimp model, where η = 8E-06 and ζ = 0.08 for all cases.

	Simulation Input Parameter Values			
Case	η_z	$\mu_{x-,y\text{-inter}}$	$k_{x-,y\text{-inter}}$	$k_{z\text{-inter}}$
1a	2	0.02	0	100
1b	0.5	0.02	0	100
1c (*)	0.8	0.02	0	100
1d	2	0.02	0	50
1e (**)	0.8	0.02	0	50
2a	0.8	0.02	0	10
2b	0.8	0.02	0	125
2c	Same as above (**) case			
2d (*)	Same as above (*) case			
3a	0.8	0.2	0	100
3b	0.8	0.002	0	100
3c	0.8	0.08	0	100
3d (*)	Same as above (*) case			
4a	0.8	0.2	200	50
4b	0.8	0.2	0.5	50
4c	0.8	0.002	200	50
4d	0.8	0.002	0.5	50

We note that for each one of the cases in Table 4.3, all five crimp cases from Table 3.5 were run, as well as both projectile cases from Table 3.4. Selected plots of interest from the cases listed above are presented in the next section.

4.4.2 Effects of varying crimp on strain

Although the woven crimp model presented in this chapter has very different geometry than the laminar crimp model, it can be seen from Figs. 4.9 - 4.12 that the general trends in (i) lower strains with higher crimp, (ii) slower velocity deceleration with higher crimp, and (iii) more out-of-plane displacement with higher crimp all still apply. However, we explore the differences between the two models in the next section. We keep in mind that although the two models may yield similar average strain or velocity values, the process of de-crimping or arriving at those values may yet be vastly dissimilar, so from that perspective the close similarity in behavior is quite surprising.

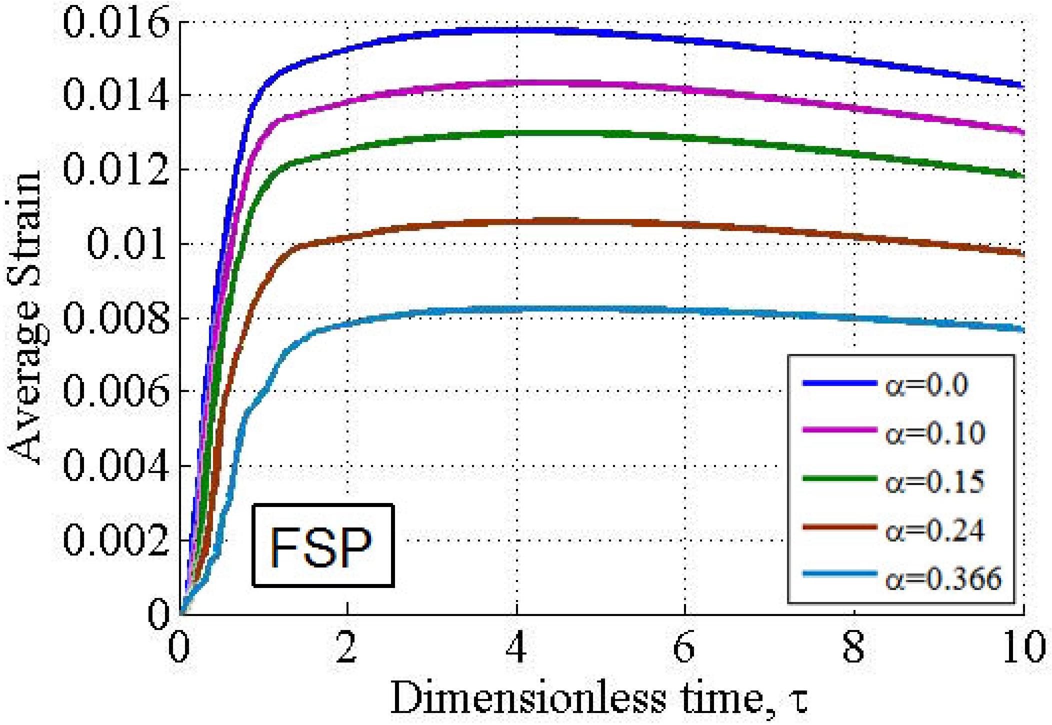

Figure 4.9. Comparison of average strain around the FSP for five cases of crimp using the woven model. Results for Case 3a from Table 4.3 are shown here.

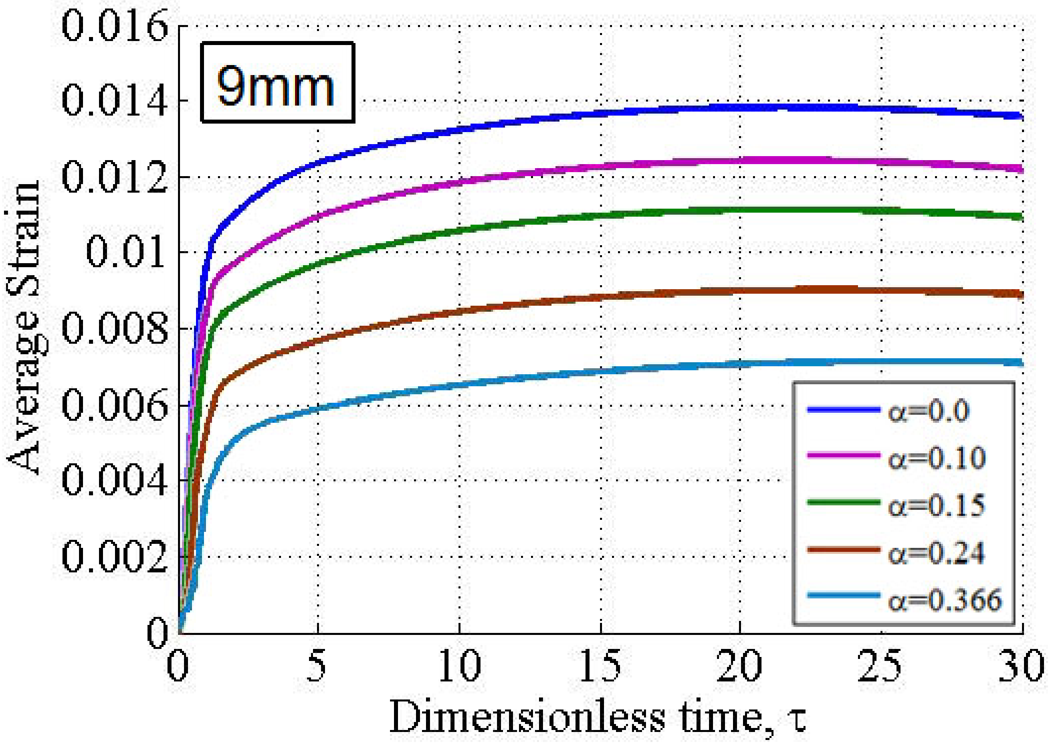

Figure 4.10. Comparison of average strain around the 9mm for five cases of crimp using the woven model. Results are for Case 3a from Table 4.3.

It is also interesting to see that, compared with the curves Figs. 3.34 and 3.35, Figs. 4.9 and 4.10's curves are much smoother, especially for higher α cases. We believe that the geometry of the woven fabric allows for greater flexibility in movement for the yarns, which in turns relieves some of the oscillations in strain present at the beginning of the simulation. Like our previous predictions and findings, the 9mm strains peak at a much later time than the FSP's, and within Fig. 4.9 and 4.10, we observe that the time when the strain peaks is later for cases of higher crimp. This makes sense because we know that more crimp causes slower tension waves, so the whole process of strain building up to a maximum and then going down is delayed.

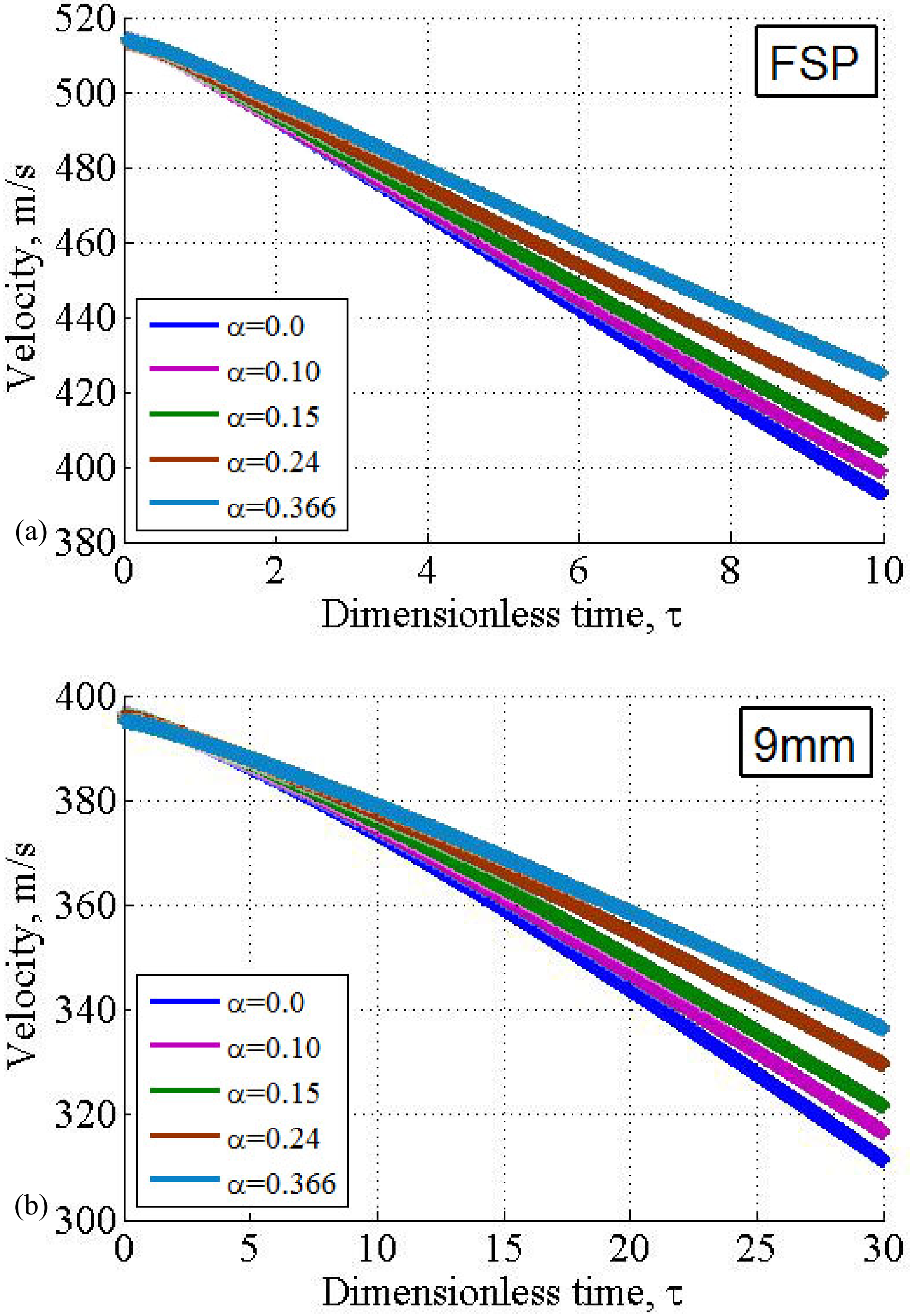

Figure 4.11. Comparison of velocity decay over time for the (a) FSP and (b) 9mm projectile for five cases of crimp using the woven model.

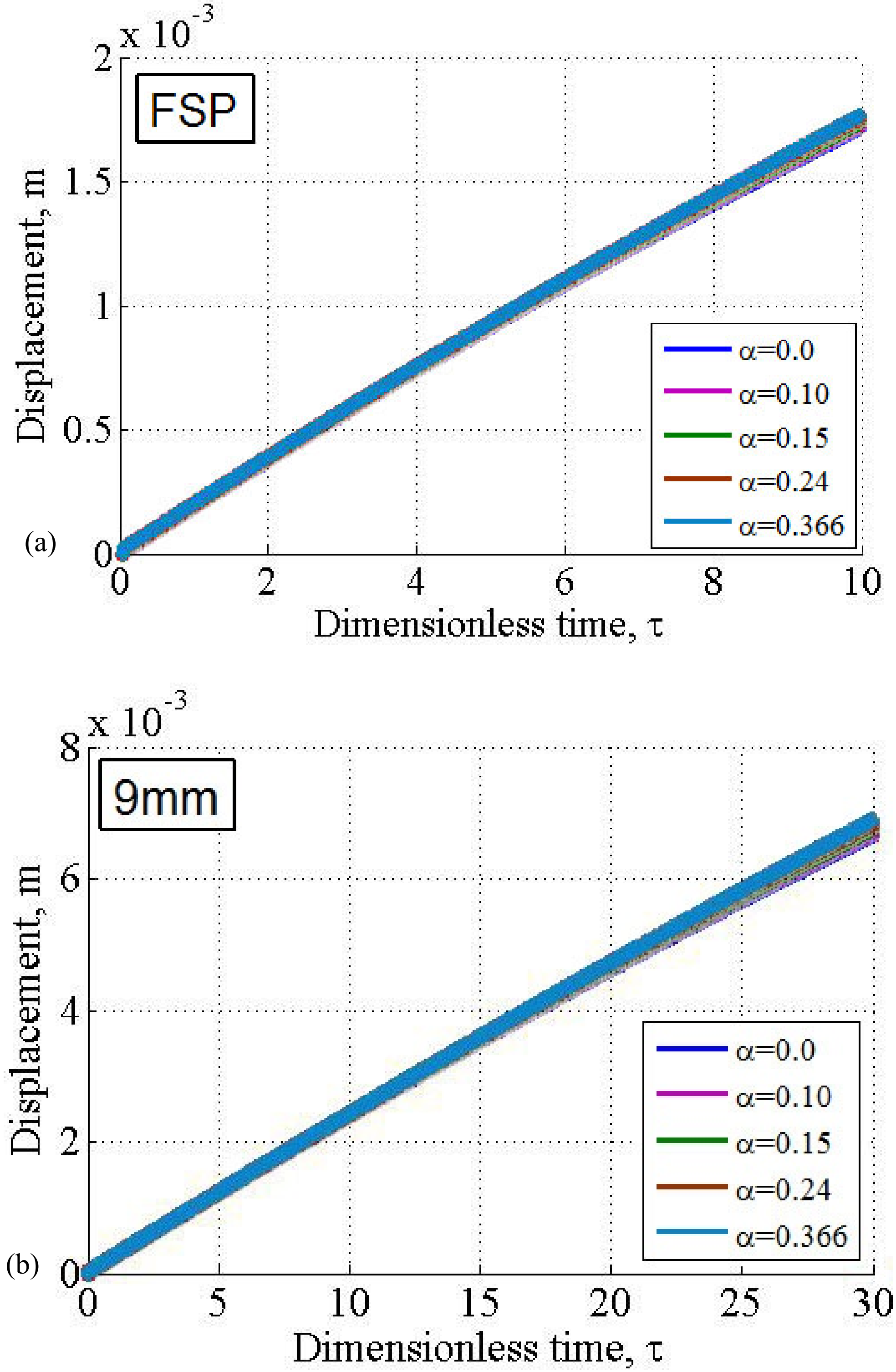

Figure 4.12. Comparison of out-of-plane displacement for the (a) FSP and (b) 9mm projectile for five cases of crimp using the woven model.

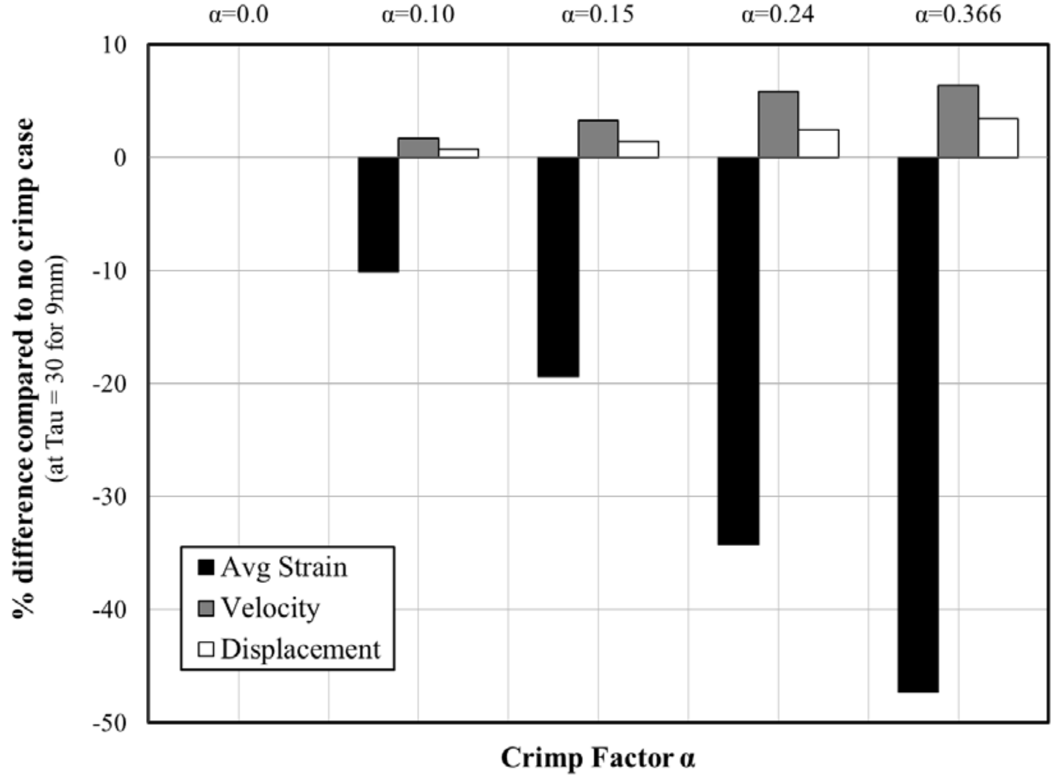

Figure 4.13. Bar graph comparing gains (lower strains) and losses (higher velocities and displacements) for ballistic performance due to crimp.

Similar to the laminar crimp model results from Fig. 3.39, Fig. 4.13 shows that the gains achieved by adding crimp outweigh the losses. We do not compare exact values with Fig. 3.39 because there are more parameters involved in this model, and adjusting one or more may cause slight variations in resulting values. Compared to the laminar crimp model, the general trend however, remains unchanged regardless of how we adjust our new parameters.

4.4.3 Comparison of laminar and woven model results

In order to compare our laminar model (two parameters) to our woven model (8 parameters) without attempting to compare "apples and oranges," we looked at our simulation results for all the cases from Table 4.3 to find one which was most similar to our laminar model's results. We were looking specifically for agreement between $\alpha = 0$ cases where there was no crimp in the fabric, and we ended up selecting Case 3a. All the figures (except Fig. 4.18) from the woven model's results in this section are made from Case 3a simulation results.

Likewise, we needed to select a case for comparison from the laminar model's cases listed in Table 3.6. Since we did not include slip underneath the projectile for the woven model, we would not consider Cases 3a-4c. This only left Case 1d, as it is the only case whose η and ζ values were the same between the two models. All the figures from the laminar model's results in this section are made from Case 1d simulation results.

Fig. 4.14 plots the velocity deceleration for the two extreme cases of crimp: $\alpha = 0$ and $\alpha = 0.366$. From it, we observe that even though the velocity decay profiles for the two models are nearly identical in the no crimp case, the differences between the two models do in fact grow as the crimp factor increases. This can be attributed to the effect of crimp interchange in the woven model, which provides a secondary stiffening effect as the yarn strain profiles around the edge of the projectile are quite different between the two cases. This is also evident in Fig. 4.15, since with no crimp, the two strain profiles appear nearly identical.

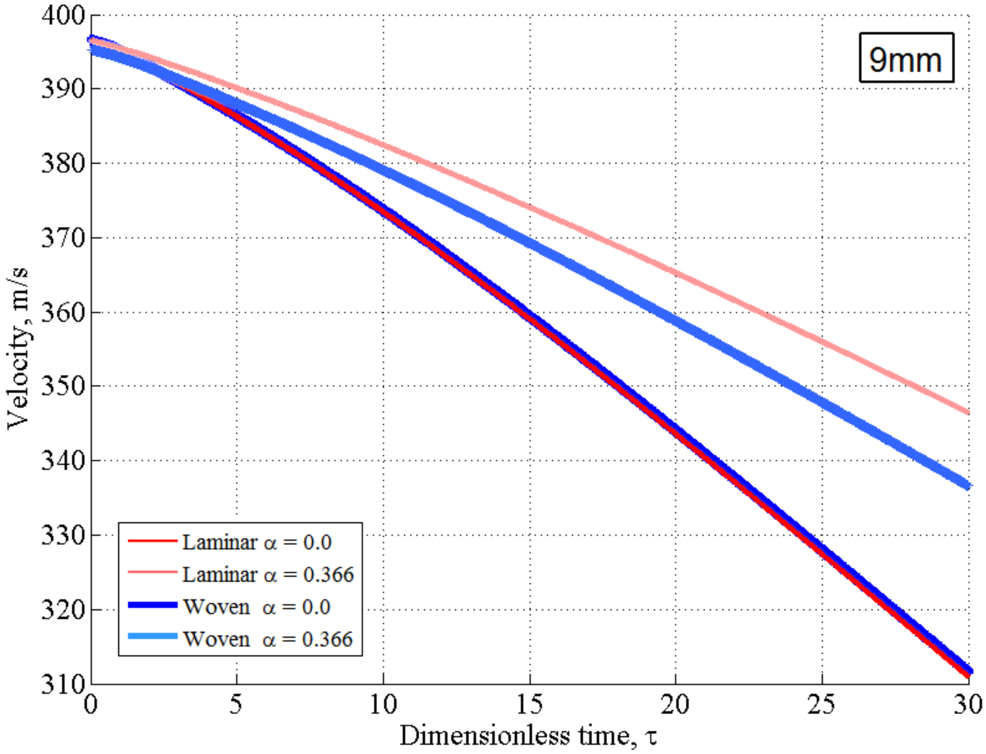

Figure 4.14. Comparison of velocity decay for a 9mm showing two cases of crimp using the laminar model and the same two cases of crimp using the woven model.

Both figures show a trough near the center where $N = 38$ and $\theta = 0°$, where the horizontal axis lies. Also both show the lowest strains along the two sides, where $N = 0$ and 76, $\theta = -90°$ and 90°, which is where the vertical axis lies. Both have the highest peaks around $N = 19$ and $N = 57$, which is very close to $\theta = \pm 45°$. However, as crimp is increased, although the overall strains for both models decrease, the laminar model retains its original shape, with its peaks and valleys at the same node points. On the other hand, the woven model's middle trough and two sides flatten out, and approach the same strains as its other nodes. This indicates that the woven model allows for greater flexibility in movement along the yarn axes when more crimp is introduced, hence evening out the strain around the entire projectile. By contrast, the laminar model does not allow for such a process to occur. Fig. 4.15 also illustrates this point by comparing axis strains for two projectile types, two fabric models, and five crimp cases. As the crimp increases, the axis strains decrease in the two models, but the models exchange places in terms of which model provides the highest axial strain.

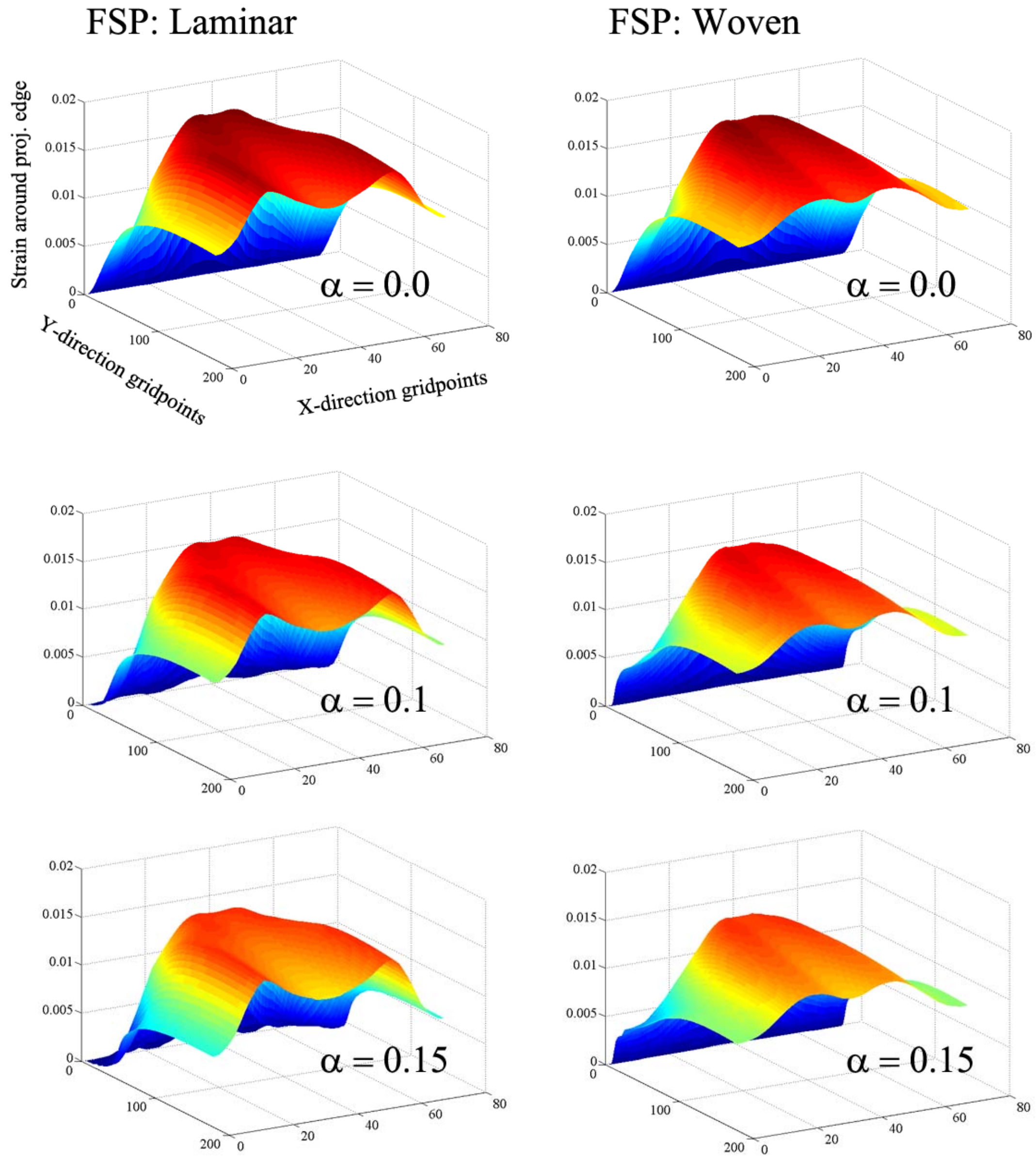
FSP: Laminar

FSP: Woven

Figure 4.15. 3-D surface plots comparing strain profiles around projectile edge post-impact by an FSP using the two models (laminar vs. woven) for five cases of crimp (continued on next page).

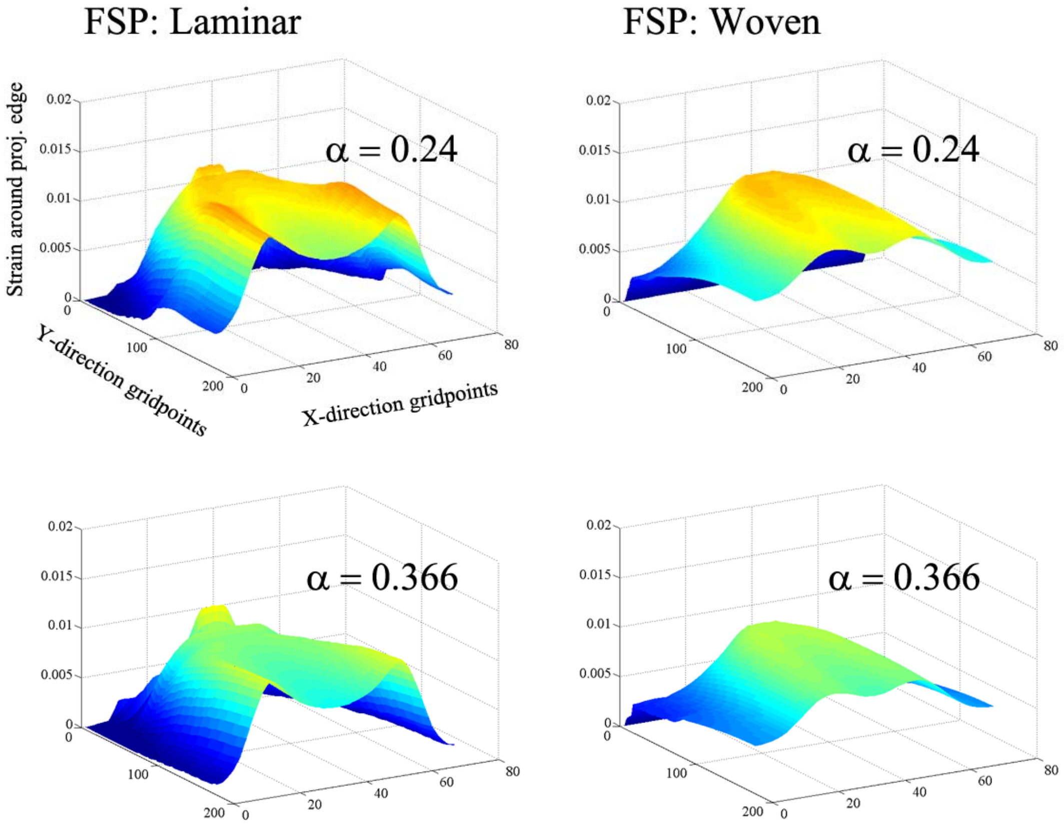

Figure 4.15 (cont).

Following the trends established by velocity decay profiles and strain surface profiles along the projectile edge over time, tension wave profiles for the no crimp case looks nearly identical for the laminar and woven models in Fig. 4.16, as one might expect. The distances traveled, magnitude of strains, and shapes of the waves themselves are nearly identical. However, once crimp is introduced, even in the case of $\alpha = 0.1$, the differences begin to appear between the two models. First, we see the effect of the woven model's tension wave on the strains in crossing yarns as it propagates, forming a visible region of light blue color, which indicates the presence of strain. The laminar model's tension wave seems to have no effect on crossing yarns, and generates no such milder tension waves in the transverse direction. Also, the woven model's tension wave travels farther than the laminar model's tension wave, and this distance gap increases as crimp increases, again due to the stiffening effect of crimp interchange. At the nose or front of the tension wave, the woven model shows greater dispersion than the laminar model.

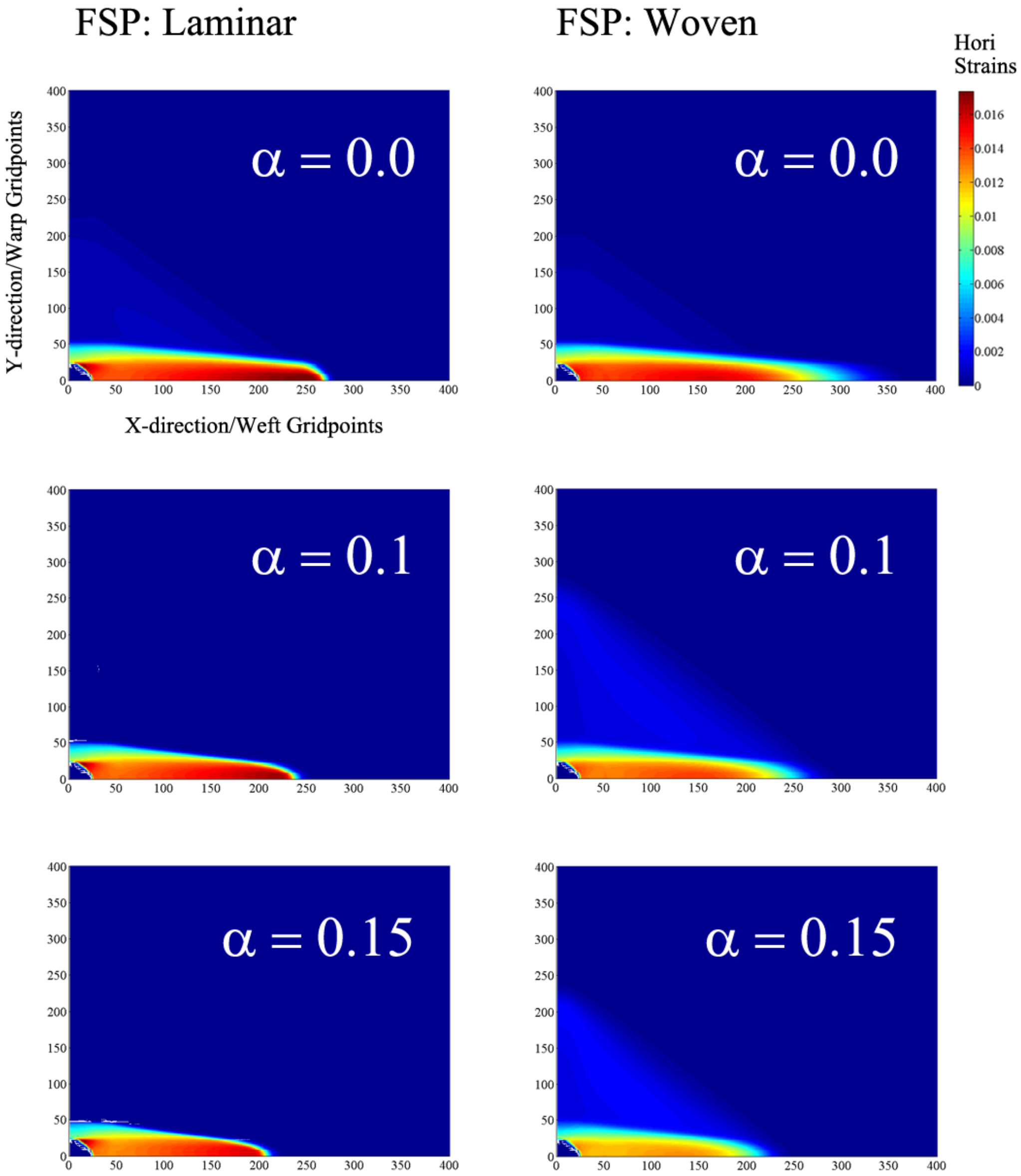

Figure 4.16. Comparison of tension waves post-impact by FSP for the two models (laminar vs. woven) and five cases of crimp at $\tau = 10$ (continued on next page).

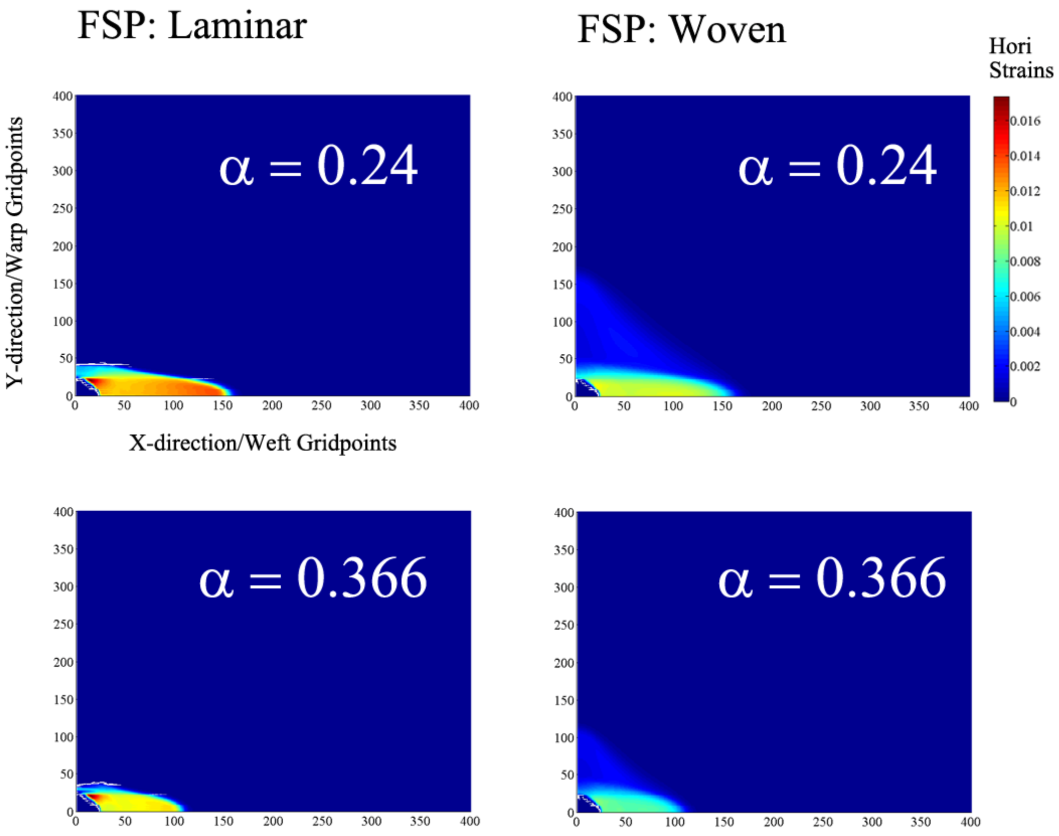

Figure 4.16 (cont).

For the corresponding cone wave profiles in Fig. 4.17, similar observations can be made. Initially with no crimp, both cone waves have the same rounded pyramid shape and travel the same distance. Nevertheless, it is clear from the difference in colors that the laminar model's cone is steeper and with a sharper transition (or corner) at the cone base. As crimp increases, the difference between the distances traveled by the cone wave for the two models increases as well. For the most extreme crimp case, we note three interesting details: (i) the development of out-of-plane force concentrations along the cone edge for the laminar model (causing sudden redirection of the particle velocity from in-plane to out of plane motion – approximately at the velocity of the projectile), (ii) the rounded shape of the cone for the woven model despite its having traveled farther, and (iii) the presence of small forces disturbances that form two “arms” extending out from the cone edge in the laminar model.

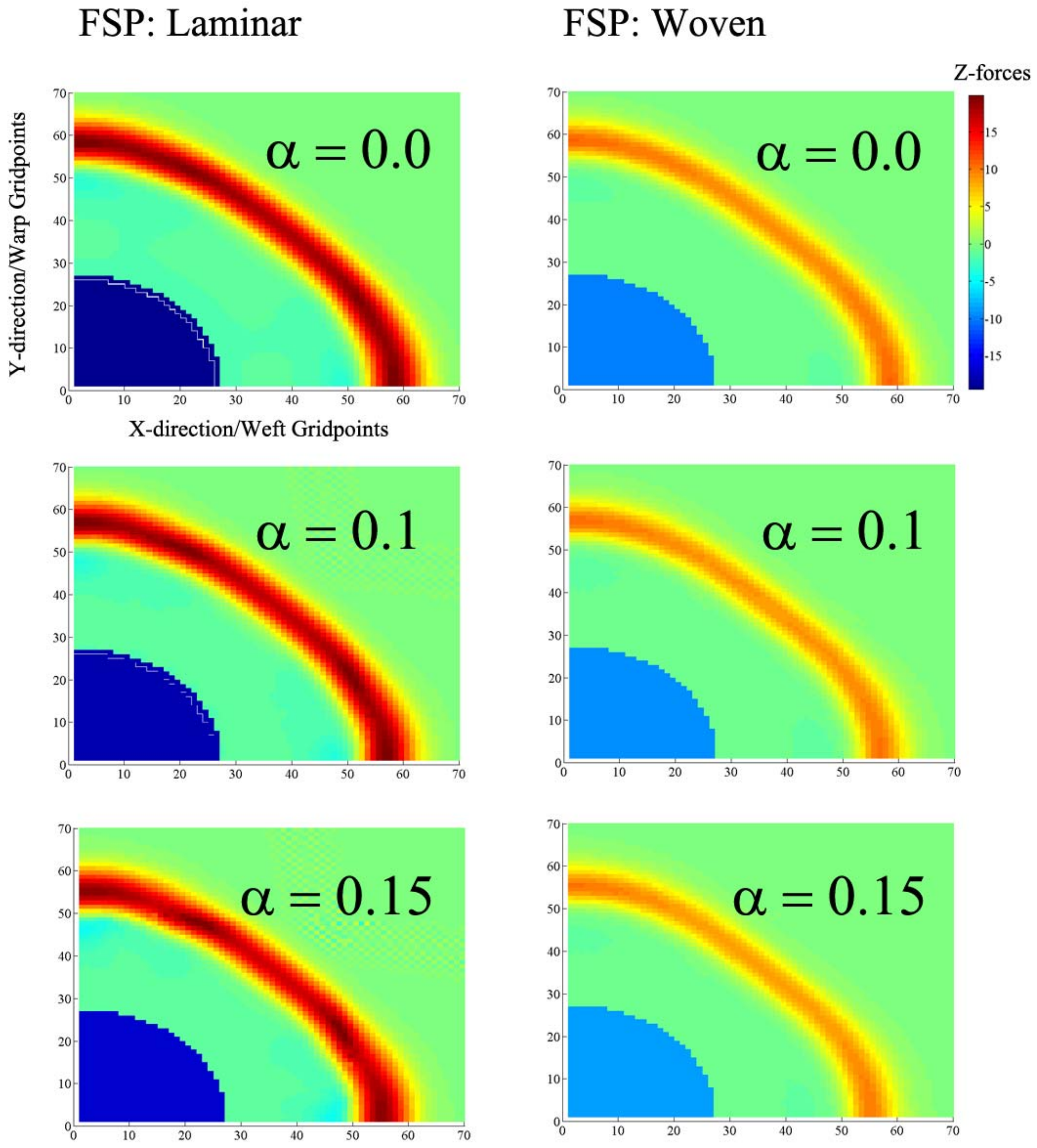

Figure 4.17. Comparison of cone waves post-impact by FSP for the two models (laminar vs. woven) and five cases of crimp at $\tau = 10$ (continued on next page).

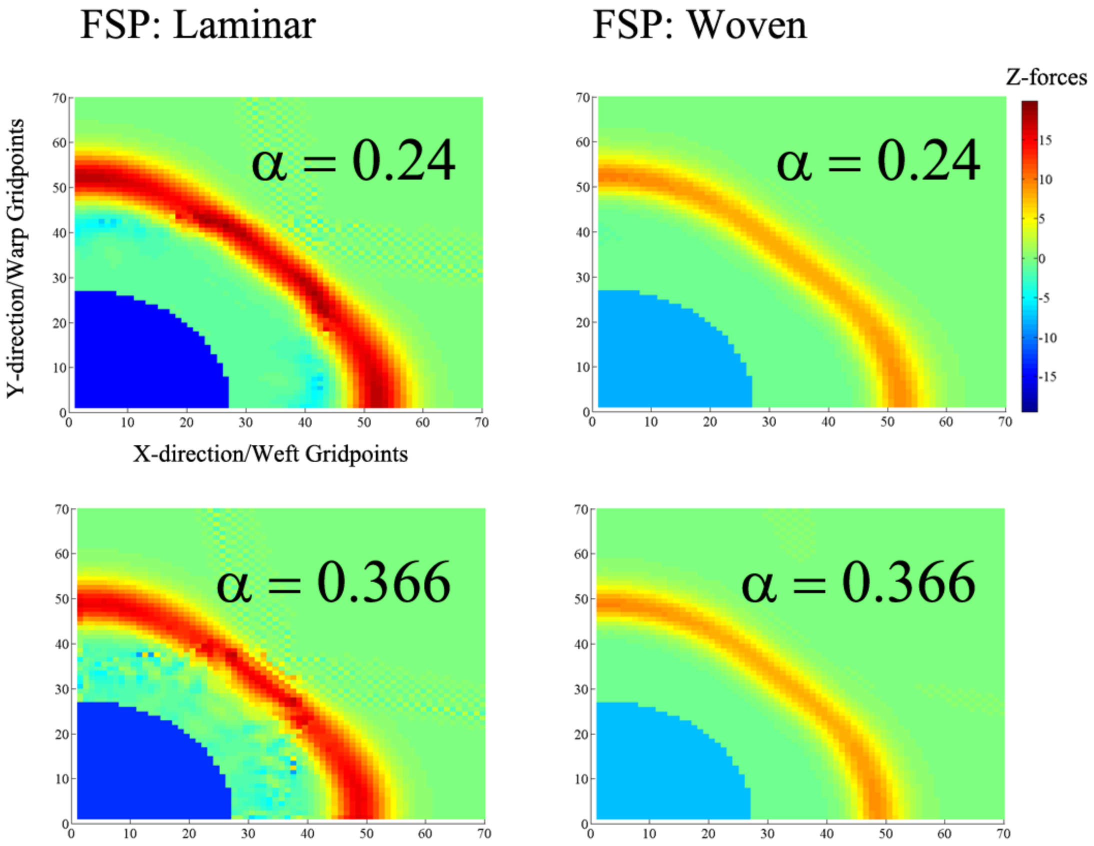

Figure 4.17 (cont).

We now examine Fig. 4.19 to see the crucial differences in the de-crimping process between the two models. In the laminar crimp model, a horizontal tension wave causes de-crimping along both the horizontal/weft axis and along the vertical/warp axis. In the woven crimp model, a horizontal tension wave only causes de-crimping along the horizontal/weft axis, and furthermore, it actually causes greater crimping along the vertical/warp axis. This is known as “crimp-interchange” (also shown in Fig. 4.18), which has been discussed in previous sections and chapters. Even along the horizontal axis, the degree to which crimp is pulled out in the de-crimping process is significantly different between the two models. The laminar model essentially pulls out all the crimp in both directions, to the point where the horizontal slope of the yarns is zero. It also manages to do so in the maximum range out to 45 grid-points. On the other hand, the woven model does not pull out crimp completely, and from the example shown in Fig. 4.19, we see that the horizontal slope still has a magnitude of 0.025 even after the tension wave has passed through those yarns. Even then, it still takes approximately 125 grid-points to complete its de-crimping process. Finally, we note that material length is preserved in the woven model. Along the horizontal *x*-axis, de-crimping causes horizontal slope to decrease from the original 0.15 to 0.025 and while this is a large change, some crimp remains (though very little additional length will be gained from the remaining crimp). Along the *y*-axis, crimp interchange causes the horizontal slope to increase from the original 0.15 to 0.26, almost exactly the same amount that was decreased along the other axis.

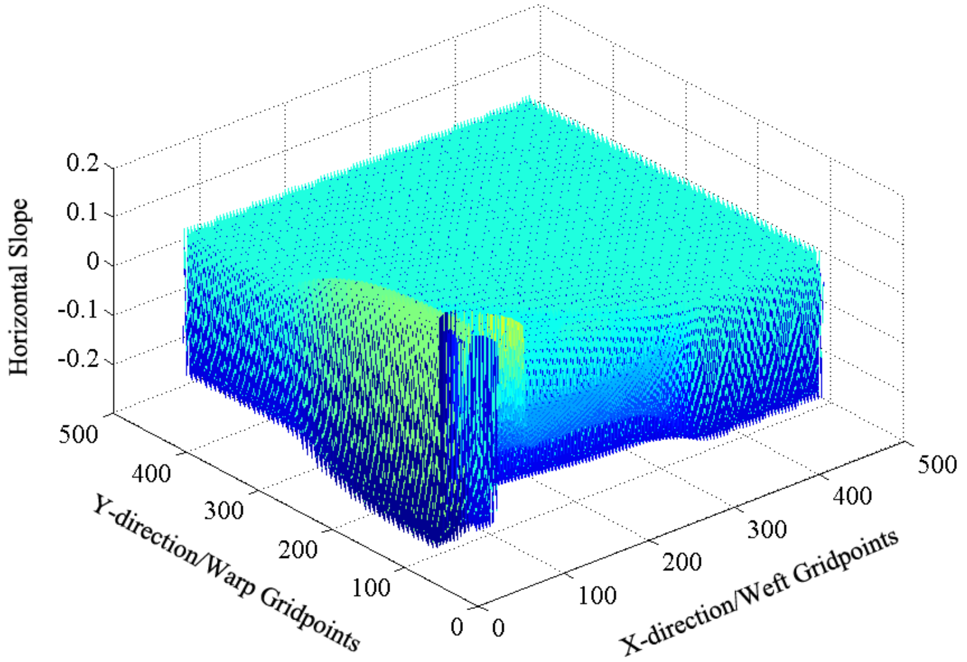

Figure 4.18. 3-D plot of hori yarn de-crimping process in the woven model with crimp interchange. Results are for Case 2b – $\alpha = 0.15$ from Table 4.3

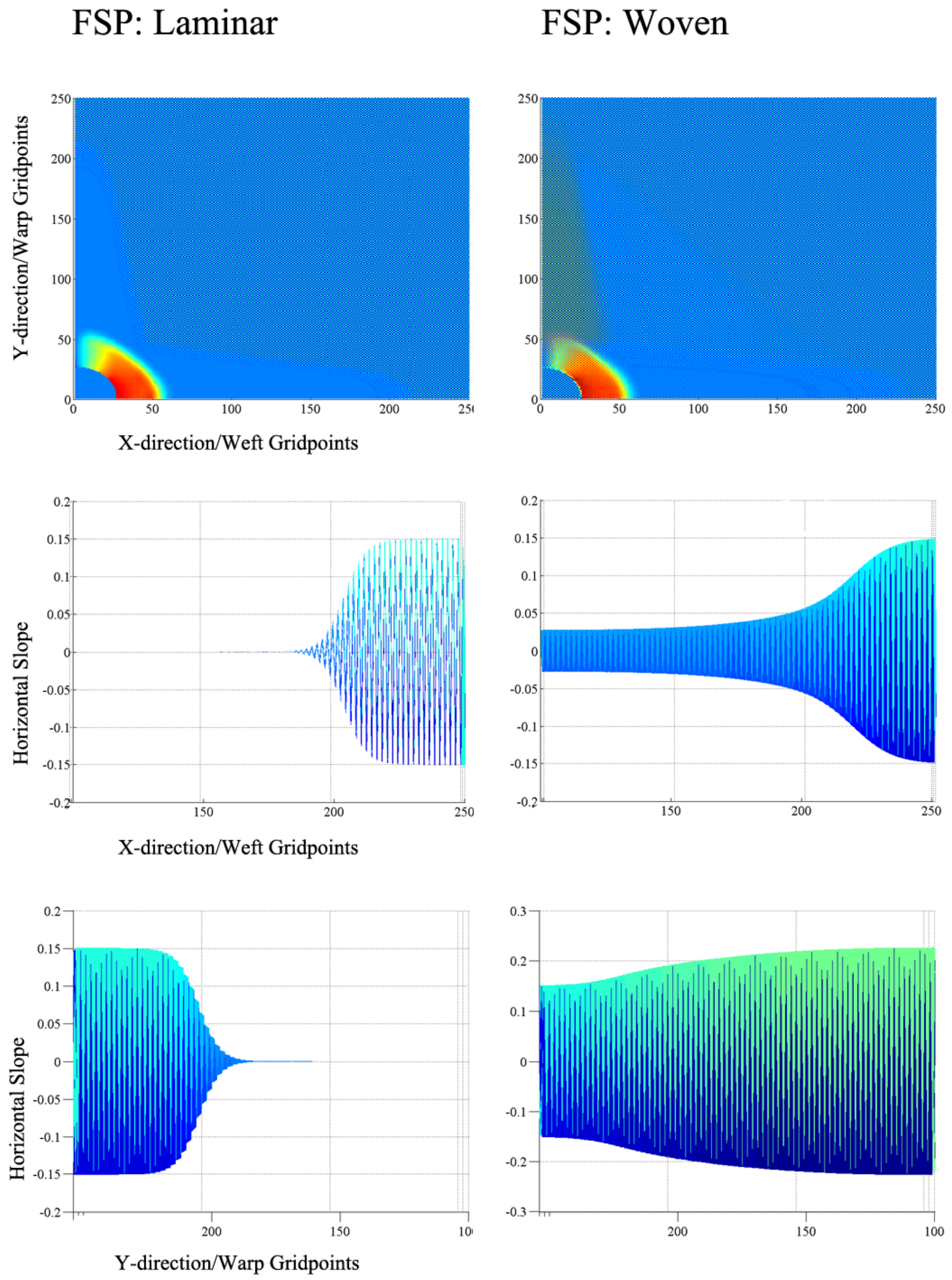

FSP: Laminar

FSP: Woven

Figure 4.19. Fabric and yarn de-crimping process comparison between laminar and woven models.

4.4.4 Effects of varying out-of-plane 'interference' contact spring stiffness

Fig 4.20 shows the effects of varying the out-of-plane contact spring stiffness: $k_{z,\text{inter}}$. This parameter controls how strongly the centers of the top and bottom yarns are forced towards each other, which of course requires yarn flattening or void removal. When this stiffness is high, the connection is strong and the two yarns are more likely to stay locked into position and move as one entity in and out of plane. When low, the stiffness is weak and the two yarns (i.e., the masses are likely to move towards each other.

From the figure, we see that similar to the crimp effect, lowering $k_{z,\text{inter}}$ also lowers the average strain, but increases the final velocity and therefore displacement and BFS. However, all the cases shown had strains that were very close to each other, and practically identical at $T = 10$ (for the FSP) and $T = 30$ (for the 9mm). This brings up the question of whether more differences could be seen on the plot if we used a wider range of $k_{z,\text{inter}}$ values than the 10-125 here. Past studies where $k_{z,\text{inter}}$ values ranged from 0.1-1000 did show somewhat more difference. However, we noticed that in order to accommodate the no crimp case (let α get as close to 0 as possible) and prevent it from going unstable during the simulation, we could not vary the $k_{z,\text{inter}}$ as much as we did in past studies. If we neglect that case or use a slightly higher α such as 0.02 to represent the no crimp case, we could vary $k_{z,\text{inter}}$ much more than the range presented here. Nevertheless, actual yarns used in ballistic fabrics are likely to be sufficiently incompressible and void free for such cases not to be realistic in the first place.

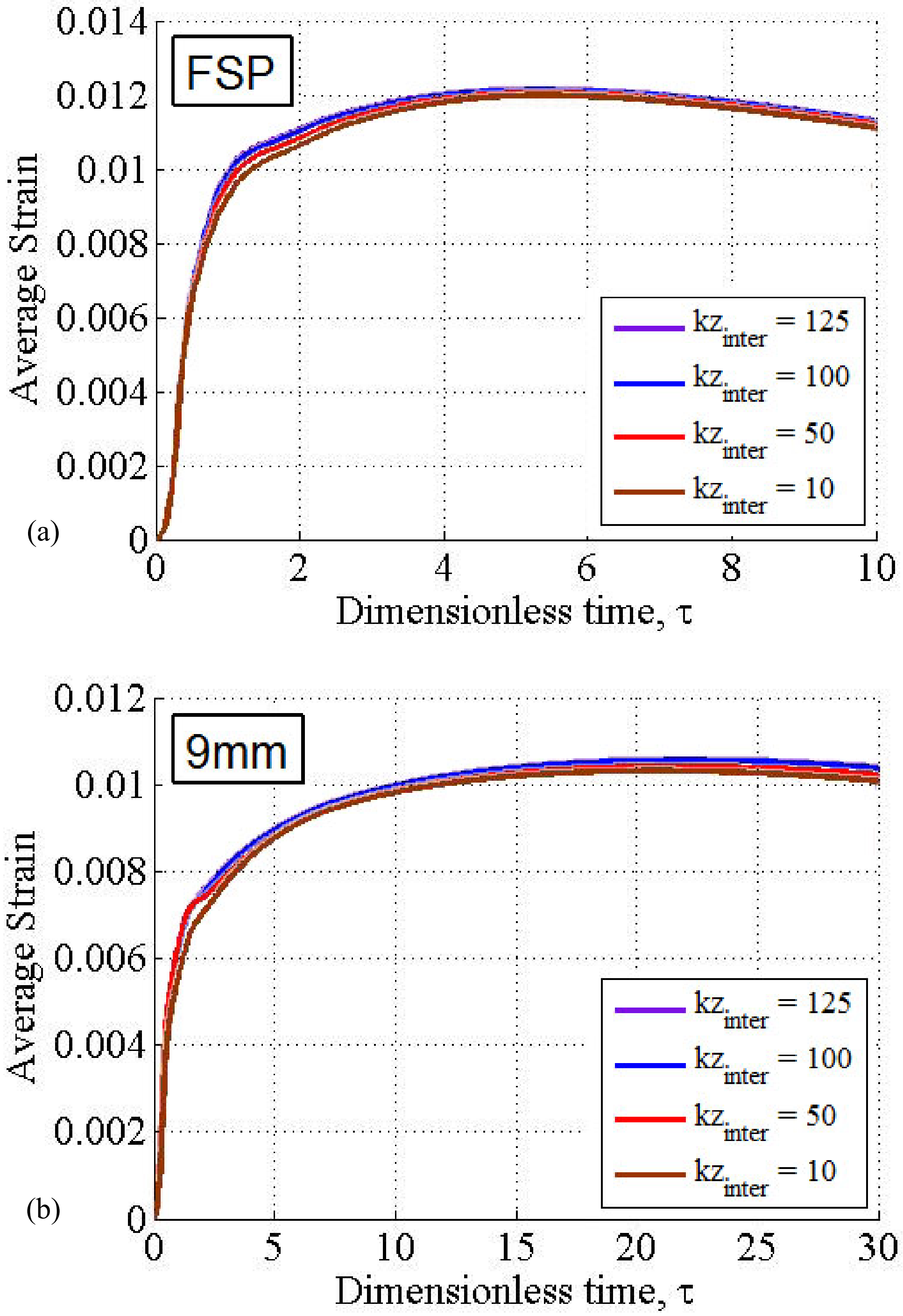

Figure 4.20. Graph comparing average strain around (a) FSP and (b) 9mm edge for four cases of $k_{z,\text{inter}}$ at $\alpha = 0.15$ and time up to $\tau = 10$. Results are for Cases 2b, 1c, 1e, and 2a from Table 4.3.

4.4.5 Effects of varying inter-yarn sliding slip viscosity

Fig. 4.21 shows the effects of varying the inter-yarn slip viscosities: $\mu_{x,\mathrm{inter}}$ and $\mu_{y,\mathrm{inter}}$, which have been set to be equal to each other for all our simulations, and therefore abbreviated as simply μ_{inter} on some plots. This parameter controls how much viscous slip occurs between yarns due to yarn force imbalance at the nodes driving shear effects at the yarn crossovers. In practice, slip also tends to be inversely proportional to the amount of friction existing between yarns as amplified by crimp. Looking at Fig. 4.21, we see that for both the FSP and 9mm cases, the differences in average strain around the projectile between the various μ_{inter} continues to exist over time, rather than just at the initial phases. As noted before, where there is benefit of slip to reducing average strain, there is disadvantage in velocity decay and BFS.

Fig. 4.22 compares the two extreme μ_{inter} cases from Fig. 4.21 in terms of amount of sliding in-plane. We see that when the value of μ_{inter} is relatively large, the friction prevents most of the sliding from occurring. However, the opposite happens when μ_{inter} is relatively small.

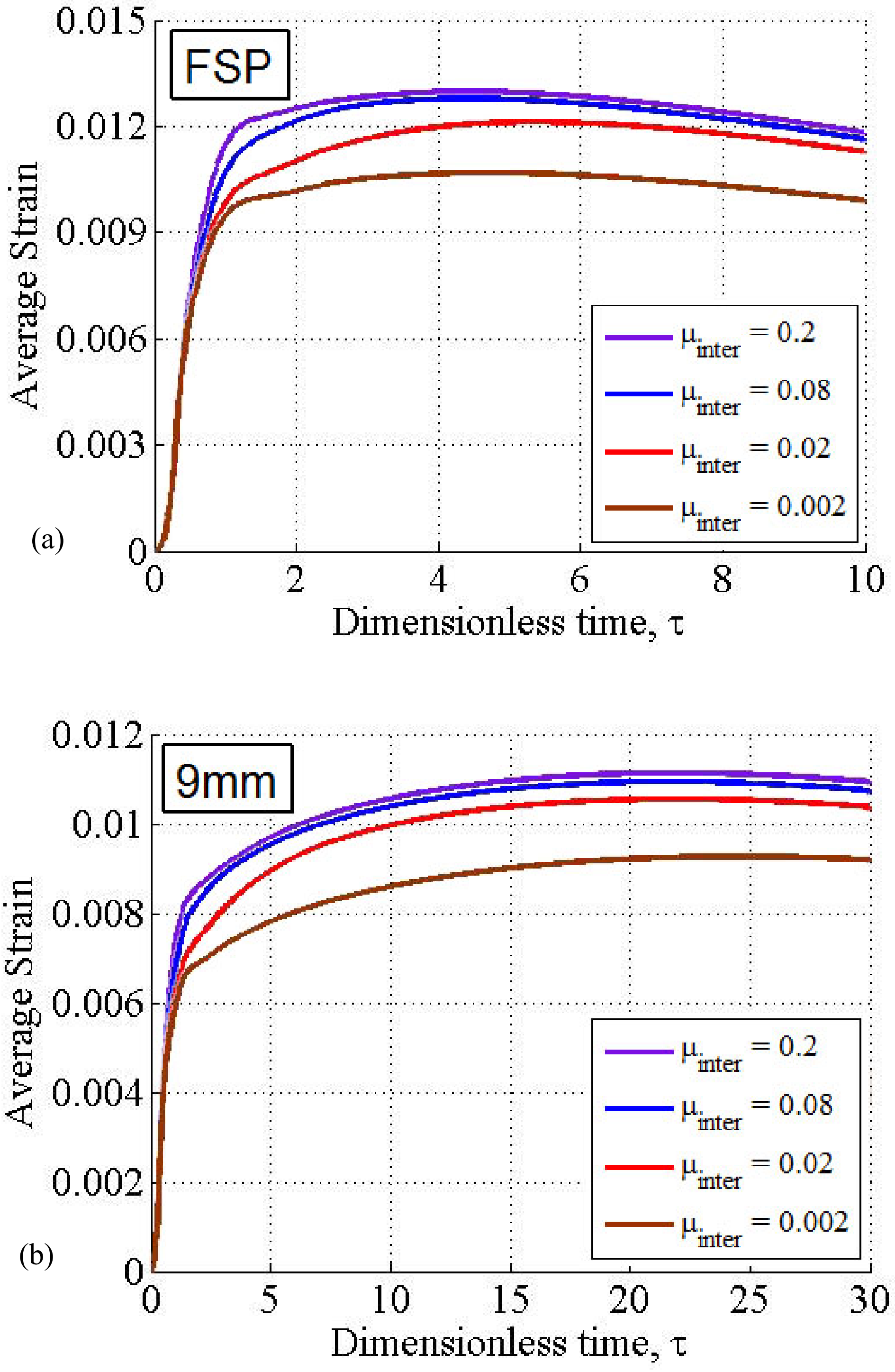

Figure 4.21. Graph comparing average strain around (a) FSP and (b) 9mm edge for four cases of μ_{inter} at $\alpha = 0.15$ and time up to $\tau = 10$. Results are for Cases 3a, 3c, 1c, and 3b from Table 4.3.

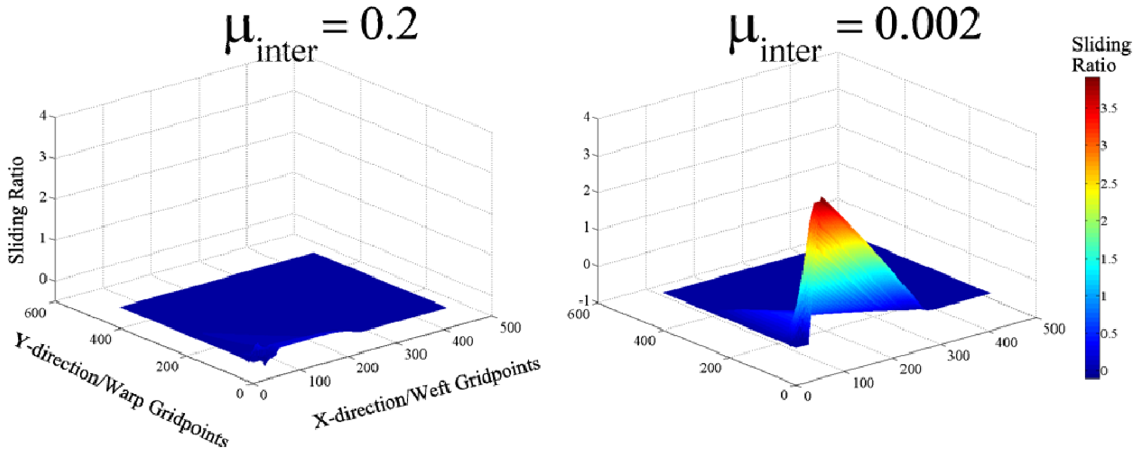

Figure 4.22. 3-D view of the in-plane sliding for two extreme 9mm μ_{inter} values. Results include Cases3a and 3b – FSP- $\alpha = 0.15$.

4.4.6 Effects of varying inter-yarn in-plane shear spring (coupling) stiffness

Fig 4.23 shows the effects of varying the inter-yarn shear spring stiffness, $k_{x,\text{inter}}$ and $k_{y,\text{inter}}$, which have been set to be equal in our simulations. This parameter controls how much elastic restoring force there is between the yarns when they try to slip over one another. Three of the four curves (blue, red, brown) in the figure follow the same patterns with very similar values, with the 3rd case (brown) needing more η to dampen initial oscillations. However, the 4th case (green) is very different from the other three.

We note that in order for the $k_{x,\text{inter}}$ values to have a significant impact on the strain, two conditions need to be met: very low μ_{inter} values and low $k_{x,\text{inter}}$ values. The extremely low (and almost nonexistent) μ_{inter} is analogous to a spring-mass system with no damper, where the yarns are free to slide. The low $k_{x,\text{inter}}$ ensures that yarns at crossover points are not bound tightly together (say with a flexible matrix), and are therefore likely to slip permanently. However, since the $k_{x,\text{inter}}$ value is still influential, it will pull the yarns back a certain amount each time the tension wave tries to move it forward. Although the yarns may slip and slide easily during early times post-impact, resulting in lower strains, a certain amount of material is always needed to build the cone and slow down or stop the projectile, prompting the eventual and hurried "catching up" effect later on, and hence the strain overshoot around $\tau = 7$ in Fig. 4.23 (green line).

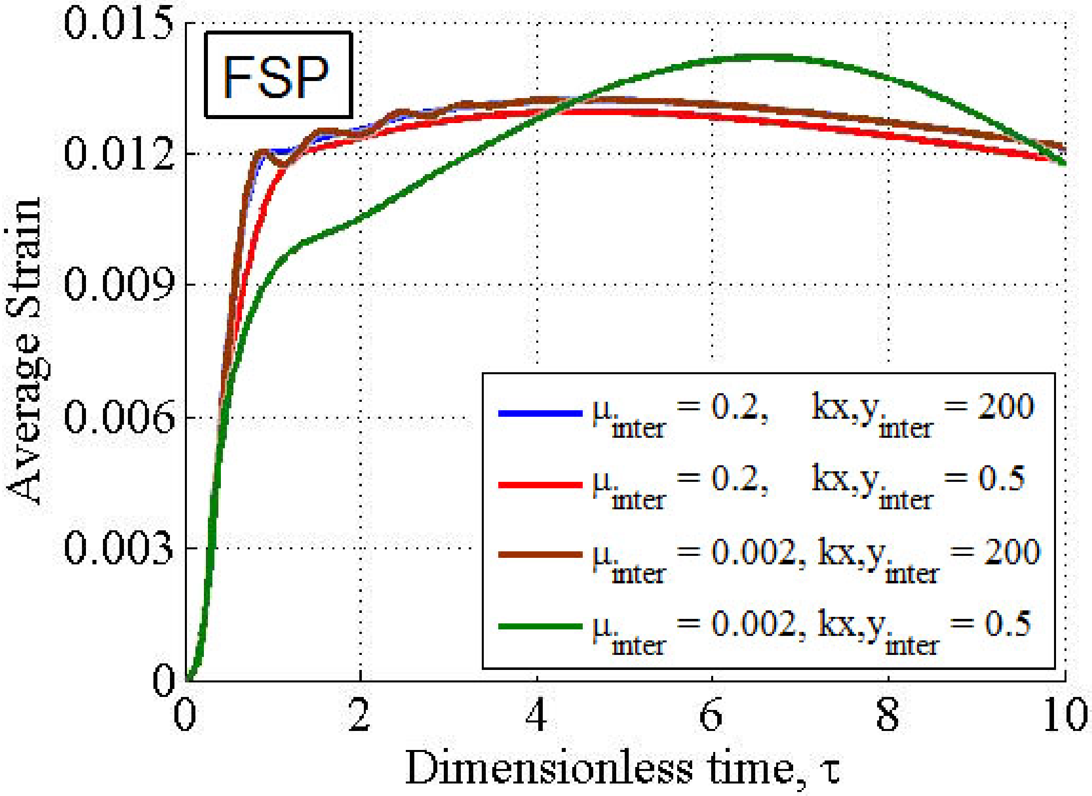

Figure 4.23. Graph comparing average strain around edge of FSP for two cases of $k_{x,\text{inter}}$ and two cases of μ_{inter} at $\alpha = 0.15$ and $\tau = 10$. Results are for Cases 4a, 4b, 4c, and 4d from Table 4.3.

CHAPTER 5

CONCLUSIONS

5.1 Summary of the thesis

In this thesis, we presented two models for numerically simulating the mechanical response of crimped fibrous targets impacted by rigid, high-velocity projectiles with the shape of a right circular cylinder. Projectile-yarn slip was incorporated into our laminar model, and yarn-yarn slip was incorporated into our woven model.

First, our laminar crimp numerical model was developed for projectile impact into a Dyneema® panel modeled as a network of pin-jointed nodal masses with each mass linked to four neighboring masses. A linear viscoelastic relationship described the forces between the nodal masses, as well as the panel's simulation-generated oscillations. Out-of-plane crimp was introduced into the system by assigning alternating over-under initial *z*-positions to the nodes to create a zigzag geometric configuration. The amount of crimp was user-controlled, and could vary from as little as zero crimp (completely flat panel) to as high as necessary. Our model also allowed for user flexibility in setting properties such as Young's modulus, density, projectile mass and velocity, and projectile dimensions. Each individual yarn was assumed to fail when its strain reached a critical value, although we predicted the likelihood of overall fabric failure using the average strain in all the yarns around the region with the highest strain. In our results, we analyzed ballistic performance of the fabric by focusing on performance measures such as strain profiles over time, the rate of velocity deceleration, and the amount of BFS (back-face signature). We also studied the behavior of tension and cone waves over time, and most importantly, the sequence and manner in which the yarns de-crimped. Finally, parametric studies were done on the effects of varying the rocking viscosity coefficient η and the slip viscosity coefficient ζ on the ballistic performance measures stated above. A few general conclusions can be drawn from our simulation results:

(1) In agreement with the Cornell Phoenix Group's previous analytical modeling results, our simulation results show that in a post-impact 2-D target system, the strains first rise to a climax before slowly decreasing, signifying that failure may occur instantaneously or slightly later at the point of maximum strain. Once the strain starts to decrease, the projectile will not have failed enough yarns to penetrate or go through the fabric or panel, although it will continue to travel perpendicular to the fabric for a period of time (while the cone grows) until its velocity eventually reaches zero and it is stopped completely.

(2) Also in agreement with previous analytical findings, our simulation results show that the post-impact strain behavior between projectiles of different sizes such as the FSP and 9mm is very different. We observe that in the FSP, strain builds up to its peak location almost immediately following impact, while this process takes much longer for the 9mm. Hence we conclude that if the target fabric can prevent failure from occurring right away at the moment of impact for lighter projectiles, it will eventually stop the projectile. However, for heavier projectiles, failure can occur later, even after the cone has grown by a significant amount. Experimental studies have also determined that for the

same fabric and using the same critical strain as failure criteria, the FSP has a much higher critical velocity than the 9mm.

(3) Increasing crimp in a fabric system causes a significant decrease in strains (by up to 45% from our test cases). While this is immensely beneficial, we also note that its disadvantage is in the corresponding increase in BFS due to the slower rate of projectile velocity decay and hence allowing for the projectile to travel farther. We compared both FSP and 9mm cases to NIJ's standards for BFS and conclude that under our simulation conditions, only the most extreme crimp cases would not pass the limiting 44mm requirement.

(4) Increasing crimp lowers the velocity of the tension waves by up to 55%, since the waves now need to straighten out the crimp before moving forward. Because the tension wave brings material into the impact region, thus forming the pyramid-shaped cone, the cone also grows more slowly with more crimp although the retardation is not nearly prominent as seen with the tension wave.

(5) Increasing the rocking viscosity coefficient η also lowers the strains, but only on the order of approximately 1% (corresponding to a ten-fold increase in η) for the no crimp case. This difference increases to 5% for the case of highest crimp factor $\alpha = 0.366$, since the overall strains are lower for higher crimp. While increasing η has the benefits of lowering strains and removing system oscillations (especially in the *z*-direction), its disadvantage in more BFS is also similar to that of increasing crimp, but once again, is not nearly as significant.

(6) Due to the way each nodal mass in our fabric model is connected to its four neighbors, the de-crimping of any yarn along an in-plane axis causes an equal amount of de-crimping in a yarn along the other in-plane axis.

(7) The slip viscosity coefficient ζ is relevant to our simulation only when sliding is allowed to occur between the projectile and the yarns in contact with it underneath. Since ζ is proportional to normal contact force and inversely proportional to slip, we vary its value to see the effects of the tension wave collision, which is most significant at lower ζ. For those cases, we observe an initial delay in strain-buildup, followed by a sudden jump in strain caused by the wave collision, with peak strains reaching 1.2 times that of the cases with high friction or no sliding. We define the K_{SC} as the ratio of the peak strain value attained as a result of the wave collision over its steady-state value at long times, and quantitatively compare this against analytical predictions to obtain an excellent agreement with less than 3% error.

Our second numerical model, the woven crimp model, used similar Finite-Difference numerical techniques, fabric and projectile properties, and zigzag crimp configuration as the laminar crimp model. However, this model allowed the yarns to be interlaced in an over-under geometry, with each nodal mass connected to only two of its neighbors, which lie on the same yarn. We further defined the force relations governing the motion between the nodal masses (in all three Cartesian directions) by incorporating six new parameters. Contrary to the previous model where all compressive motion was restricted, this model permitted two nodal masses both at crossover points but belonging to different yarns to compress, or move closer towards each other, although with the limiting condition that they would never "go through" each other and switch places.

From the woven crimp model, the following conclusions were drawn:

(1) In describing the general strain behavior over time of the fabric and the difference between the FSP and 9mm impact cases, (1) and (2) of the laminar crimp model's results also hold for this model.

(2) For the effect of varying crimp on strain behavior, projectile velocity decay, and amount of BFS, the woven crimp model exhibits the same general patterns as the laminar crimp model. However, at the same point in time, the average strains in the woven crimp model are often lower than in the laminar crimp model, differing by as much as 10%. We also compare the rate of projectile velocity decay between the two models, where there is little noticeable difference in the case of no crimp, but in the laminar case the projectile decelerates about 3% slower than in the woven case. Hence we conclude that increasing the amount of crimp exacerbates the differences between the two models, with the differences becoming more pronounced over longer periods of time.

(3) The differences mentioned above in (2) are attributed to the completely opposite natures of the de-crimping process between the two models. In the woven model, we observe the well-documented phenomenon present in fabrics and textiles known as "crimp interchange," where pulling out the crimp in a yarn along an in-plane axis causes more crimp to accumulate in

a yarn along the other in-plane axis. Additionally, the rate of de-crimping is vastly different between the two models, where yarns in the laminar model de-crimp almost three times faster than yarns in the woven model. Furthermore, yarns in the laminar model de-crimp "completely," to the point of zero slopes between two neighboring masses; however, yarns in the woven model only de-crimp to around 15% of their original slopes, most likely due to the stiffening effect between top and bottom nodal masses at crossovers, which prevents "complete" de-crimping.

(4) The crimp interchange effect can also be observed in the tension wave profiles, where there are visibly higher strains in the region of crossing yarns for the woven crimp model, even though its overall strains are lower than the laminar crimp model.

(5) We observe the following general trends for varying the new parameters introduced into the woven crimp model: the effects of increasing or decreasing $k_{z,\text{inter}}$ and μ_{inter} values are correspondingly proportional to average strain values in the target fabric, although there are several key differences. First, the differences in strain observed for the various $k_{z,\text{inter}}$ values are evident at earlier times, but become nearly non-existent later on. In contrast, the differences in strain observed for the various μ_{inter} are much greater in magnitude, and continue to exist in later times. We believe that while the general trends are realistic, the details regarding differences in strain over time would require a more thorough study at much longer times,

as well as a greater range of values for $k_{z,\mathrm{inter}}$, which is not possible with the current code.

(6) The effects of shear spring stiffness $k_{x,\mathrm{inter}}$ and $k_{y,\mathrm{inter}}$ are noticeable only in cases where both of those values, along with $\mu_{x,\mathrm{inter}}$ and $\mu_{y,\mathrm{inter}}$, are relatively small. This is because whether $k_{x,\mathrm{inter}}$ is large, causing yarns at crossovers to be bound tightly together, or $\mu_{x,\mathrm{inter}}$ is large, representing large frictional forces in-plane, the yarns would have some restrictions on its sliding motion. However, when both are small, the yarns are free to slide with no inhibitors, and the result is too much sliding initially, causing low strains, which seem ideal until the system pushes itself to bring much more material necessary to slow down the projectile into the impact zone. By then, there is too much catch up work to do, and strains shoot up far past their steady-state values and then dip down low again, creating an oscillating effect that continues for long periods of time without stabilizing.

5.2 Suggestions on future work

Although we don't anticipate large changes to the general qualitative trends discussed in this thesis, we seek to make future progress in the following areas:

(1) Incorporate crimp effects into our bi-axial analytical model by methods such as quantitatively relating its effects to that of varying the elastic modulus of the yarns (using the numerical model).

(2) Reduce noise/ringing caused by the projectile edge nodes (due to the square mesh) when crimp is extremely low and approaching zero.

(3) Model the projectile nose as the realistic smooth rounded shape, rather than the flat shape used currently.

(4) Include realistic yarn counts in ballistic fabrics into our mesh for discretization.

(5) Extend the woven crimp model to account for multiple layers.

Lastly, we realize that one aspect that will potentially degrade performance is the possibility of the projectile sliding through between yarns due to yarn slip at crossovers. One possible counter measure stems from the fact that ballistic panels usually have many fabric layers, so that the first few layers impacted by the projectile should be designed not to allow slip, or if limited slip is allowed, they should have fine low-denier yarns so that the projectile hits many yarns at once and is less likely to separate them and pass through. Close to the panel's ballistic limit, these early layers are much more likely to be penetrated by the projectile, but in doing so, they typically blunt the projectile as well as form a plug of fabric that effectively broadens the projectile nose as experienced by later layers, which are the ones that halt the projectile. The later layers can then be designed to allow slip and take advantage of the strain reducing benefits. Finally as we have learned previously, a single layer model, with areal density ratio mimicking multiple layers, provides a surprising amount of insight into a tightly spaced multiple layer panel, so the results are immediately useful. Nevertheless, since much previous work from the Cornell Phoenix Group has been devoted to understanding and characterizing the effects of layer gaps on multi-layer bi-axial fabrics' ballistic impact response, it would be logical as a next step to combine that with the woven geometry and crimped yarns presented in this thesis.

REFERENCES

ASTM International. 2008. Standard test method for yarn crimp and yarn take-up in woven fabrics. ASTM D3883-04.

Atas, C., Liu, D. 2008. Impact response of woven composites with small weaving angles. International Journal of Impact Engineering 35 (2) 80-97.

NATO Standardization Agreement (STANAG) 2920, Edition 2. 2003. Ballistic test method for personal armor materials and combat clothing. North Atlantic Treaty Organization. July 31.

Barauskas, R., Abraitiene, A. 2007. Computational analysis of impact of a bullet against the multilayer fabrics in LS-DYNA. International Journal of Impact Engineering 34 (7) 1286-1305.

Bazhenov, S. 1997. Dissipation of energy by bulletproof aramid fabric, Journal of Materials Science. 341627-4,173.

Bilisik, K., Korkmaz, M. 2010. Multilayered and multidirectionally-stitched aramid woven fabric structures: experimental characterization of ballistic performance by considering the yarn pull-out test. Textile Research Journal 80 (16) 1697-1720.

Billon, H.H. 1998. A model for ballistic impact on soft armour. DSTO-TR-0730. Aeronautical and Maritime Research Laboratory, Melbourne, Australia.

Billon, H.H., Robinson, D.J. 2001. Models for the ballistic impact of fabric armour. International Journal of Impact Engineering 25 411-422.

Boubaker, B.B., Haussy, B., Ganghoffer, J. 2007. Consideration of the yarn-yarn interactions in meso/macro discrete model of fabric. Part II: Woven fabric under uniaxial and biaxial extension. Mechanics Research Communications 34 (4) 371-378.

Briscoe, B.J., Motamedi, F. 1992. The ballistic impact characteristics of aramid fabrics: The influence of interface friction. Wear 158 (1-2) 229-247.

Cavallaro, P., Sadegh, A.M. 2010. Crimp-imbalanced protective (CRIMP) fabrics. NUWC-NPT Technical Report 11, 957.

Cavallaro, P. 2011. Soft Body Armor: An overview of materials, manufacturing, testing, and ballistic impact dynamics. NUWC-NPT Technical Report 12,057.

Cheeseman, B.A., Bogetti, T.A. 2003. Ballistic impact into fabric and compliant composite laminates. Composite Structures 61 (1-2) 161-173.

Cheng, C.K., Chen, Y.L. 2010. Ballistic-proof effects of various woven constructions. Fibres and Textiles in Eastern Europe 18 (6) 63-67.

Ching, T.W., Tan, V.B.C. 2006. Modelling ballistic impact on woven fabric with LS-DYNA. Computational Methods 1879-1884.

Chocron-Benloulo, I.S., Rodriguez, J., Sanchez-Galvez, V. 1997. A simple analytical model to simulate textile fabric ballistic impact behavior. Textile Research Journal 67 520-528.

Chocron, S., Figueroa, E., King, N., Kirchdoerfer, T., Nicholls, A.E., Sagebiel, E., Weiss, C., Freitas, C. 2010. Modeling and validation of full fabric targets under ballistic impact. Composites Science and Technology 70 (13) 2012-2022.

Chou, F.J., Yu, C., Chen, K.N., Yu, L.C., Lai, Y.C., Yeh, J.T. 2011. Ultra-high molecular weight polyethylene (uhmwpe)/inorganic nanocomposite material and high performance fiber manufacturing method thereof. EP 2308922 A1.

Cunniff, P.M. 1992. An analysis of the system effects in woven fabrics under ballistic impact. Textile Research Journal 62 (9) 495-509.

Cunniff, P.M. 1999. Dimensional parameters for optimization of textile-based body armor systems. Proceedings of the 18th International Symposium of Ballistics, San Antonio, TX 1303-1310.

Department of Defense Military Standard. 1997. V50 ballistic test for armor. MIL-STD-662F.

Dong, Z. Sun, C.T. 2009. Testing and modeling of yarn pull-out in plain woven Kevlar fabrics. Composites Part A: Applied Science and Manufacturing 40 (12) 1863-1869.

Duan, Y., Keefe, M., Bogetti, T.A., Cheeseman, B.A. 2005. Modeling the role of friction during ballistic impact of a high-strength plain-weave fabric. Composite Structures 68 (3) 331-337.

Duan, Y., Keefe, M., Bogetti, T.A., Cheeseman, B.A., Powers, B. 2006. A numerical investigation of the influence of friction on energy absorption by a high-strength fabric subjected to ballistic impact. International Journal of Impact Engineering 32 (8) 1299-1312.

Figucia, F., Williams, C., Kirkwood, B., Koza, W. 1982. Mechanisms of improved ballistic fabric performance. AD A117104.

Galin, M.P. 1949. Impact on a flexible plate. Sbornik Statei Instituta Mekhaniki.

Grigoryan, D.M. 1949. Normal impact on a unbounded thin diaphragm. PPM 13 277-284.

Grujicic, M., Bell, W.C., Cheeseman, B.A. 2008. Development and verification of a meso-scale based dynamic material model for plain-woven single-ply ballistic fabric. Journal of Materials Science 43 (18) 6301-6323.

Ha-Minh, C., Boussu, F., Kanit, T., Crepin, D., Imad, A. 2011. Analysis on failure mechanisms of an interlock woven fabric under ballistic impact. Engineering Failure Analysis 18 (8) 2179-2187.

Ha-Minh, C., Imad, A., Boussu, F., Kanit,T. 2013. On analytical modeling to predict of the ballistic impact behavior of textile multi-layer woven fabric. Composite Structures 99 462-476.

Hearle, J.W.S., Grosberg, P., Backer, S. 1969. Structural mechanics of fibers, yarns, and fabrics. John Wiley & Sons, Inc. New York.

Hur, H.K., Park, J.S., Kapania, R.K. 2008. The ballistic impact model of plain woven textile structure using meso-scaled yarns. The 49th AIAA Structural Dynamics and Materials Conference, April 7-April 10. Schaumburg, IL, AIAA-2008-1825.

Ivanov, I., Tabiei, A., 2004. Loosely woven fabric model with viscoelastic crimped fibres for ballistic impact simulations. International Journal for Numerical Methods in Engineering 61 (10) 1565-1583.

Jin, L., Hu, H., Sun, B., Gu, B. 2010. A simplified microstructure model of bi-axial warp-knitted composite for ballistic impact simulation. Composites Part B: Engineering 41 (5) 337-353.

King, M.J., Jearanaisilawong, P., Socrate, S. 2005. A continuum constitutive model for the mechanical behavior of woven fabrics. International Journal of Solids and Structures 42(13) 3867-3896.

Kirkwood, J.E., Kirkwood, K.M., Lee, Y.S., Egres, R.G., Wagner, N.J., Wetzel, E.D. 2004. Yarn pull-out as a mechanism for dissipating ballistic impact energy in Kevlar® KM-2 fabric. Textile Research Journal 74 (11) 939-948.

Li, W. 2011. Models for projectile impact into hybrid multi-layer armor systems with axisymmetric or biaxial layers with gaps. Ph.D. dissertation.

Lim, C.T., Tan, V.B.C., Cheong, C.H. 2002. Perforation of high-strength double-ply fabric system by varying shaped projectiles. International Journal of Impact Engineering 27 (6) 577-591.

Luan, K., Sun, B., Gu, B. 2013. Ballistic impact damages of 3-D angle-interlock woven composites based on high strain rate constitutive equation of fiber tows. International Journal of Impact Engineering 57 145-158.

National Institute of Justice (NIJ) Standards. 2008. Ballistic resistance of personal body armor. 0101.06.

Nilakantan, G., Gillespie, J.W. 2012. Ballistic impact modeling of woven fabrics considering yarn strength, friction, projectile impact location, and fabric boundary condition effects. Composite Structures 94 (12) 3624-3634.

Nilakantan, G., Wetzel, E.D., Bogetti, T.A., Gillespie, J.W. 2013. A deterministic finite element analysis of the effects of projectile characteristics on the impact response of fully clamped flexible woven fabrics. Composite Structures 95 191-201.

Novotny, W.R., Cepus, E., Shahkarami, A., Vaziri, R., Poursartip, A. 2007. Numerical investigation of the ballistic efficiency of multi-ply fabric armours during the early stages of impact. International Journal of Impact Engineering 34(1) 71-88.

Parga-Landa, B., Hernandez-Olivares, F. 1995. An analytical model to predict impact behaviour of soft armours. International Journal of Impact Engineering 16(3) 455-466.

Parsons, E.M., Weerasooriya, T., Sarva, S., Socrate, S. 2010. Impact of woven fabric: Experiments and mesostructure-based continuum-level simulations. Journal of the Mechanics and Physics of Solids 58 (11) 1995-2021.

Parsons, E.M., King, M.J., Socrate, S. 2013. Modeling yarn slip in woven fabric at the continuum level: simulations of ballistic impact. Journal of Mechanics and Physics of Solids 61 (1) 265-292.

Phoenix, S. L., Porwal, P. K.. 2003. A new membrane model for the ballistic impact response and V50 performance of multi-ply fibrous systems. International Journal of Solids and Structures 40 (24) 6723-6765.

Phoenix, S.L., Yavuz, A.K., Porwal, P.K. 2010. A new interference approach for ballistic impact into stacked flexible composite body armor. AIAA Journal 48 (2) 490-501.

Phoenix, S.L., Yavuz, A.K., Zhou, R., Li, W., Van der Werff, H., Heisserer, U. 2010. Design optimization of integrated multi-ply body armor by a computation tool (DO-IMPACT). PASS 2010.

Phoenix, S.L., Heisserer, U., van der Werff, H., van der Jagt-Deutekom. Submitted. Modeling and experiments on ballistic impact into UHMWPE yarns using flat and saddle-nosed projectiles. Journal of Strain Analysis, special issue on High Velocity Impact Behavior of Composites.

Porwal, P. K., Phoenix, S.L. 2005. Modeling system effects in ballistic impact into multi-layered fibrous materials for soft body armor. International Journal of Fracture 135 (1-4) 217-249.

Rakhmatulin, Kh.A., Dem'yanov, Y.A. 1961. Strength under high transient loads. 94-152 (English translation, Israel Program for Scientific Translations, 1966).

Rao, M. P., Duan, Y., Keefe, M., Power, B. M., Bogetti, T.A. 2009. Modeling the effects of yarn material properties and friction on the ballistic impact of a plain-weave fabric. Composite Structures 89 (4) 556-566.

Roylance, D.K., Wilde, A., Tocci, G. 1973. Ballistic impact of textile structures. TEXTILE RI-iseancn Journal 43(1).

Roylance, D. 1980. Stress wave propagation in fibres: Effect of crossovers. Fibre Science and Technology 13 (5) 385-395.

Roylance, D., Wang, S.S. 1980. Penetration mechanics of textile structures ballistic materials and penetration mechanics. Elsevier 273-292.

Roylance, D., Chammas, P., Ting, J., Chi, H., Scott, B. 1995. Numerical modeling of fabric impact. Proceedings of the National Meeting of the American Society of Mechanical Engineers (ASME).

Shahkarami, A., Vaziri, R. 2007. A continuum shell finite element model for impact simulation of woven fabrics. International Journal of Impact Engineering 34 (1) 104-119.

Shim, V.P.W., Tan, V.B.C., Tay, T.E. 1995. Modelling deformation and damage characteristics of woven fabric under small projectile impact. International Journal of Impact Engineering 16 (4) 585-605.

Shim, V.P.W., Guo, Y.B., Tan, V.B.C. 2012. Response of woven and laminated high-strength fabric to oblique impact. International Journal of Impact Engineering 48 87-97.

Shimek, M.E., Fahrenthold, E.P. 2012. Effects of weave type on the ballistic performance of fabrics. AIAA Journal 50 (11) 2558-2565.

Scott, B.R. 1999. The penetration of compliant laminates by compact projectiles. Proceedings of the 18th International Symposium of Ballistics 1181-1191.

Stig, F., Hallstrom, S. 2013. Influence of crimp on 3D-woven fibre reinforced composites. Composite Structures 95 114-122.

Tabiei, A., Ivanov, I. 2002. Computational micro-mechanical model of flexible woven fabric for finite element impact simulation. International Journal for Numerical Methods in Engineering 53 1259-1276.

Tabiei, A., Nilakantan, G. 2008. Ballistic impact of dry woven composites: a review. Applied Mechanics Reviews 61(1) 10801-10813.

Talebi, H., Wong, S.V., Hamouda, A.M.S. 2009. Finite element evaluation of projectile nose angle effects in ballistic perforation of high strength fabric. Composite structures 87 (4) 314-320.

Tan, V.B.C., Shim, V.P.W., Tay, T.E. 2003. Experimental and numerical study of the response of flexible laminates to impact loading. International Journal of Solids and Structures 40 (23) 6245-6266.

Tan, V.B.C., Shim, V.P.W., Zeng, X. 2005. Modelling crimp in woven fabrics subjected to ballistic impact. International Journal of Impact Engineering 32 (1-4) 561-574.

Tan, V.B.C., Ching, T.W. 2006. Computational simulation of fabric armour subjected to ballistic impacts. International Journal of Impact Engineering 32 (11) 1737-1751.

Tan, V.B.C., Zeng, X.S., Shim, V.P.W. 2008. Characterization and constitutive modeling of aramid fibers at high strain rates. International Journal of Impact Engineering 35, 1303-1313.

Ting, C., Ting, J, Cunniff, P.M., Roylance, D. 1998. Numerical characterization of the effects of transverse yarn interaction on textile ballistic response. Proceedings of the international SAMPE Technical Conference.

Van, H.J., Shakarami, S., Cunningham, D.V., Pritchard, L.E. 2008. Densely woven quasi-unidirectional fabric for ballistic applications. EP 1908864 A1.

Vinson, J.R., Zukas, J.A. 1975. On the ballistic impact of textile armor. ASME Journal of Applied Mechanics 42 263-268.

Wang, X., Hu, B., Feng, Y., Liang, F., Mo, J., Xiong, J., Qiu, Y. 2008. Low velocity impact properties of 3D woven basalt/aramid hybrid composites. Composites Science and Technology 68 (2) 444-450.

Wang, Y., Miao, Y., Swenson, D., Cheeseman, B., Yen, C., LaMattina, B. 2010. Digital element approach for simulating impact and penetration of textiles. International Journal of Impact Engineering 37 (5) 552-560.

Walker, J.D. Constitutive model for fabrics with explicit static solution and ballistic limit. 1999. Proceedings of the 18th International Symposium of Ballistics 1231-1239.

Walker, J.D. Ballistic limits of fabrics with resin. 2001. Proceedings of the 19th International Symposium of Ballistics.

Young, S. L., Wetzel E. D., Wagner, N. J. 2003. The ballistic impact characteristics of Kevlar® woven fabrics impregnated with a colloidal shear thickening fluid. Journal of Materials Science 38 (13) 2825-2833.

Zeng, X.S., Shim, V.P.W., Tan, V.B.C. 2005. Influence of boundary conditions on the ballistic performance of high-strength fabric targets. International Journal of Impact Engineering 32 (1-4) 631-642.

Zeng, X.S., Tan, V.B.C., Shim, V.P.W. 2006. Modelling inter-yarn friction in woven fabric armour. International Journal for Numerical Methods in Engineering 66 (8) 1309-1330.